Observation of a Double-Λ Hypernucleus ${}^{}_{\Lambda\Lambda}$Be with Hybrid Emulsion Method at J-PARC

Hiroyuki Ekawa

December, 2019

Observation of a Double-Λ Hypernucleus $^{\ }_{\Lambda\Lambda}$Be with Hybrid Emulsion Method at J-PARC

A dissertation

by

Hiroyuki Ekawa

Submitted to
Department of Physics, Kyoto University
in partial fulfillment of the requirements
for the Degree of Doctor of Science

December, 2019

Abstract

Experimental study of double-Λ hypernuclei is a most effective method to investigate the $\Lambda\Lambda$ interaction. Among several observations, only the NAGARA event gives us an unambiguous information, the $\Lambda\Lambda$ bonding energy ($\Delta B_{\Lambda\Lambda}$) of $0.67 \pm 0.17\,\mathrm{MeV}$ in ${}^{\ 6}_{\Lambda\Lambda}\mathrm{He}$. However, since the $\Lambda\Lambda$ interaction could be affected by the possible change of the core nucleus, systematic study of various species are essential. Furthermore, other related information such as $\Lambda\Lambda$ p-wave interaction, $\Lambda\Lambda$-$\Xi^- p$ mixing are totally unknown.

Therefore, E07 experiment was carried out to collect ten times more statistics than the past experiments. In order to collect such enormous double-Λ hypernuclei events efficiently, we adopted a counter-emulsion hybrid method. A Ξ^- hyperon produced in the (K^-, K^+) reaction off a diamond target was injected into emulsion sheets. It stopped in the emulsion by losing its kinetic energy and was captured in the atomic orbit of a nucleus. Double-Λ hypernuclei were searched by detecting Ξ^- stopping point with an automated microscope tracking system.

The E07 experiment was performed at the K1.8 beam line of the hadron experimental hall in 2016 and 2017. Two magnetic spectrometers of the K1.8 beam line spectrometer and the KURAMA spectrometer were used for the selection of Ξ^- production with (K^-, K^+) reaction at $1.8\,\mathrm{GeV}/c$. In total, 2.1 tons of emulsions were exposed to the K^- beam. The detected Ξ^- hyperons were almost ten times more than that in the KEK E373 experiment.

A double-Λ hypernucleus of ${}_{\Lambda\Lambda}\mathrm{Be}$ was newly observed. Possible interpretations of this event are narrowed down to ${}^{\ 10}_{\Lambda\Lambda}\mathrm{Be}$, ${}^{\ 11}_{\Lambda\Lambda}\mathrm{Be}$, and ${}^{\ 12}_{\Lambda\Lambda}\mathrm{Be}$ by taking account of the NAGARA event. The most probable candidate was obtained to be ${}^{\ 11}_{\Lambda\Lambda}\mathrm{Be}$ from the kinematic analysis. In that interpretation the binding energy of the $\Lambda\Lambda$ system is estimated to be 19.07 ± 0.11 MeV, and the $\Lambda\Lambda$ bonding energy 1.87 ± 0.36 MeV. The present result including other interpretations was discussed with the past measurements and theoretical calculations.

Contents

Chapter 1

Introduction

1.1 Baryon–Baryon interaction

Understanding the baryon-baryon (BB) interactions in terms of quantum chromo dynamics (QCD) is one of the main topics in hadron physics. A baryon is composed of three constituent quarks in non-relativistic quark models. The color charge of the quarks is confined in a baryon to become colorless. Therefore, we do not see any direct effects of quark gluon dynamics of QCD in the BB interactions. On the other hand, the confinement of the quarks in a baryon must be taken into account, where the non-perturbative nature of the QCD dominates.

A typical BB interaction is nuclear force between nucleons (NN). The realistic nuclear force models have been developed in the framework of meson-exchange models based on a lot of NN scattering database. They succeeded to describe various low energy nuclear phenomena. By extending these models in flavor SU(3) introducing s-quark, the nuclear force is extended among baryon octet; namely, nucleons (p, n) and hyperons $(\Lambda, \Sigma^{-,0,+}, \Xi^{-,0})$. The interaction between octet baryons are classified as the following irreducible representations in the $\mathrm{SU}(3)_f$ (Fig. 1.1):

$$8 \otimes 8 = 27_s \oplus \overline{10}_a \oplus 10_a \oplus 8_s \oplus 8_a \oplus 1_s. \tag{1.1}$$

Here, the nuclear force is only included in 27_s and $\overline{10}_a$. Therefore, it is not trivial to extend the information on nuclear force to other categories, such as 8, 1_s.

The experimental information of hyperon(Y)-nucleon interaction is very much limited in statistics and covered energy regions. This is because the hyperon life-times are too short to carry out the YN scattering at low energies. Thus, the effective interaction information of YN has been extracted through the spectroscopic information of hypernuclei, bound systems of Y in nuclei. The production of hyper nuclei was extended from Λ hypernuclei to Σ^-, Ξ^-, double-Λ hyper nuclei, and now the research field is called strangeness nuclear physics. The single particle potential depth of a Λ in nuclear matter is known to be $-29\,\mathrm{MeV}$, while the ΣN interaction is repulsive, $+30\,\mathrm{MeV}$. In particular, the spin-orbit force between ΛN is measured to be very small compared with that of NN.

The Nijmegen group has been working for developing the BB interaction models in the frame work of one-boson-exchange in $\mathrm{SU}(3)_f$. The extended-soft-core model ESC08 is

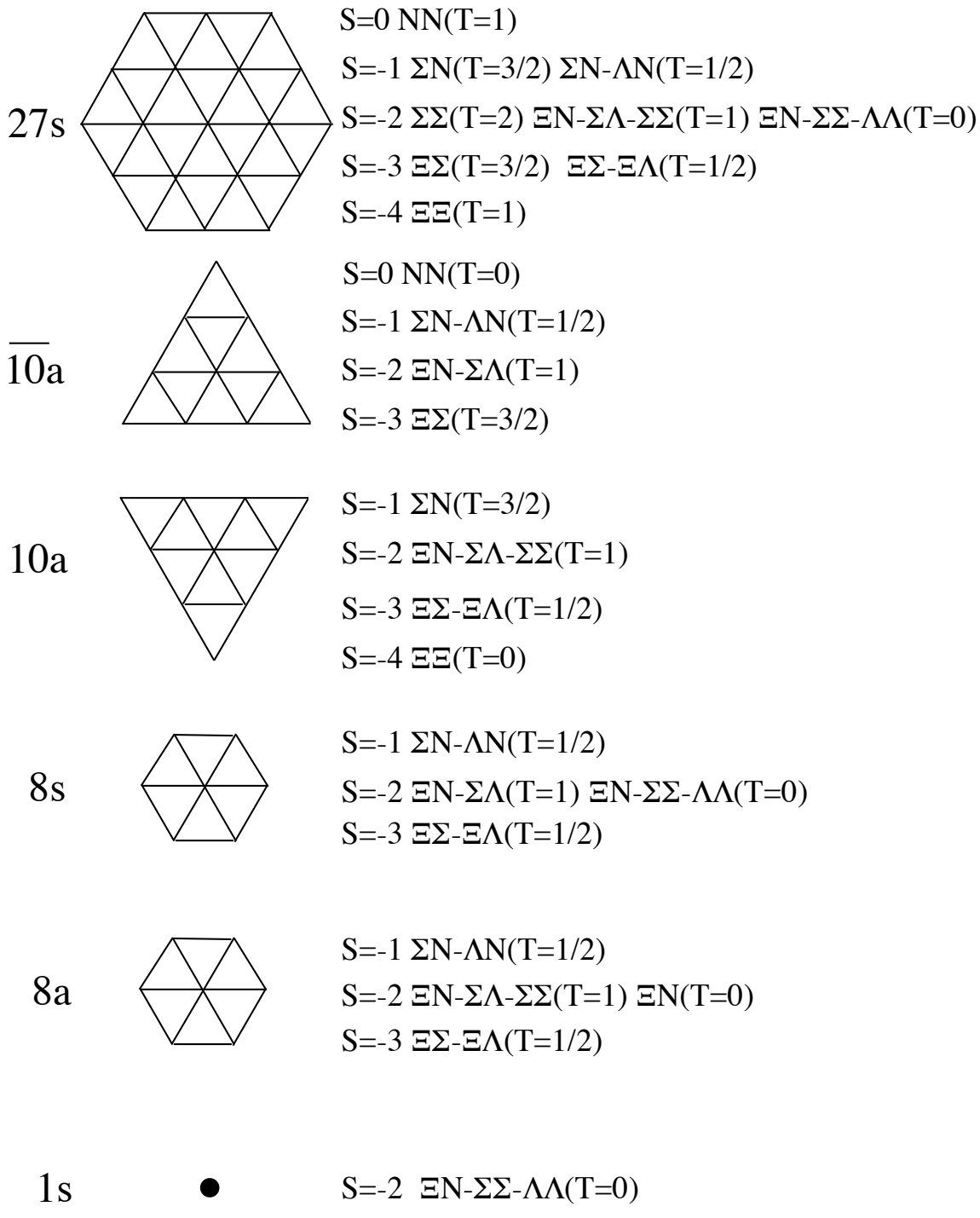

Figure 1.1: Representation of two baryon systems in $SU(3)_f$ symmetry.

their most complete and sophisticated model [1]. It was developed to include multiple-gluon exchange and structural effect due to the quark-core of the baryons. The ESC meson-exchange interaction consists of local- and non-local-potentials due to (i) one-boson-exchange, (ii) pomeron and odderon (multiple-gluon) exchange, (iii) two pseudo-scalar exchange, and (iv) meson-pair-exchange. The ESC model describes the NN, NY and YY interaction in a unified way using broken SU(3) symmetry, which is utilized to make a simultaneous fit to the NN and YN data with a single-set of parameters. The ESC08 model can reproduce single particle potentials. No bound state of $S = -1$ was found. They have constructed ESC16 as an improved version. [2, 3]. This model shows reasonable scattering cross sections comparing to ESC08. However, the Ξ well-depth becomes repulsive, $+13.7\,\mathrm{MeV}$ (unpublished), while the experimental data suggests $-14\,\mathrm{MeV}$ [4].

The HAL collaboration succeeded to obtain the BB potentials with the Lattice QCD method [5]. With the help of rapid improvements in supercomputer technology, they can perform the simulation almost at the pion physical mass as shown in Table 1.1. The K-configuration is adopted as the gauge configuration to perform lattice QCD numerical simulations [6].

Table 1.1: Mass of pseudo-scalar meson and the octet baryons measured in the lattice QCD simulation with the K-configuration set.

Hadron	π	K	N	Λ	Σ	Ξ
Mass [MeV]	146	525	958(3)	1140(2)	1223(2)	1354(1)

Figure 1.2 shows diagonal parts of flavor-basis potentials of baryon-baryon s-wave interactions in $S = -2$ sector. The upper three figures show flavor-symmetric two baryons in the ${}^1S_0$ partial wave and the lower six figures show flavor-anti-symmetric two baryons in the ${}^3S_1 - {}^3D_1$ partial wave, respectively. These results demonstrate a phenomenological feature of hadron interaction in $SU(3)_f$ symmetry. The entire attraction in the flavor singlet sector and the extreme repulsion in the flavor octet sector are characteristic. The potential of the 27-plet and 10^*-plet shows the two nucleon potential in the $\mathrm{SU}(3)_f$ symmetry limit. HAL QCD method can reasonably reproduce the BB interaction from QCD.

It should be noted that they also extracted the single-particle potential of hyperons in nuclear matter based on the Brueckner-Hartree-Fock (BHF) approximation. The potential is obtained by summing elements of the G-matrix in this frame work. In order to simplify the calculation, the flavor-basis diagonal components and the SU(3) Clebsch-Gordan coefficients were used. Figure 1.3 shows the hyperon single-particle potentials $U_Y(k)$ in the pure neutron matter (PNM) and the symmetric nuclear matter (SNM). The density of matter was fixed to the normal nuclear matter density of $\rho_0 = 0.17\mathrm{fm}^{-3}$. $U_\Lambda(0) = -28\,\mathrm{MeV}$, $U_\Sigma(0) = +15\,\mathrm{MeV}$, and $U_\Xi(0) = -4\,\mathrm{MeV}$ as the central value with the statistical error about $\pm 2\,\mathrm{MeV}$ in SNM. Since the matter at center of heavy nuclei is analogous to SNM, experimental values of $U_Y(0)$ obtained from hypernuclei experiments can confirm the calculation. At present, experimental data indicate that $U_\Lambda(0) \simeq -30\,\mathrm{MeV}$, $U_\Sigma(0) \geq +20\,\mathrm{MeV}$, and $U_\Xi(0) \simeq -10\,\mathrm{MeV}$. The calculations show reasonable agreement with these data.

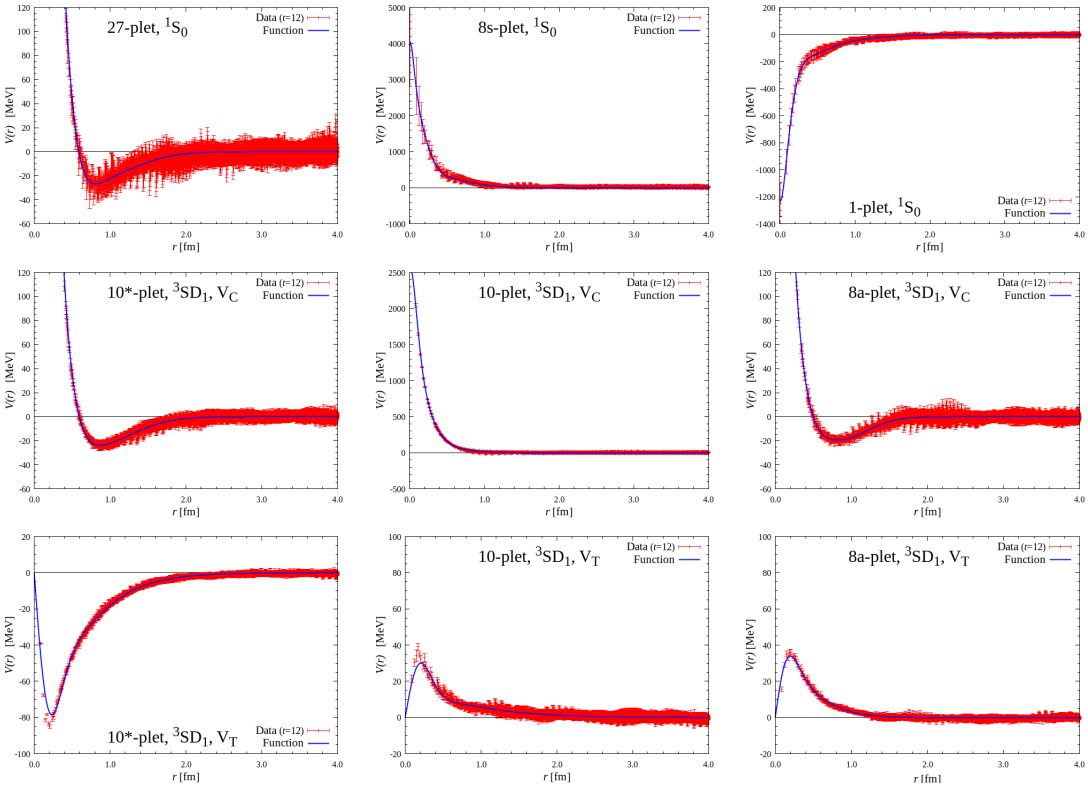

Figure 1.2: Potentials of baryon-baryon s-wave interactions diagonal in the flavor irreducible representation basis. These are obtained by rotating hyperon interaction potentials in the baryon-basis in strangeness $S = -2$ sector. [5]

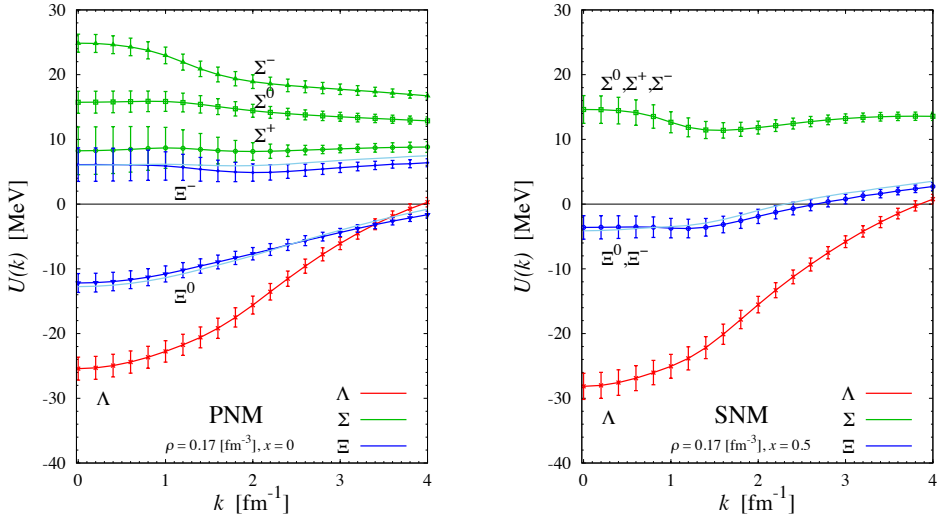

Figure 1.3: Hyperon single-particle potentials $U_Y(k)$ in nucleonic matter with the normal nuclear density, based on the hyperon interaction potentials from QCD on lattice. [5]

1.2 Hyperon puzzle

The interactions of YN and YY are important to discuss the structure of the neutron star (NS). Although the free hyperons are unstable against weak decays, in dense nuclear environment such as the inner core of the NS, the Pauli blocking prevents hyperons from decaying into nucleons. In the case that the nucleon chemical potential is large enough, the hyperon production is energetically favorable. Therefore, the equation of state (EOS) of NS becomes softer and the predicted maximum mass of NS becomes smaller than that without hyperon. However, massive NSs with almost twice solar masses have been observed recently [7, 8], which cannot be explained with various microscopic calculations having the hyperon appearance. This is as serious drawback of the present BB interaction models. Something exotic mechanisms are needed to sustain such heavy NSs in the high density condition. This problem is called "hyperon puzzle".

D. Lonardoni *et al.* calculated the EOS of NS with the auxiliary field diffusion Monte Carlo algorithm [9]. They found the three-body hyperon-nucleon interaction play a fundamental role in the softening of the EOS. Two types of the three-body force were constructed by changing the fitting parameters to reproduce the binding energy of medium mass hypernuclei. Figure 1.4 shows the relation between the mass and radius of NS. It is clearly found that the maximum mass becomes smaller by including Λ than pure neutron matter (PNM) and the three-body force makes the EOS stiffer. The model with $\Lambda N + \Lambda NN$ (II) is consistent with the observed very massive NSs. However, those effect is drastically different depending on the model and it is insensitive to the available binding energy of hypernuclei.

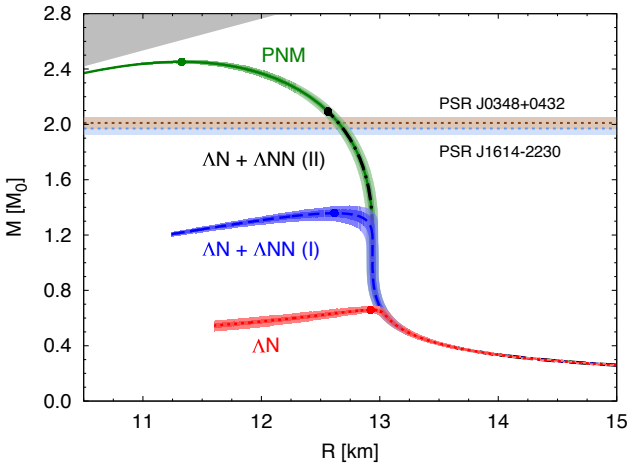

Figure 1.4: Mass-radius relations of NS in different interaction models. [9]

Additionally, odd-state parts of the $\Lambda\Lambda$ interaction are considered to be related to the structure of NS. H. Togashi *et al.* discussed the importance of odd-state parts of $\Lambda\Lambda$ interaction [10]. They estimated the EOS for symmetric nuclear matter preparing

four types of interaction with the cluster variational method. They found that the more repulsive $\Lambda\Lambda$ interaction predicted the larger maximum mass of NS. In addition, it is interesting that the threshold density of the onset of Σ hyperon depends on the odd-state $\Lambda\Lambda$ interaction, wheres that of Λ hyperon is insensitive to this interaction. However, the obtained maximum mass was still smaller than the observed massive NSs even with the most repulsive $\Lambda\Lambda$ interaction. Therefore, they introduced the universal three-body force which makes the maximum NS mass to 2.14 $M_\odot$ which was consistent with the observations. In this case, the difference of the $\Lambda\Lambda$ interaction in two body level becomes small.

In order to solve the puzzle, the three-body force is considered to be the key issue. Before that, however, we must understand the two-body BB interaction including YN and YY interactions which play an important role in not only NS but also hypernuclei. In order to extract a net interaction of two body and three body (and more) interactions, we need to decompose each interaction by observing hypernuclei systematically. In particular, data of $S = -2$ system is quite limited so far compared to that of $S = -1$ because of the experimental difficulty. Therefore, experiments with $S = -2$ are strongly awaited as a next step to investigate the BB interaction.

1.3 Previous experiments on $S = -2$ systems

The interaction between two baryons in the $S = -2$ sector is closely related to the existence of H-dibaryon, which belongs to the flavor singlet ($1s$) of $\mathrm{SU}(3)_f$ symmetry. H-dibaryon was originally predicted by Jaffe [11] as a $uuddss$ quark state with $I = 0$ and $J = 0$. A lot of QCD inspired models predicted such a deeply bound six quark state. While a lot of experiments were carried out to search for it, no conclusive evidence has been observed [12]. The existence of bound H nuclei contradicts with the weak decay of double-Λ hypernuclei, in which two Λ hyperons are bound in a nucleus, if the binding energy of H nuclei are deeper than the double-Λ hypernuclei. Since a sequential weak decay event was uniquely identified to be a ${}^{\ 6}_{\Lambda\Lambda}\mathrm{He}$ double-Λ hypernucleus with the $\Lambda\Lambda$ binding energy of $7.25 \pm 0.16\,\mathrm{MeV}$ [1] in an emulsion, the lower limit of H-dibaryon mass was obtained to be $2223.7\,\mathrm{MeV}/c^2$ [13]. Therefore, the ground state of double strangeness system is considered to be double-Λ hypernuclei. Although the existence of the deeply bound H-dibaryon was rejected, the possibility of its existence above the $\Lambda\Lambda$ threshold still remains. HAL QCD group calculated BB potentials from lattice QCD simulations with $\mathrm{SU}(3)_f$ symmetry [14]. They showed that a stable H-dibaryon exists in the flavor-singlet $J^P = 0^+$ channel with the binding energy of about 26 MeV with the mass of the pseudo-scalar-meson of 469 MeV. A new experiment to search H-dibaryon is planned in Japan Proton Accelerator Research Complex (J-PARC) [15].

Double-Λ hypernuclei are also searched for with decay π spectroscopy. The BNL-AGS E906 experiment was carried out to observe double-Λ hypernuclei by detecting two π^-s from sequential weak decays [16]. K^- beam with a momentum of $1.8\,\mathrm{GeV}/c$ was incident on a ${}^9\mathrm{Be}$ target surrounded with a cylindrical detector system. The momenta of π^- mesons were measured by tagging the (K^-, K^+) reaction. They observed the correlation

[1] The $\Lambda\Lambda$ binding energy was re-calculated because of the change of Ξ^- mass

between momenta of two π^- mesons which was interpreted to be the production of ${}^{4}_{\Lambda\Lambda}\mathrm{H}$ double-Λ hypernucleus and ${}^{4}_{\Lambda}\mathrm{H} + {}^{3}_{\Lambda}\mathrm{H}$ twin-Λ hyperfragments (Fig. 1.5). Sequential weak decays of ${}^{4}_{\Lambda\Lambda}\mathrm{H}$ can be ascribed to the following decay channels,

$$\begin{aligned} {}^{4}_{\Lambda\Lambda}\mathrm{H} &\to {}^{4}_{\Lambda}\mathrm{He}^{*} + \pi^- \qquad (\sim 104\,\mathrm{MeV}/c), \\ {}^{4}_{\Lambda}\mathrm{He}^{*} &\to {}^{3}_{\Lambda}\mathrm{H} + p, \\ {}^{3}_{\Lambda}\mathrm{H} &\to {}^{3}\mathrm{He} + \pi^- \qquad (114.3\,\mathrm{MeV}/c). \end{aligned}$$

However, this interpretation may not be unique. There is a claim that the correlation can be reproduced from the sequential decays of ${}^{7}_{\Lambda\Lambda}\mathrm{He}$ with a background of three single hypernuclear pairs, ${}^{3}_{\Lambda}\mathrm{H}$ with ${}^{4}_{\Lambda}\mathrm{H}$, ${}^{3}_{\Lambda}\mathrm{H}$ with ${}^{3}_{\Lambda}\mathrm{H}$, and ${}^{4}_{\Lambda}\mathrm{H}$ with ${}^{4}_{\Lambda}\mathrm{H}$ [17]. Additionally, A. Gal suggested the existence of ${}^{4}_{\Lambda\Lambda}n$ state and S. Bleser *et al.* reconsidered the interpretation of E906 data based on this assumption [18]. The enhancement of $(P_H, P_L) = (133, 114)\mathrm{MeV}/c$ in Fig. 1.5 was originally interpreted to be a signal of ${}^{4}_{\Lambda}\mathrm{H} + {}^{3}_{\Lambda}\mathrm{H}$ twin-Λ hypernucleus. However, they found that it is difficult to explain a sufficient amount of enhancement with the twin-Λ hypernucleus. Assuming the bound ${}^{4}_{\Lambda\Lambda}n$ production with a two-body π^- branching ratio of 50%, the E906 data can be described remarkably well in the statistical multifragmentation model. Though the existence of such neutral hypernucleus is still controversial, this may become a hint to solve the E906 puzzle. In order to observe a double-Λ hypernucleus in decay π spectroscopy without ambiguities, extremely good energy resolution and particle identification for decay particles are necessary. An upgraded experiment is planned in J-PARC to observe ${}^{5}_{\Lambda\Lambda}\mathrm{H}$ and ${}^{4}_{\Lambda\Lambda}\mathrm{H}$ with a ${}^{9}\mathrm{Li}$ target by tagging ${}^{7}_{\Xi}\mathrm{H}$ production (J-PARC P75).

In order to investigate the ΞN interaction, Ξ hypernuclei give important information. The missing mass spectroscopy in the (K^-, K^+) reaction is an effective way to produce Ξ hypernuclei. The AGS E885 experiment was carried out to produce doubly strangeness systems in the ${}^{12}\mathrm{C}(K^-, K^+)X$ reaction [4]. By irradiating a 5 cm-thick diamond target with $1.8\,\mathrm{GeV}/c$ K^- beam delivered at the AGS D6 beam line [19], a total of about 3×10^5 (K^-, K^+) events were collected. The momentum of the outgoing K^+ was measured with the 1.4 T 48D48 magnetic spectrometer. The experimental excitation energy spectra for ${}^{12}\mathrm{C}(K^-, K^+)X$ are shown in Fig. 1.6. The significant enhancement can be seen around production threshold energy compared to a Monte Carlo simulation based on quasi-free Ξ production (QF). The DWIA calculation was performed with the Woods-Saxon potential with the potential depth of $V_{0\Xi} = 12, 14, 16, 18$, and 20 MeV. The theoretical curve of $V_{0\Xi} = 14\,\mathrm{MeV}$ with the experimental resolution of $6.1\,\mathrm{MeV}/c^2$ (rms) shows good agreement with the data. However, the peak structure of the Ξ bound state could not be resolved because of the limited resolution.

J-PARC E05 experiment was carried out to confirm ${}^{12}_{\Xi}\mathrm{Be}$ hypernucleus in the ${}^{12}\mathrm{C}(K^-, K^+)$ reaction with $9.3\,\mathrm{g/cm^2}$ carbon target [20]. The energy resolution of missing mass was achieved to be 5.4 MeV by using a high resolution spectrometer system (SKS) to measure the momentum of the outgoing K^+. They observed excess in the binding region of the missing mass spectrum. The analysis is ongoing. An upgrade experiment with a new spectrometer, S-2S, is planned at J-PARC (E70). [21]. The expected resolution for the missing mass spectrum is 2 MeV which enables us to observe the peak structures of core excited states of Ξ hypernuclei.

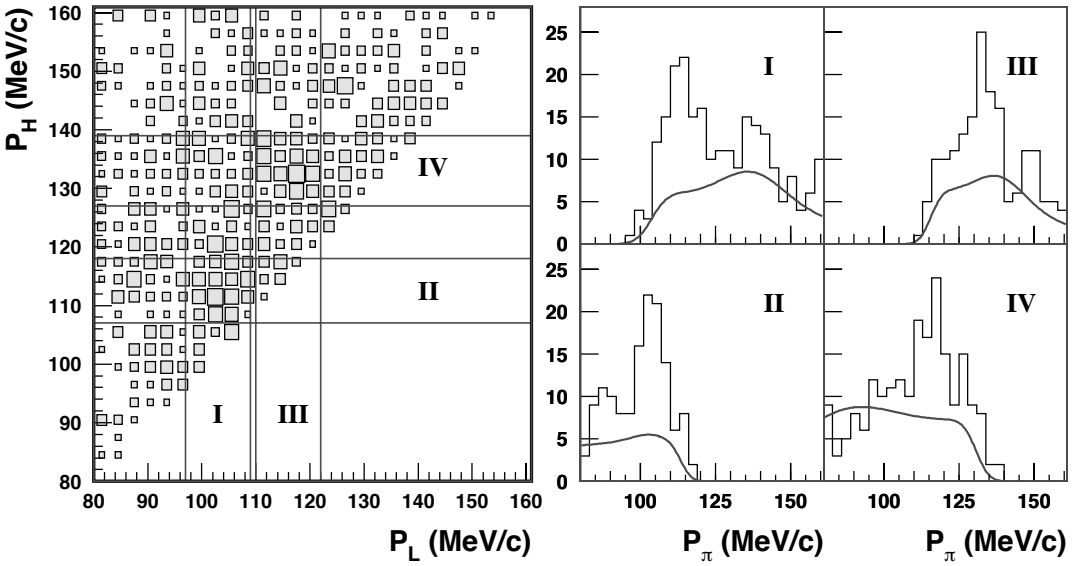

Figure 1.5: The distribution of π^- momentum observed in the BNL-AGS E906 experiment. (Left) The momentum correlation between two π^- mesons. (Right) The projections of bands where labeled with I–IV. The cross region of I and II suggest the ${}^{4}_{\Lambda\Lambda}\mathrm{H}$ event ($\sim 104\,\mathrm{MeV}/c + 114.3\,\mathrm{MeV}/c$). The cross region of III and IV suggest the ${}^{4}_{\Lambda}\mathrm{H}(132.9\,\mathrm{MeV}/c) + {}^{3}_{\Lambda}\mathrm{H}(114.3\,\mathrm{MeV}/c)$ event. [16]

Twin-Λ hypernuclei in emulsions are also an effective approach to study Ξ hypernuclei. When Ξ^- is captured with a nucleus, two single-Λ hypernuclei are expected to be produced in a few % probability. These events can be identified with their decay topology. Since the mass of single-Λ hypernuclei are well known through the past measurements, the mass of initial state, Ξ^--A system, can be estimated from the kinematics. The KISO event is the first evidence of the deeply bound Ξ^- nucleus system, Ξ^--${}^{14}\mathrm{N}$ [22]. This event was observed in the KEK-PS E373 experiment and ascribed to the following decay process:

$$ {}^{14}\mathrm{N} + \Xi^- \rightarrow {}^{10}_{\Lambda}\mathrm{Be} + {}^{5}_{\Lambda}\mathrm{He} $$

with the Ξ^- binding energy (B_{Ξ^-}) of $1.03 \pm 0.18\,\mathrm{MeV}$ or $3.87 \pm 0.21\,\mathrm{MeV}$. Since the state of daughter single-Λ hypernucleus ${}^{10}_{\Lambda}\mathrm{Be}$ was not uniquely identified, two interpretations are possible for the B_{Ξ^-} depending on the excitation energy of the ${}^{10}_{\Lambda}\mathrm{Be}$.

The ALICE collaboration performed a femtoscopy analysis to investigate BB interactions [23]. They analyzed the data of p-p collision at $\sqrt{s} = 7\,\mathrm{TeV}$ at Large Hadron Collider in CERN. They measured a correlation function which is defined as follows:

$$ C(p_1, p_2) \equiv \frac{P(p_1, p_2)}{P(p_1)\dot{P}(p_1)}, \tag{1.2} $$

where p_1, p_2 denote the momentum of each particle. The correlation function is the

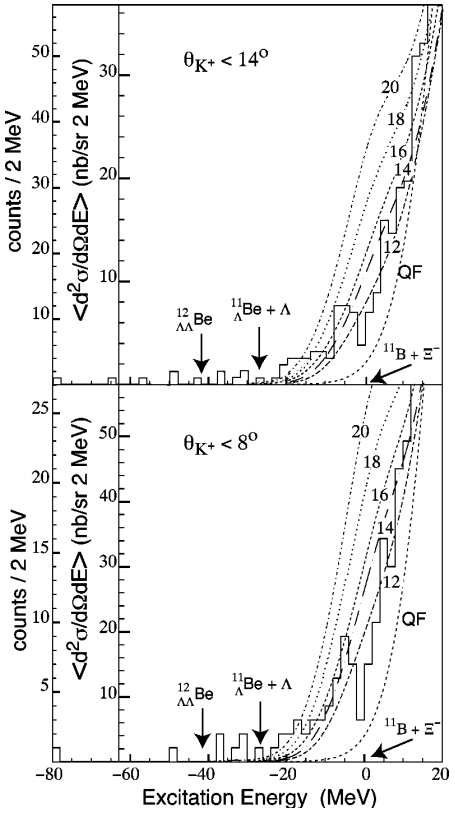

Figure 1.6: The experimental excitation energy histograms for $^{12}\mathrm{C}(K^-, K^+)X$. The top figures shows $\theta_{K^+} < 14°$ (full acceptance) region and the bottom figure shows $\theta_{K^+} < 8°$ region. Thresholds for $^{11}\mathrm{B} + \Xi^-$ and $^{11}_{\Lambda}\mathrm{Be} + \Lambda$ production and the expected location of $^{12}_{\Lambda\Lambda}\mathrm{Be}$ are indicated as arrows. [4]

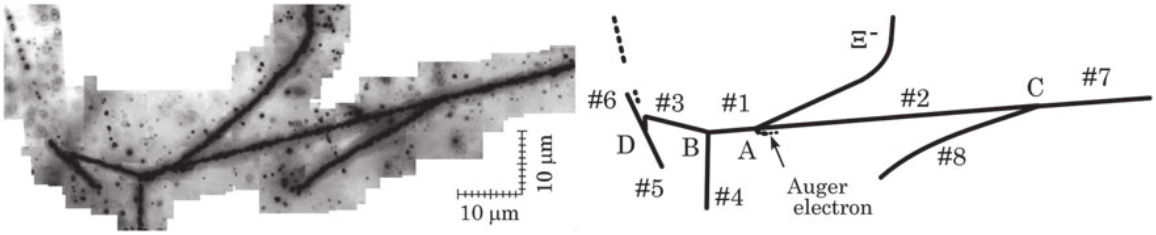

Figure 1.7: The Photograph and its schematic drawing of the KISO event. [22]

probability to find simultaneously two particles divided by the product of the corresponding single-particle probabilities. If there exist attraction between tow particles, an enhancement is expected, while in the absence of a correlation signal, $C(p_1, p_2)$ equals unity. The experimental correlation function might be distorted due to contaminations of feed-down particles from strong and weak decays. In order to extract the genuine correlation functions of interest from the signal, they developed a method to compute

the contributions arising from impurities and decaying resonances.

Figure 1.8 shows the correlation functions of p-p, Λ-p, and Λ-Λ. The p-p correlation function is well described by Argonne ν_{18} NN potential [24] with s- and p-waves.

For the case of p-Λ correlation function, the NLO parameter set obtained within the framework of chiral effective field theory is consistent with the data, but other models are also found to be in agreement with the data. The present pair data in the Λ-Λ channel allows us to constrain the available scattering parameter space. They found the interactions between Λ-Λ is attractive. Exclusion plot of the relation between the scattering length and the effective range is shown in Fig. 1.9.

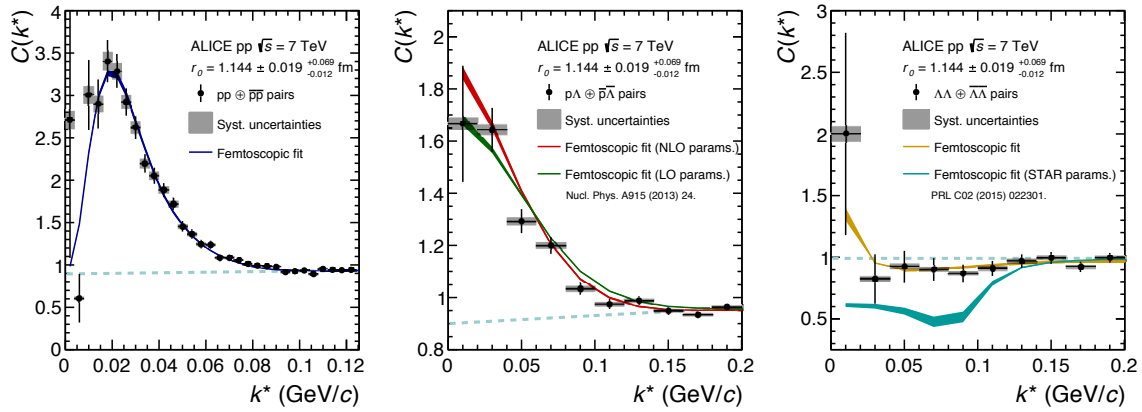

Figure 1.8: The correlation function of p-p (left), Λ-p (middle), and Λ-Λ (right) in terms of the relative momentum of the pair. [23]

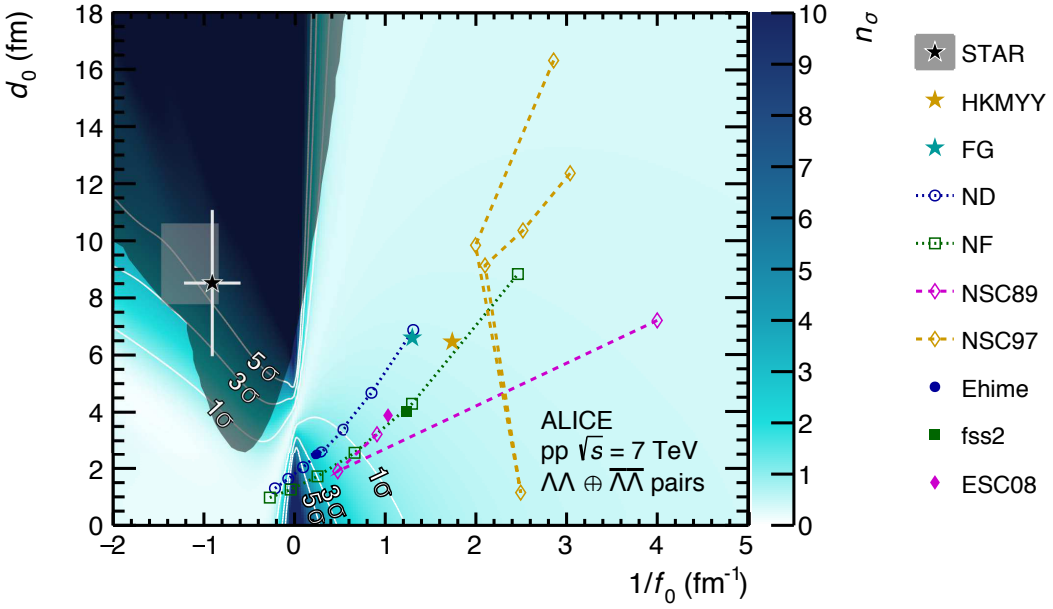

Figure 1.9: Exclusion plot of the relation between the scattering length and the effective range of $\Lambda\Lambda$ pair. [23]

The larger data sample of the LHC Run 2 and Run 3 are expected to have 10 and 100 times more yields, respectively. With these data, they can extend the current method to other hyperon systems such as Σ, Ξ, and Ω. They also analyzed $\Xi^- p$ data and confirmed the $\Xi^- p$ interaction is attractive. It is consistent with the calculation by the HAL QCD group.

1.4 Double-Λ hypernuclei observed in emulsions

Double-Λ hypernuclei have been investigated to study the ΛΛ interaction. Mass of a double-Λ hypernucleus, $M({}^{A}_{\Lambda\Lambda}Z)$, is measured in an experiment and the binding energy, $B_{\Lambda\Lambda}({}^{A}_{\Lambda\Lambda}Z)$, is obtained as

$$B_{\Lambda\Lambda}({}^{A}_{\Lambda\Lambda}Z) = M({}^{A-2}Z) + 2M(\Lambda) - M({}^{A}_{\Lambda\Lambda}Z). \tag{1.3}$$

From that, the ΛΛ bonding energy is calculated as

$$\Delta B_{\Lambda\Lambda}({}^{A}_{\Lambda\Lambda}Z) = B_{\Lambda\Lambda}({}^{A}_{\Lambda\Lambda}Z) - 2B_{\Lambda}({}^{A-1}_{\Lambda}Z), \tag{1.4}$$

where B_Λ represent the binding energies of a Λ hyperon in a single hypernucleus. The $\Delta B_{\Lambda\Lambda}$ indicates the binding energy between the two Λ hyperons by assuming that the binding energy of a Λ hyperon in a nucleus does not change from single-Λ hypernucleus. Since the double-Λ hypernucleus has two Λ hyperons in a nucleus, it shows typical event pattern in an emulsion. Emulsion experiment is one of the most efficient method to identify double-Λ hypernuclei. Emulsion is a kind of photographic sheet which contains AgBr crystals. It can record tracks of charged particles with sub-μm position resolution, which is good enough to separate their weak decay vertices. Additionally, their kinetic energies can be determined with $\Delta E/E \sim 1\%$ accuracy with their ranges. Therefore, the mass of double-Λ hypernuclei can be reconstructed with a good resolution, typically $\sim$ 0.2 MeV, by kinematic analysis of their production and decay vertices. Several emulsion experiments were performed to search for them.

The first double-Λ hypernucleus event was observed by Danysz in 1963 in an experiment at CERN [25]. K^- beam with a momentum of 1.5 GeV/c was injected into the emulsion. A Ξ^- hyperon emitted from the interaction point of K^- came to rest after flying a distance of 357 μm. At the Ξ^- stopping point, two π^- mesons were emitted from different vertices. This event was interpreted as the mesonic cascade decay of a double-Λ hypernucleus of ${}^{10}_{\Lambda\Lambda}$Be or ${}^{11}_{\Lambda\Lambda}$Be. The $\Delta B_{\Lambda\Lambda}$ values were obtained to be 4.5 ± 0.4 MeV and 3.2 ± 0.6 MeV for ${}^{10}_{\Lambda\Lambda}$Be and ${}^{11}_{\Lambda\Lambda}$Be, respectively.

The counter-emulsion hybrid method was adopted for the first time to observe double-Λ hypernuclei in the KEK-PS E176 experiment [26]. A Ξ^- hyperon in the emulsion was searched from the reaction vertex which was detected by tracing K^+ meson from the downstream. Emulsion sheets with a changeable sheet (CS) which was located at the downstream side were irradiated by 1.66 GeV/c K^- beam. The CS was changed 10 or 12 times in an exposure cycle to reduce the track density for the K^+ detection. Silicon strip detectors (SSDs) were installed to sandwich the emulsion sheets to measure K^+ track precisely. A K^+ meson detected in CS from the SSD prediction was traced in emulsion sheets to detect the $p(K^-, K^+)\Xi^-$ vertex. Among 98 candidates of Ξ^- stopping events,

four events showed the sequential weak decay topology. One event (#15-03-37) was identified as the production and decay of ${}^{10}_{\Lambda\Lambda}$Be or ${}^{13}_{\Lambda\Lambda}$B [27]. The $B_{\Lambda\Lambda}$ values for each mode were obtained to be 8.5 ± 0.7 MeV and 27.6 ± 0.7 MeV, respectively.

The most impressive results were obtained in the KEK-PS E373 experiment. In order to observe double-Λ hypernuclei efficiently, a counter-emulsion hybrid method with scintillating-fiber detectors was adopted. From about 700 Ξ^- stopping events, seven double-Λ hypernuclear events were observed. Among them, an event was uniquely identified as ${}^{6}_{\Lambda\Lambda}$He [13]. This event was called "NAGARA" (Fig. 1.10 (a)). From this event, $\Lambda\Lambda$ interaction, especially its s-wave (${}^1S_0$) interaction, is found to be weakly attractive. The $B_{\Lambda\Lambda}$ and $\Delta B_{\Lambda\Lambda}$ were obtained to be 6.91 ± 0.16 MeV and 0.67 ± 0.17 MeV, respectively [28]. This event became a standard to evaluate the $\Lambda\Lambda$ interaction. It should be noted that $B_{\Lambda\Lambda}$ and $\Delta B_{\Lambda\Lambda}$ depend on the Ξ^- binding energy (B_{Ξ^-}). Here, the Ξ^- hyperon was assumed to be captured in the atomic 3D state of ^{12}C, in which case the B_{Ξ^-} value was estimated to be 0.13 MeV [29].

Stimulated from this result, the past double-Λ hypernuclear events were re-examined. The double-Λ hypernucleus observed by Danysz was considered to be another decay modes. By considering an excited state of ${}^{9}_{\Lambda}$Be which is a decay daughter of the double-Λ hypernucleus, the following decay mode was found to be consistent with the NAGARA event.

$$
\begin{aligned}
{}^{16}\mathrm{O} + \Xi^- &\rightarrow {}^{10}_{\Lambda\Lambda}\mathrm{Be} + {}^{2}\mathrm{H} + n, \\
&\hookrightarrow {}^{9}_{\Lambda}\mathrm{Be}^* + p + \pi^-.
\end{aligned}
$$

The $\Delta B_{\Lambda\Lambda}$ value was re-evaluated and found to be decreased by 3 MeV the excitation energy of ${}^{9}_{\Lambda}$Be*. Thus, the $B_{\Lambda\Lambda}$ and $\Delta B_{\Lambda\Lambda}$ values were calculated to be 14.7 ± 0.4 MeV and 1.3 ± 0.4 MeV, respectively [30–32].

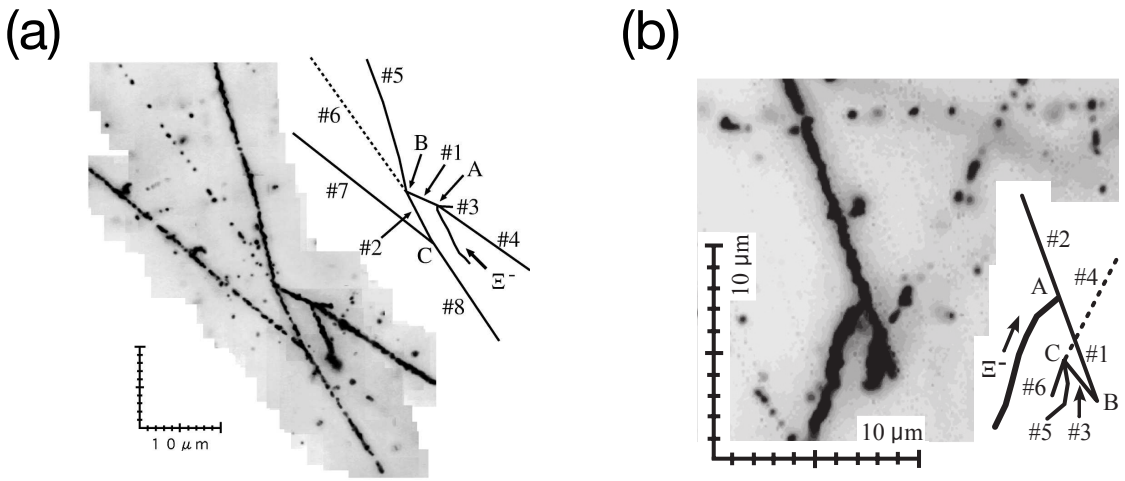

Figure 1.10: Photographs of NAGARA event (a) and DEMACHIYANAGI event (b), which are observed in the KEK E373 experiment. [28]

DEMACHIYANAGI event is another impressive double-Λ hypernucleus observed in the E373 experiment [Fig. 1.10 (b)]. The most probable interpretation of this event was

${}^{10}_{\Lambda\Lambda}$Be with $B_{\Lambda\Lambda}$ of 11.90 ± 0.13 MeV and $\Delta B_{\Lambda\Lambda}$ of -1.52 ± 0.15 MeV [28]. The $\Delta B_{\Lambda\Lambda}$ value is negative; it is not consistent with NAGARA event, if a double-Λ hypernuclus was generated as an excited state, the $\Delta B_{\Lambda\Lambda}$ value of the ground state become increased by its excited energy. E. Hiyama *et al.* calculated the energy level of ${}^{10}_{\Lambda\Lambda}$Be with the Gaussian expansion method, in which the Λ-Λ interaction was tuned to reproduce the NAGARA result [33]. The $\Delta B_{\Lambda\Lambda}$ value from the DEMACHIYANAGI event is close to that for the NAGARA event assuming an excited level (2^+) of ${}^{10}_{\Lambda\Lambda}$Be.

There were several other double-$\Lambda\Lambda$ events observed in the E373 experiment. Unfortunately, they were not uniquely interpreted and errors of $\Delta B_{\Lambda\Lambda}$ were large because of a neutron emission at the production vertex of double-Λ hypernuclei.

Since the NAGARA event was uniquely identified, $\Lambda\Lambda$ ${}^1S_0$ interaction in ${}^{6}_{\Lambda\Lambda}$He was determined with good energy accuracy. However, the $\Delta B_{\Lambda\Lambda}$ value may change according to the change of core nucleus structure due to the existence of one more Λ. Moreover, other related interactions such as p-wave information of $\Lambda\Lambda$, $\Lambda\Lambda$-ΞN mixing are totally unknown. In particular, the $\Lambda\Lambda$-ΞN mixing is important on light s-shell double-Λ hypernuclei. In case of p-shell double-Λ hypernuclei, $\Lambda\Lambda$-ΞN mixing is suppressed due to the Pauli blocking because $1s$ orbits of nucleons are occupied. On the other hand, $\Lambda\Lambda$ binding energy of s-shell double-Λ hypernuclei such as ${}^{4}_{\Lambda\Lambda}$H, ${}^{5}_{\Lambda\Lambda}$H, is considered to be sensitive to the $\Lambda\Lambda$-ΞN mixing.

Several groups calculated the structure of unobserved double-Λ hypernuclei and their results depend on the model [35, 66–68]. Therefore, it is necessary to measure the $\Lambda\Lambda$ binding energy in several double-Λ hypernucleus species systematically to guide the theoretical works.

1.5 J-PARC E07 experiment

The J-PARC E07 experiment is an upgraded counter-emulsion hybrid experiment to accumulate 10 times more statistics than that of E373 [34]. Such enormous amount of double-Λ hypernuclear events can be collected due to high intensity and high purity K^- beam provided from the J-PARC accelerator. We were able to increase the emulsion volume and enhance the K^- purity from E373. Additionally, the acceptance of spectrometer to detect the outgoing particles was enlarged. The difference between E373 and E07 experiments is listed in Table 1.2. Since the classical emulsion scanning with a microscope by human eyes took a long time to analyze the whole volume, we developed an automated microscope scanning system. From a prediction of Ξ^- position and angle obtained with silicon strip detectors, Ξ^- tracks in emulsion can be automatically traced. It is expected to detect 100 double-Λ hypernuclei events including new species among 1×10^4 Ξ^- stopping events. They provide us useful knowledge of the $\Lambda\Lambda$ interaction depending on their species. If we observe a p-shell double-Λ hypernucleus, it can examine the model calculation based on the NAGARA event. In case of a light s-shell double-Λ hypernucleus, the strength of the $\Lambda\Lambda$-ΞN mixing can be determined. There is a possibility to obtain the information of $\Lambda\Lambda$ p-wave interaction by detecting an excited state of a double-Λ hypernucleus. We can reveal the $S = -2$ interactions in $\Lambda\Lambda$ hypernuclei.

Beam exposure of E07 was carried out in 2016 and 2017. A total of 2.1 tons of emulsion was exposed to 1.13×10^{11} K^- beam. An impressive new double-Λ hypernuclear

Table 1.2: Comparison between E373 and E07 run conditions.

Experiment	Emulsion volume [t]	number of K^- [$\times 10^9$]	K^- purity [%]	acceptance [msr]
KEK-PS E373	0.8	14	25	170
J-PARC E07	2.1	113	82	280

event, "MINO", was observed after scanning 30% of all emulsion volume. In this thesis, an interpretation of this event is discussed.

1.6 Thesis composition

The setup of this experiment is described in Chapter 2. Chapter 3 and 4 provide the analysis of spectrometer systems and emulsion microscope system, respectively. An interpretation "MINO" event is discussed in Chapter 5. Finally, the present result is summarized in Chapter 6.

Chapter 2

Experiment

2.1 Outline

The J-PARC E07 experiment was carried out at the K1.8 beam line in the J-PARC Hadron Experimental Facility with K^- beams of 1.8 GeV/c momentum. This momentum was chosen to maximize the Ξ^- stopping yield in emulsions. Typical intensity and purity of the K^- beam were 2.8×10^5 particles per spill of 2.0 s duration every 5.52 s and 82%, respectively. Incoming K^- and outgoing K^+ were momentum analyzed in each corresponding magnetic spectrometer, the beam line spectrometer [37] and the KURAMA spectrometer, respectively. Momentum resolution of each spectrometer was $\Delta p/p = 3.3 \times 10^{-4}$ (FWHM) and $\Delta p/p = 2.7 \times 10^{-2}$ (FWHM), respectively. The acceptance of the KURAMA spectrometer was 280 msr at 1.0-1.4 GeV/c.

The primary proton beam with a kinetic energy of 30 GeV was delivered from the J-PARC main ring (MR) to the production target (T1). Typical beam power of the primary beam was about 40 kW for the present experiment. The target was a gold bar with a size of 15 mm (W) × 6 mm (H) × 66 mm (T). Secondary beams produced from the target were extracted to the K1.8 beam line with an extraction angle of 6°.

A Ξ^- hyperon was produced through the quasi-free (K^-, K^+) reaction off a diamond target with 30-mm thickness (9.83 g/cm^2) and was injected into an emulsion module with a recoil momentum of about 550 MeV/c. It subsequently slowed down and was captured in a Ξ^- atomic orbit of the nucleus contained in the emulsion material. A bound state of double-Λ hypernucleus was eventually produced by the interaction between the Ξ^- hyperon and the nucleus with a probability of a few %. As shown in Fig. 2.1, an emulsion module was sandwiched with two sets of silicon strip detectors (SSDs). A K^+ track and Ξ^- track were traced with these SSDs. When the double-Λ hypernucleus was produced, decay particles would escape from the module. These tracks were also traced with SSDs.

The emulsion sheets were photographically developed after the beam exposure and analyzed by micro scope systems. A Ξ^- track was traced from the upstream of an emulsion module to find a double-Λ hypernucleus supported by the predictions of the Ξ^- position and angle obtained with the SSD. This method is called "counter-emulsion hybrid method".

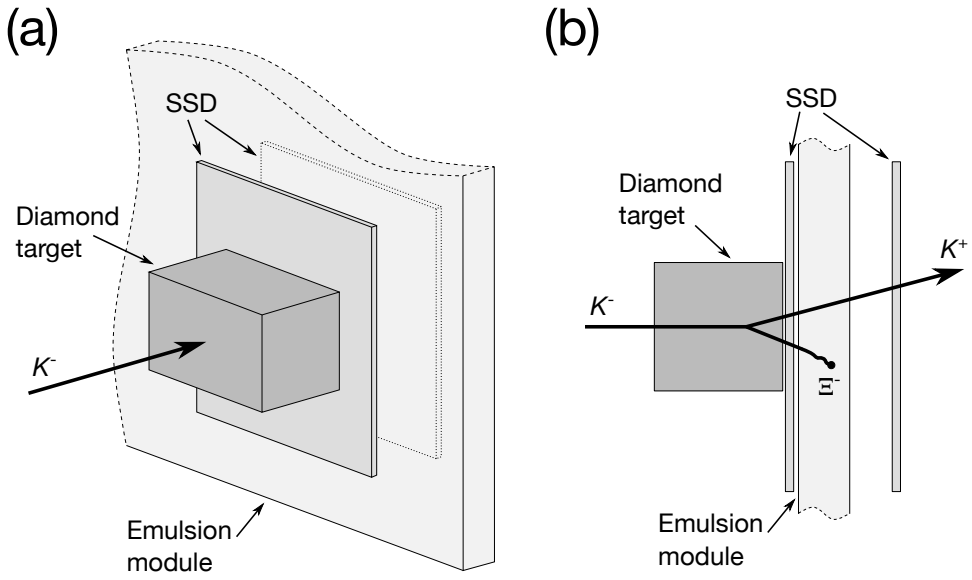

Figure 2.1: Schematic drawing of experimental setup of E07 around a diamond target. The target size was 50 mm (W) × 30 mm (H) × 30 mm (T).

2.2 J-PARC K1.8 beam line

The K1.8 beam line is a multi-purpose beam line which can deliver various secondary hadron beams. This beam line was designed to conduct $S = -2$ physics with the (K^-, K^+) reaction with high intensity and large K^-/π^- ratio. Its maximum momentum, 2.0 GeV/c, was set because the cross section of Ξ^- production has a maximum at K^- beam momentum of 1.8 GeV/c. In order to separate K^- from π^-, two electrostatic separator (ESS) systems were implemented. Figure 2.2 shows the schematic drawing of the K1.8 beam line. This beam line consists of three sections which are the upstream section, mass separation section, and momentum analysis section.

upstream section

Two dipole magnets (D1 and D2) and two quadruple magnets (Q1 and Q2) were equipped in the upstream section. The momentum of the extracted secondary beam was determined by the D1 magnet setting. Two intermediate focus slits, IFH (horizontal) and IFV (vertical), were installed to reject cloud pions. They were produced from the decay of K^0_s. The scattered pions from materials in the upstream section would be also rejected with these slits. IF slits consisted of a 30-cm thick brass block.

mass separation section

A dipole magnet (D3), seven quadruple magnets (Q3–Q9), four sextuple magnets (S1–S4), three octupole magnets (O1–O3) and two electrostatic separators (ESS1 and ESS2) with four correction magnets (CM1–CM4) were equipped in the mass separation section. Two sets of mass separation systems were essential components of the K1.8 beam line to select K^- beam in high purity. The mass separation system consisted of electrostatic

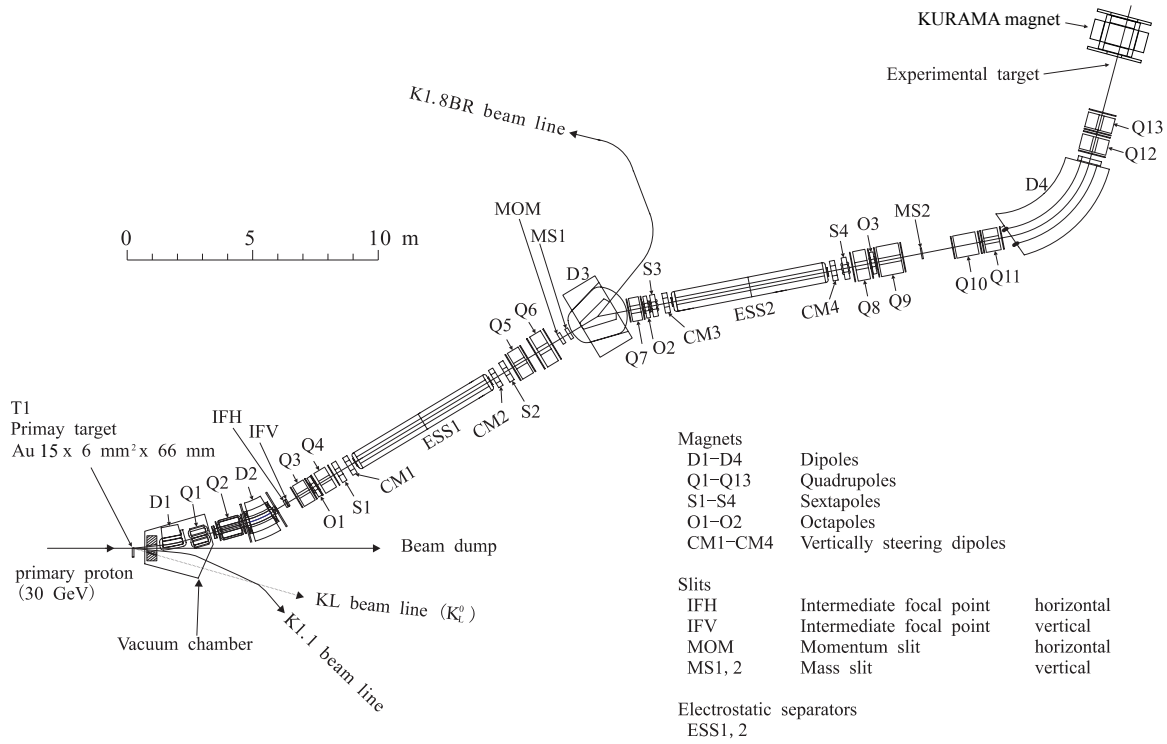

Figure 2.2: Schematic drawing of the K18 beam line.

separators sandwiched by two correction magnets. Each electrostatic separator generated a high electric field with a gap of 10 cm between parallel electrode plates with a width of 30 cm and a length of 6 m. In the present experiment, the gradient of the electric field was set to 50 kV/cm.

In order to make the central beam trajectory parallel to the ground, two correction magnets which have dipole were installed at the entrance and the exit of a electrostatic separator. After ESS1 and ESS2, the beam trajectory was focused vertically and momentum dispersion became large horizontally. Mass slits (MS1 and MS2) were installed at the focusing positions to select target particles by their masses. A momentum slit (MOM) was installed to define the momentum bite of the secondary particles.

momentum analysis section

The momentum analysis section called K1.8 beam line spectrometer was installed at the end of K1.8 beam line. The detail of this section is written in Sec.2.2.1.

2.2.1 K1.8 beam line spectrometer

Figure 2.3 shows the schematic drawing of the K1.8 beam line spectrometer. A dipole magnet (D4) and four quadruple magnets (Q10–Q13) were installed to construct QQDQQ system. The beam was focused on the experimental production target and its momentum was analyzed. A collimator consisted of heavy metals was installed at the exit of K1.8 beam spectrometer to kill beam halo. The typical size of the beam at the

target position for X and Y were 7.6 mm(σ) and 5.3 mm(σ), respectively (Fig. 2.4).

The beam momentum was reconstructed from the horizontal position at the entrance and the trajectory at the exit of QQDQQ system with third-order transfer matrix. The specifications of detectors are listed in Table 2.1. The momentum resolution was estimated as $\Delta p/p = 3.3 \times 10^{-4}$ (FWHM) in the past experiment [37]. The central momentum of the incident trajectory was determined by the magnetic field of the dipole magnet (D4). In order to monitor the fluctuations of the magnetic field, a high precision Hall probe [Digital Teslameter 151 (DTM-151)] was installed in the D4 magnet. The observed fluctuation (ΔB/B) was $\pm$0.5%.

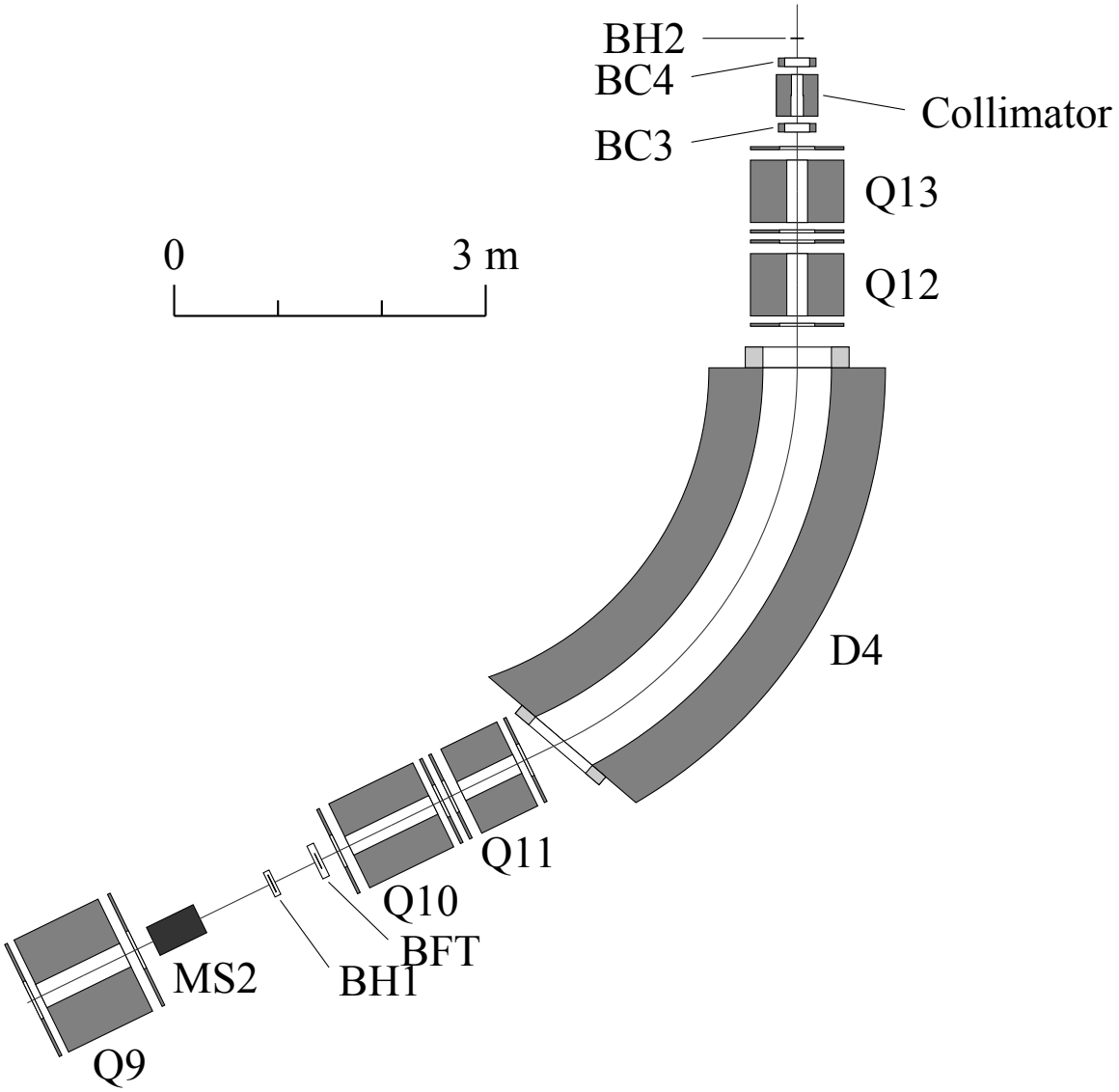

Figure 2.3: K1.8 Beam line spectrometer.

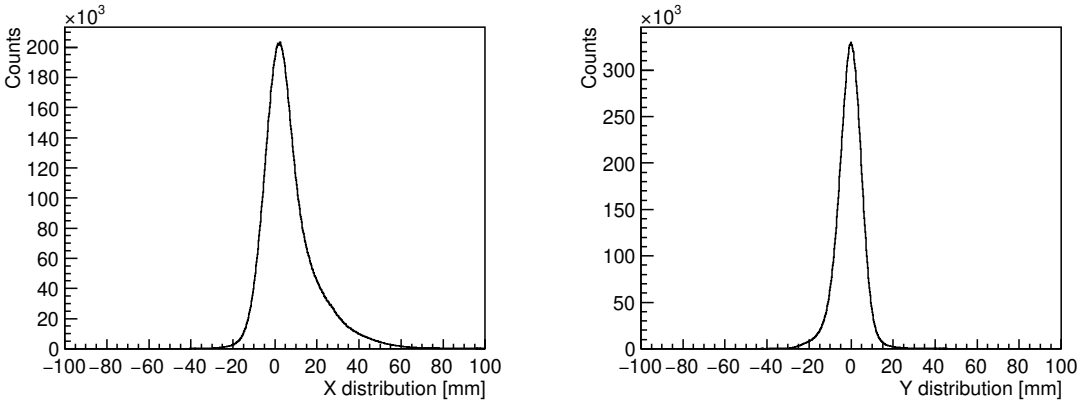

Figure 2.4: Distribution of K^- beam at the target position.

Table 2.1: The specifications of detectors in the K1.8 beam line spectrometer.

Detector	Scintillator	Segments	Effective area (W) × (H) [mm]	Readout
BH1	Saint-Gobain BC-420	11	170 × 66 × 5	PMT (Hamamatsu H6524MOD)

Detector	plane	fiber size ϕ [mm]	Effective area (W) × (H) [mm]	Readout
BFT	XX'	1	160 × 80	MPPC (Hamamatsu S10362-11-100P)

Detector	plane	wire pitch [mm]	Effective area (W) × (H) [mm]	gas
BC3	XX'VV'UU'	3.0	192 × 100	Ar(76%) + iso-C_4H_{10}(20%) + methylal(4%)
BC4	UU'VV'XX'	3.0	192 × 100	Ar(76%) + iso-C_4H_{10}(20%) + methylal(4%)

collimator

Since the emulsion sheet records all charged particles, the particle density must be controlled to keep good analysis quality. In order to suppress the beam halos, a collimator was installed between BC3 and BC4. The collimator was composed of tungsten blocks near the beam and of lead blocks outer side. Figure 2.5 shows the schematic drawing of the collimator. This configuration was determined by measuring the beam size at the collimator position. Typical beam profile is shown in Fig. 2.6.

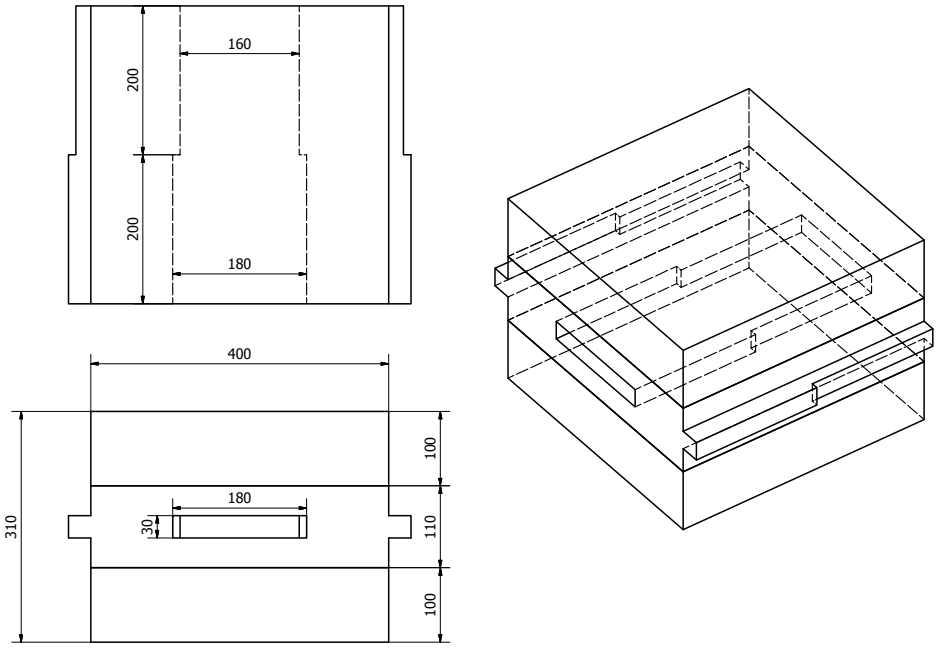

Figure 2.5: Schematic drawings of a collimator.

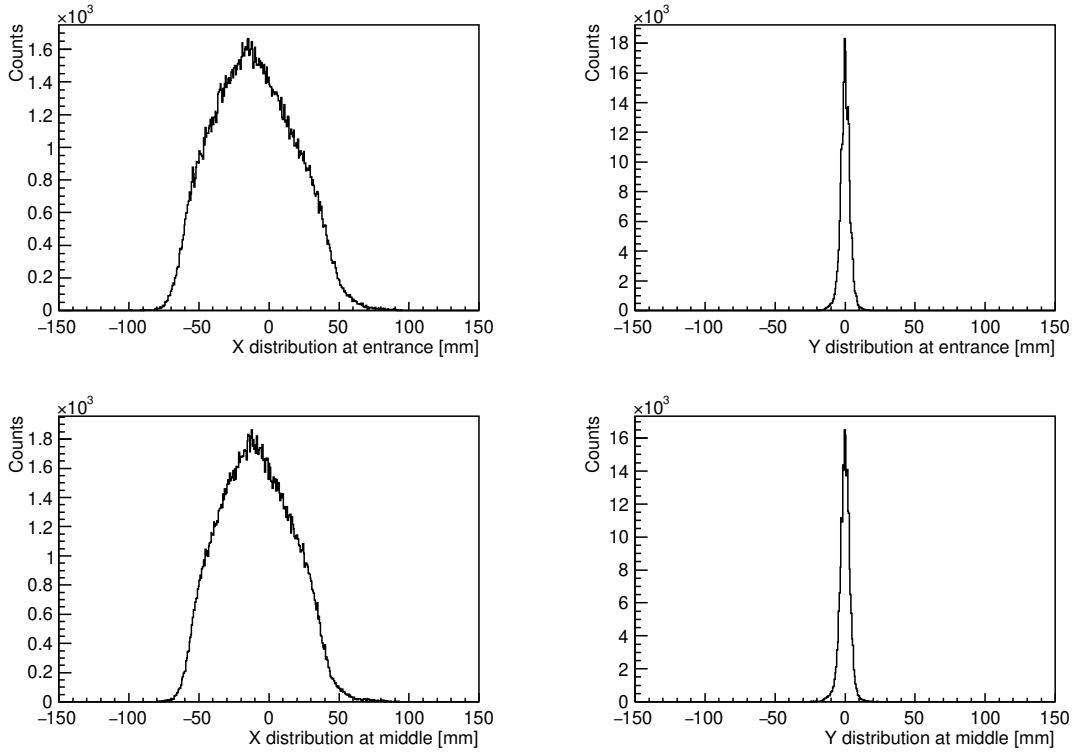

Figure 2.6: Distribution of K^- beam at the entrance (a) and the middle (b) of the collimator.

BH1

The beam hodoscope 1 (BH1) was located at the entrance of the K1.8 beam line spectrometer to measure the time of flight of incident particles. It consisted of eleven segments of scintillation counters with a thickness of 5 mm. In order to accept a high rate beam, the width of each scintillator was optimized by taking into account the beam rate at each position. The total effective area was 170 mm (W) × 66 mm (H). Scintillation signals were read by PMTs (Hamamatsu H6524MOD) on the top and bottom of scintillator through acrylic light-guides. Figure 2.7 shows the schematic drawing.

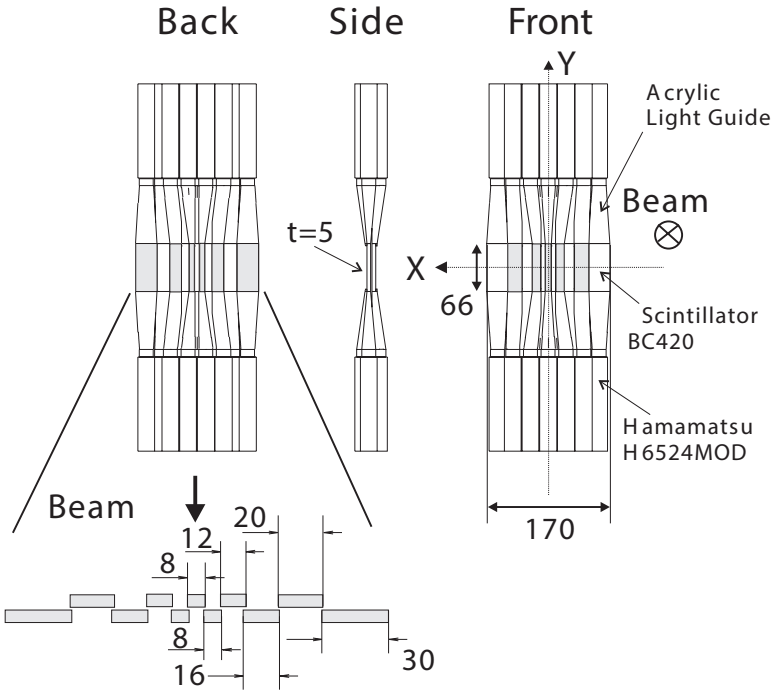

Figure 2.7: Schematic drawings of BH1.

BFT

The beam fiber tracker (BFT) was located downstream of BH1 to measure the incident position of the beam. Beam trajectory was focused horizontally at the position. The effective area of BFT was 160 mm (H) × 80 mm (W). BFT has a two-layers configuration (XX) consisted of cylindrical scintillation fibers (Kuraray SCSF-78MJ) with a diameter of 1 mm. Scintillation signals were read by MPPCs (Hamamatsu S10362-11-100P) attached at an end of each fiber. The position resolution is estimated to be 180 μm (σ). Figure 2.8 shows the schematic drawing.

BC3 and BC4

Two sets of multi-wire drift chambers were located at the exit of the K1.8 beam line spectrometer to measure the beam trajectory. Both chambers have a six layers configuration (XX'UU'VV') with 3-mm wire spacing. Figure 2.9 shows the schematic drawing

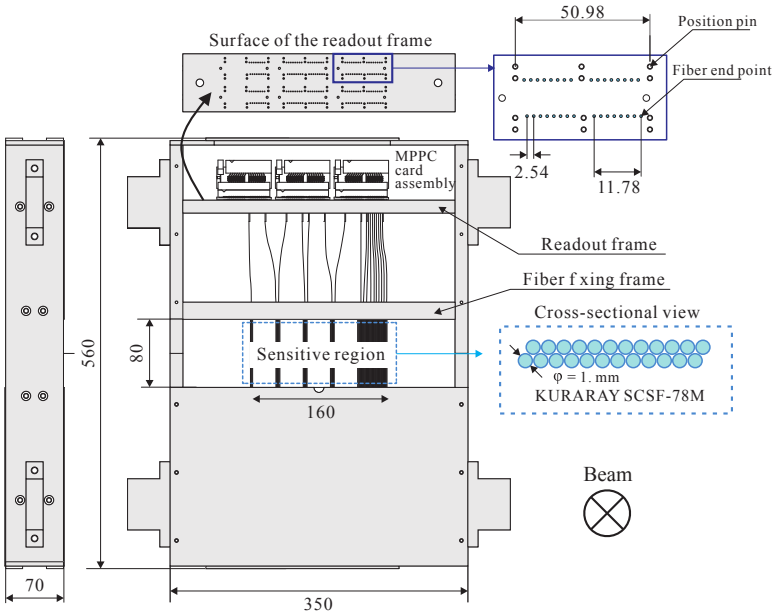

Figure 2.8: Schematic drawings of BFT.

of BC3,4. U and V planes are tilted +15° and −15°, respectively. Anode wires and potential wires consisted of tungsten with a diameter of 12.5 μm and gold-plated tungsten with a diameter of 75 μm, respectively. A set of two layers, XX', UU', and VV', are called as a pair plane in which two layers are shifted by 1.5 mm, which corresponds to a half size of the cell. The left/right ambiguity of each wire hit for a straight track can be solved by checking the hit combination in the pair plane as shown in Fig 2.9(c). This method helps us to analyze data efficiently. Each layer was separated by cathode plane which consisted of a 12 μm aramid film on which 20 μm graphite was pasted. A mixed gas of Ar(76%), iso-C_4H_{10}(20%), and methylal(4%) was filled in BC3 and BC4. Methylal was mixed to prevent anode wires from sputtering caused by beam particles. The inner pressures of chambers were kept positive to prevent contamination of outer air by keeping gas flowing continuously. A raw signal from each wire was read by Amplifier Shaper Discriminator (ASD) card attached on the chamber. A high voltage of −1.22 kV for cathode and −1.25 kV for potential wires were applied to BC3 and BC4 in operation, respectively.

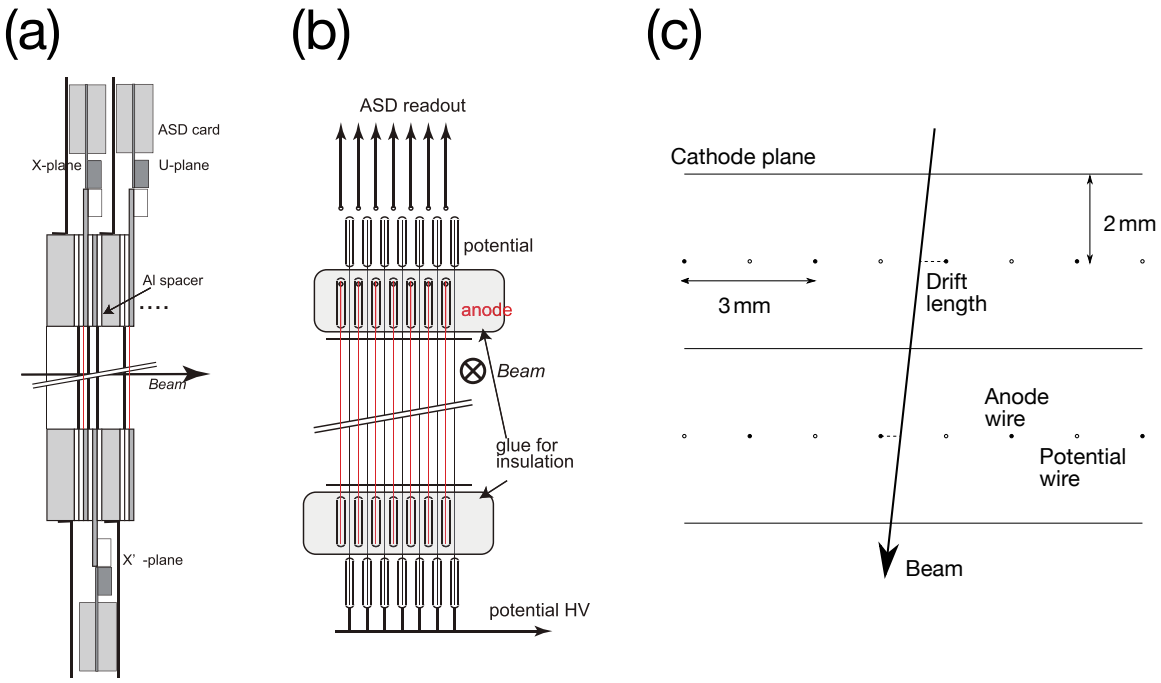

Figure 2.9: Schematic drawings of BC3 and BC4. Both chambers had a same wire configuration.

2.3 KURAMA spectrometer

The KURAMA spectrometer, which was also used in the KEK E373 experiment, consisted of a dipole magnet (KURAMA) and detectors located at the entrance and exit of it. Figure 2.10 shows the schematic drawing of the KURAMA spectrometer and the specifications of detectors is listed in Table 2.2-2.4. The momentum of scattered particles was analyzed by the Runge-Kutta method [39]. The strength of the central magnetic field of the KURAMA magnet was 0.7 T by applying a current of 2400 A. End-guards were attached on the entrance and exit of the magnet to reduce the fringing field. In order to monitor fluctuations of the magnetic field, an NMR probe was installed in the KURAMA magnet. The acceptance of this spectrometer system was 280 msr, which was increased from the E373 experiment by enlarging the pole gap of the KURAMA magnet. In order to cover the acceptance, suitable detectors have been newly constructed.

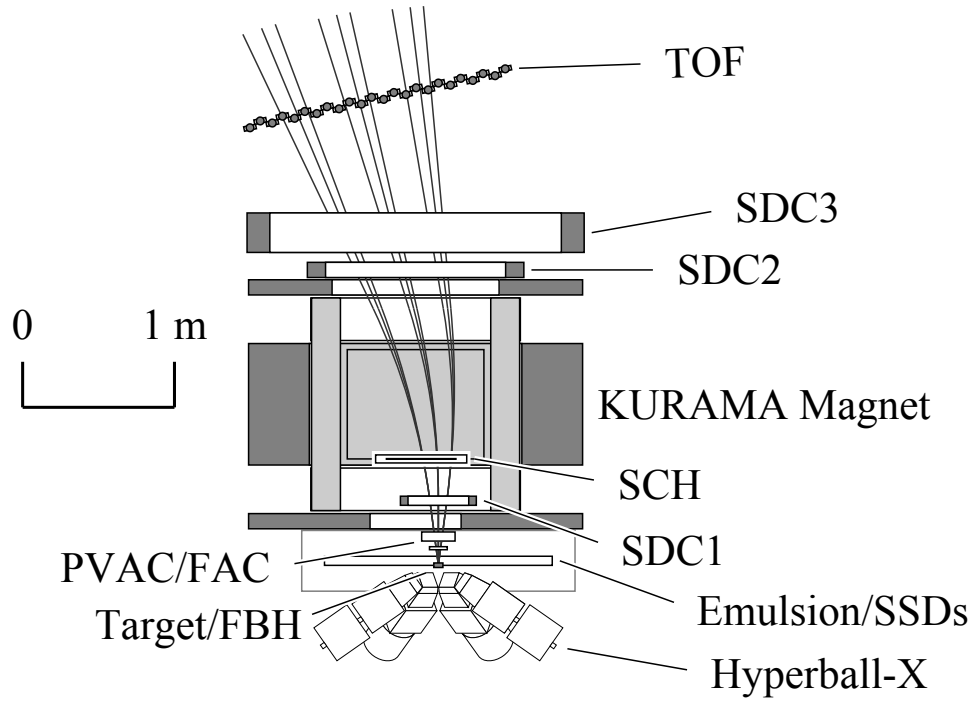

Figure 2.10: Schematic drawings of the KURAMA spectrometer.

BH2

The beam hodoscope 2 (BH2) was installed just after the BC4. It consists of a plastic scintillator (EJ212) with the size of 120 mm(W) × 40 mm(H) × 6 mm(T). Scintillation signals were read by two PMTs (Hamamatsu H10570) on the top and bottom through acrylic light guides. Figure 2.11 shows the schematic drawing. BH2 was used as a start timing counter for our DAQ system.

Table 2.2: The specifications of scintillation detectors for the trigger. Although the FBH had 16 scintillators with 2.5 mm overlap, its signal was treated as 31 segments by considering hit combination.

Detector	Scintillator	Segments	Effective size (one segment) (W) × (H) × (T) [mm]	Readout
BH2	EJ212	1	120 × 40 × 6	PMT (Hamamatsu H10570)
FBH	EJ212	31	82.5 × 35 × 2	MPPC (Hamamatsu S12571-100P)
SCH	EJ212	64	673 × 450 × 2	MPPC (Hamamatsu S10362-11-100P)
TOF	EJ200	24	1805 × 1800 × 30	PMT (Hamamatsu H1945)

Table 2.3: The specifications of Čerenkov counters in the KURAMA spectrometer.

Detector	Refractive index	Effective size of radiators (W) × (H) × (T) [mm]	PMT
BAC	1.03	165 × 75 × 50	Hamamatsu R6683 × 2
PVAC	1.12	120 × 110 × 30	Hamamatsu R6682 × 4
FAC	1.05	210 × 160 × 50	Hamamatsu R6682 × 6

Table 2.4: The specifications of drift chambers in the KURMA spectrometer.

Detector	Plane	Wire pitch [mm]	Effective area (W) × (H) [mm]	Gas
SDC1	UU'XX'VV'	6.0	400 × 250	Ar(76%) + iso-C_4H_{10}(20%) + methylal(4%)
SDC2	XX'YY'	9.0	1187 × 1187	Ar (50%) + ethane (50%)
SDC3	YY'XX'	20.0	1900 × 1280	Ar (50%) + ethane (50%)

BAC · PVAC · FAC

Three kinds of aerogel Čerenkov counters were installed to identify incident and scattered particles in the trigger. These were threshold type Čerenkov counters with a refractive index of 1.03 (BAC), 1.12 (PVAC), and 1.05 (FAC), respectively. BAC was located downstream of BH2 to veto π^- in incident particles. In order to improve the veto efficiency, two sets of BAC were aligned in the beam direction. PVAC (FAC) was located at the entrance of the KURAMA magnet to veto proton (K^- and $\pi^\pm$), respectively. The radiators were installed in a box covered with Teflon sheets to diffuse Čerenkov lights. Fine mesh PMTs were used for these counters near the KURAMA magnet to reduce the effect of fringing field. Figure 2.12,2.13,2.14 show the schematic drawings.

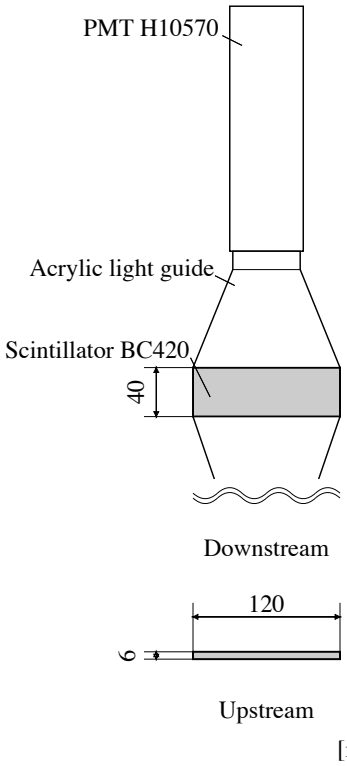

Figure 2.11: Schematic drawings of BH2.

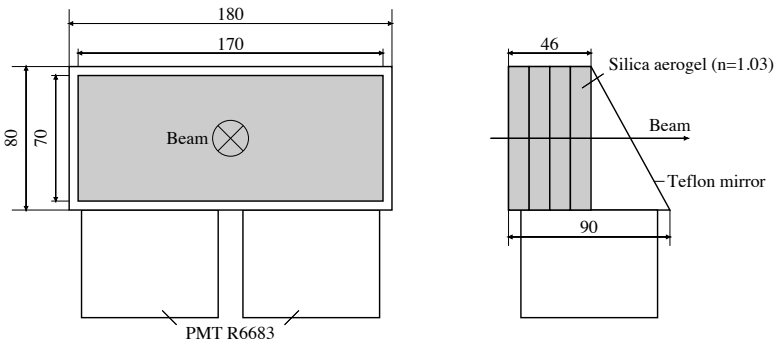

Figure 2.12: Schematic drawings of BAC.

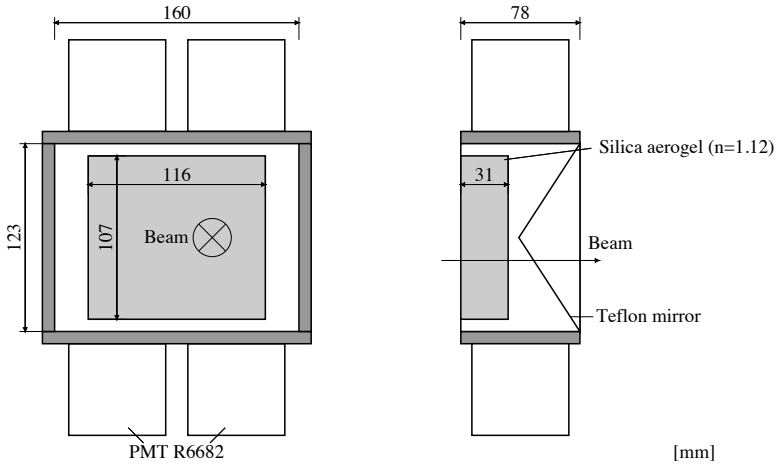

Figure 2.13: Schematic drawings of PVAC.

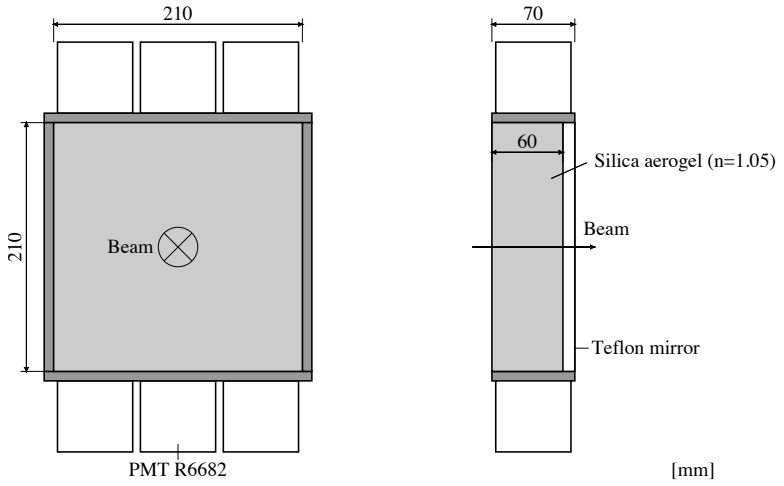

Figure 2.14: Schematic drawings of FAC.

FBH

The fine beam hodoscope (FBH) was located just before the target. FBH · SCH · TOF were used to construct the matrix trigger (Sec.2.7.2). FBH consisted of sixteen segments of plastic scintillators (EJ212) with a size of 7.5 mm(W) × 35 mm(H) × 2 mm(T). Each segment was aligned in two lines with an overlap of 2.5 mm. Then FBH was treated as having 31 segments depending on the hit combination of neighbor segments. Each scintillator has a strip with a width of 1 mm on its surface where 1 mm a wave length shift (WLS) fiber was attached. Scintillation signal was read by two MPPCs (Hamamatsu S12571-100P) attached on both edges of the WLS fiber. MPPC signals were read by EASIROC readout board which is a ASIC to be developed to read multi-MPPC electronics. [40].

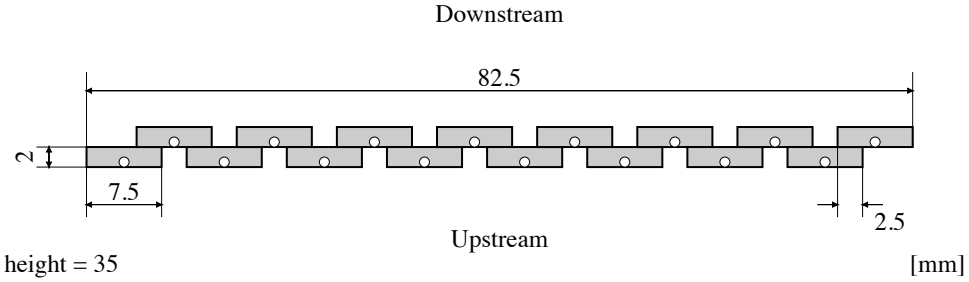

Figure 2.15: Schematic drawings of FBH.

SDC1

A multi-wire drift chamber (SDC1) was located at the entrance of the KURAMA magnet. SDC1 had a six-layers configuration (VV'XX'UU') with a wire pitch of 6 mm. The configuration of field wires was honeycomb-type. The specifications of wires of SDC1 are listed in Table 2.5. The Same gas system was used to SDC1 and BC3,4. A mixed gas of Ar(76%), iso-C_4H_{10}(20%), and methylal(4%) was filled in SDC1. Signals from anode wires were read by ASD cards attached on the chamber. Figure 2.16 shows the schematic drawing of wire configurations in SDC1.

Table 2.5: The specifications of wires of SDC1,2,3.

Chamber	Anode	Potential	Shield
SDC1	20 μm Au-plated W/Re	80 μm Au-plated Al	80 μm Au-plated Al
SDC2	20 μm Au-plated W	100 μm Au-plated Al	100 μm Au-plated Al
SDC3	30 μm Au-plated W	50 μm Au-plated CuBe	50 μm Au-plated CuBe

SCH

A hodoscope (SCH) was located just after SDC1. SCH consisted of 64 segments of scintillators (EJ212) with a size of 11.5 mm(W) × 450 mm(H) × 2 mm(T). Each segment was aligned in two lines with an overlap of 1 mm to reduce the ineffective area. Each

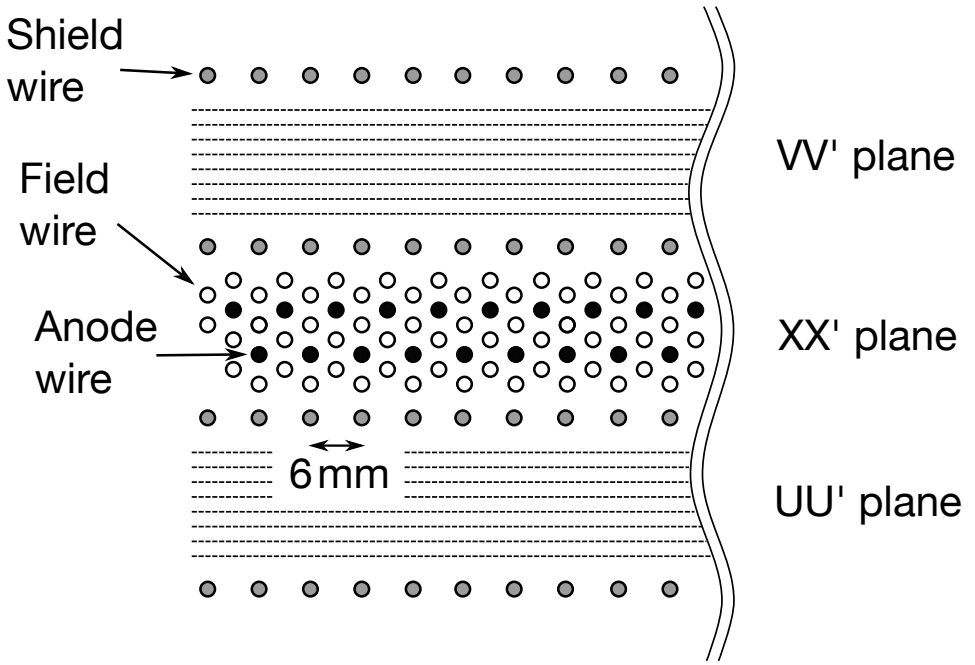

Figure 2.16: Schematic drawing of SDC1.

scintillator had a strip with a width of 1 mm on its surface in which 1 mm wave length shift (WLS) fiber attached. Signal was read by MPPCs (Hamamatsu S10362-11-100P) through WLS fibers. MPPC signals were read by the EASIROC board.

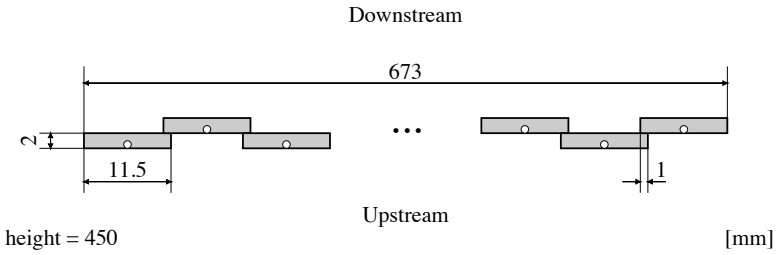

Figure 2.17: Schematic drawings of SCH.

SDC2 and SDC3

Two sets of multi-wire drift chambers (SDC2 and SDC3) were located at the exit of the KURAMA spectrometer. Both chambers had a four plane configuration (XX'YY') with a wire pitch of 9 mm and 20 mm for SDC2 and SDC3, respectively. The specifications of wires of SDC2 and SDC3 are listed in Table 2.5. A mixed gas of Ar(50%) and ethane(50%) was filled in SDC2 and SDC3 and was kept flowing. The configurations of field wires were honeycomb-type. Shield wires were equipped to separate each plane. A signal from each wire was read by pre-amplifier card which was attached on the chambers. It was connected to an amplifier discriminator board and read by Multi-hit TDC (N64). A high voltage of -2.1 kV for potential wires and shield wires was applied to SDC2 in

operation. On the other hand, a high voltage of $-2.8\,\mathrm{kV}$ for potential wires and $-2.9\,\mathrm{kV}$ for shield wires were applied to SDC3 in operation, respectively. Figure 2.18, 2.19 shows the schematic drawing of wire configurations in SDC2 and SDC3.

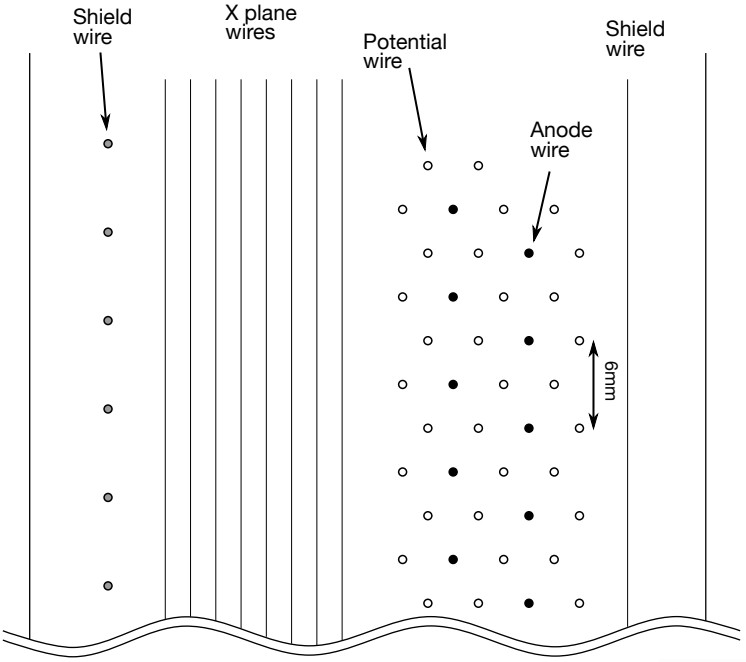

Figure 2.18: Schematic drawings of SDC2.

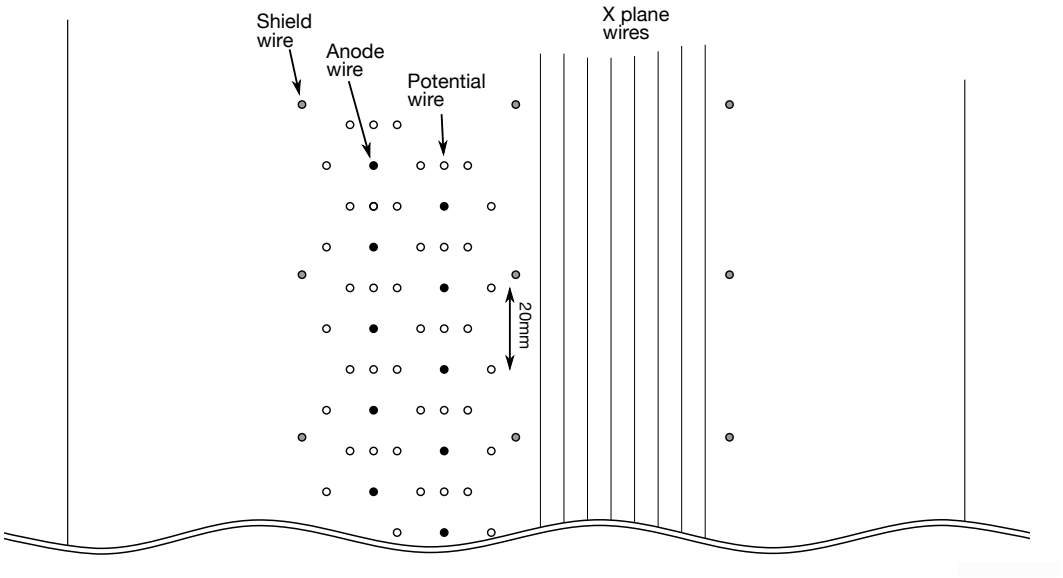

Figure 2.19: Schematic drawings of SDC3.

TOF

The time of flight counter (TOF) was located at the end of KURAMA spectrometer. Flight length of a scattered particle from the targets to TOF was about 3100 mm. TOF consisted of 24 segments of plastic scintillators (EJ200) with a size of 80 mm(W) × 1800 mm(H) × 30 mm(T). The scintillators were aligned in two lines and each segment have an overlap by 5 mm to reduce ineffective area. Scintillation signals were read by two PMTs (Hamamatsu H1945) attached on the top and bottom of the scintillator through light guides. Each PMT was surrounded by a steel tube to prevent from the fringing field. The intrinsic time resolution was estimated to be 80 ps after ADC correction. Figure 2.20 shows the schematic drawing.

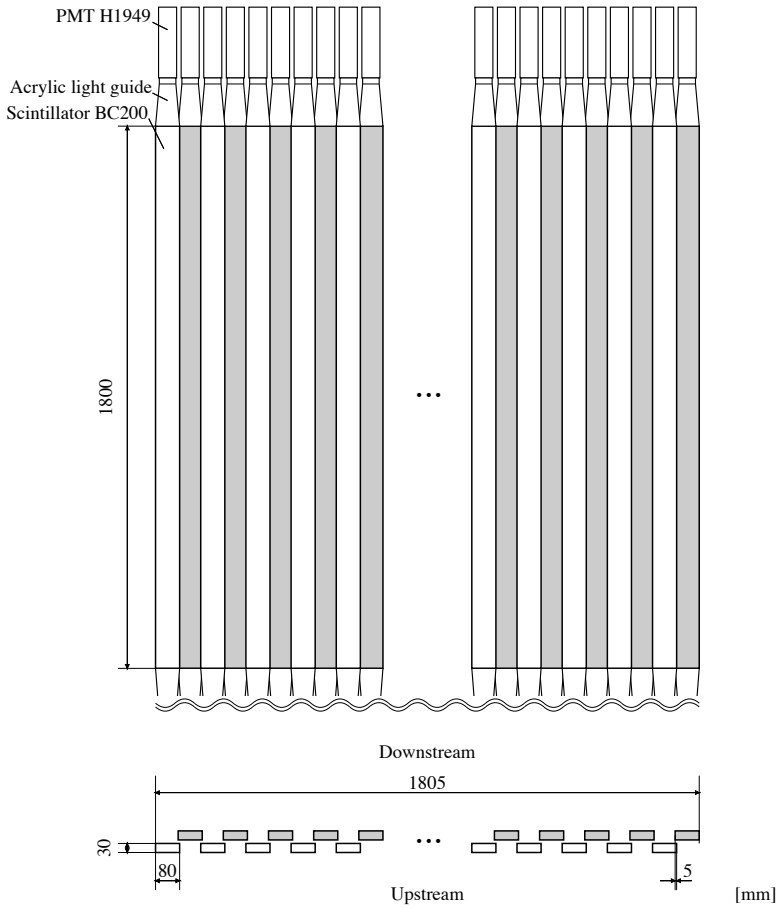

Figure 2.20: Schematic drawings of TOF.

2.4 Diamond target

In the present experiment, the number of Ξ^- stopping event in the emulsion is important. Ξ^- hyperons are generated in the quasi-free $p(K^-, K^+)\Xi^-$ reaction and Ξ^- production cross section is proportional to $A^{0.38}$ of the target material [41]. Since the proton ratio becomes smaller by increasing the mass number, small mass material is better to optimize the rate of $p(K^-, K^+)\Xi^-$ reaction. On the other hand, high density material was

preferred to accumulate stop events because the loss of the kinetic energy becomes large. From the above considerations, the diamond was adopted for the reaction target. Since the diamond is a stable material, it was easy to handle.

The size of the diamond target was 50 mm (W) × 30 mm (H) × 30 mm (T). The diamond target was composed of 45 pieces of 10 mm cubes. One cube consisted of 10 thin wafers and those were tightly fixed with epoxy [42]. The density was measured to be $3.243 \pm 0.016\,\mathrm{g/cm^3}$, which corresponds to 92% of that of the pure diamond crystal ($3.51\,\mathrm{g/cm^3}$).

2.5 Emulsion

Each emulsion module consisted of eleven thick-type sheets sandwiched between two thin-type sheets with an area of 345 mm [W] × 350 mm [H] (Fig. 2.21). The thin-type sheets had emulsion layers with a thickness of 100 μm on both sides of 180 μm polystyrene base film and were used to connect tracks to the SSDs, because they have high deformation tolerance thus good angular resolution. The thick-type sheets had 450 μm thick layers on both sides of 40 μm polystyrene base film. The emulsion layers were made of "Fuji GIF" emulsion gel produced by FUJIFILM Corporation. The typical density of the emulsion gel was $3.53\,\mathrm{g/cm^3}$. The composition of the emulsion gel is listed in Table 2.6, which was estimated from the production process.

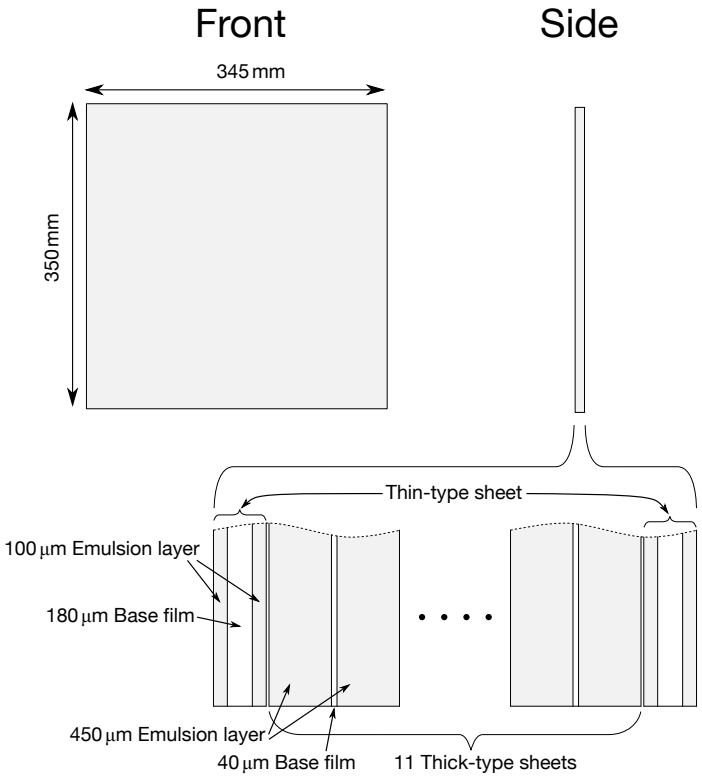

Figure 2.21: Schematic view of a emulsion module.

Emulsion sheets were packed in a stainless steel case named "emulsion cassette". Figure 2.22 shows the schematic drawing of the cassette. The upstream surface of the

Table 2.6: The composition of the Fuji GIF emulsion.

material	weight ratio [%]
H	1.42
C	9.27
N	3.13
O	6.54
Ag	45.52
Br	33.17
I	0.94

cassette was a 0.1-mm SUS plate. The downstream side was sealed with a 1-mm thick rubber sheet. The thirteen emulsion sheets were packed all together in the cassette and fixed tightly by vacuum pumping. Inner gas of the cassette was drawn from a non-return valve before the beam exposure. Then the inside of the cassette could be kept vacuum during the beam exposure without additional pumping.

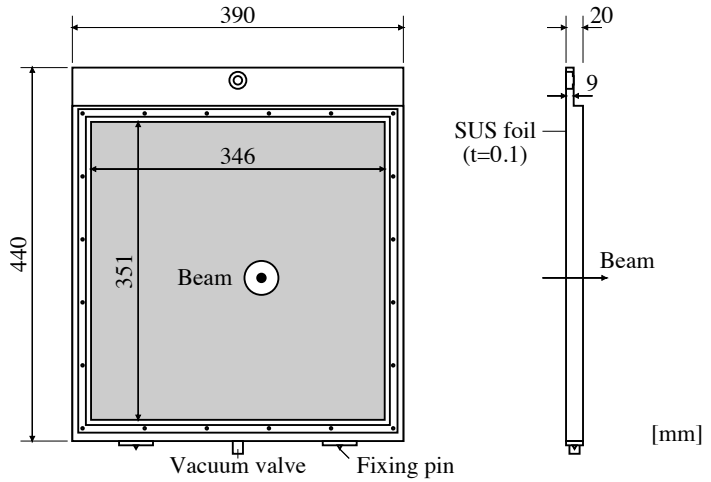

Figure 2.22: Schematic view of the emulsion cassette.

The cassette was mounted on an Emulsion Mover (EM). EM move the cassette in the beam spill-off period to keep the beam particles density less than 1×10^4 particles/mm^2 in order to keep good efficiency for automated image tracking. The cassette was moved along the horizontal and vertical rails with stepping motors. The stepping size was tuned depending on the beam intensity. Figure 2.24 shows the typical distributions of beam center position on a emulsion module. Four corner were avoided to expose for $\overline{p}$ beam through calibration. The position of the cassette was recorded with a few μm accuracy with two linear encoders attached on each rail. Figure 2.23 shows the schematic drawing of the EM.

The thickness and weight of each emulsion sheet were measured just after beam exposure to estimate the density and the shrinkage effect of the sheet. Emulsion sheets were kept in a humidity of 60% and a temperature of 25°C condition in the Kamioka mine until photographic development to keep the ratio of moisture in the emulsion layer

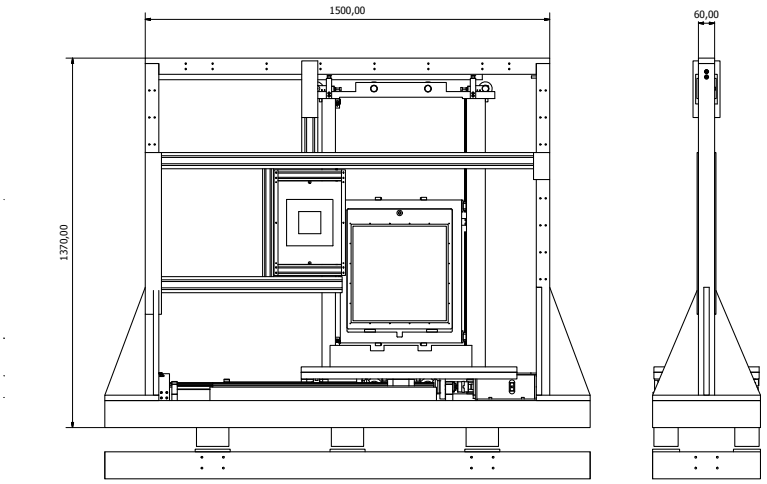

Figure 2.23: Schematic drawings of Emulsion Mover.

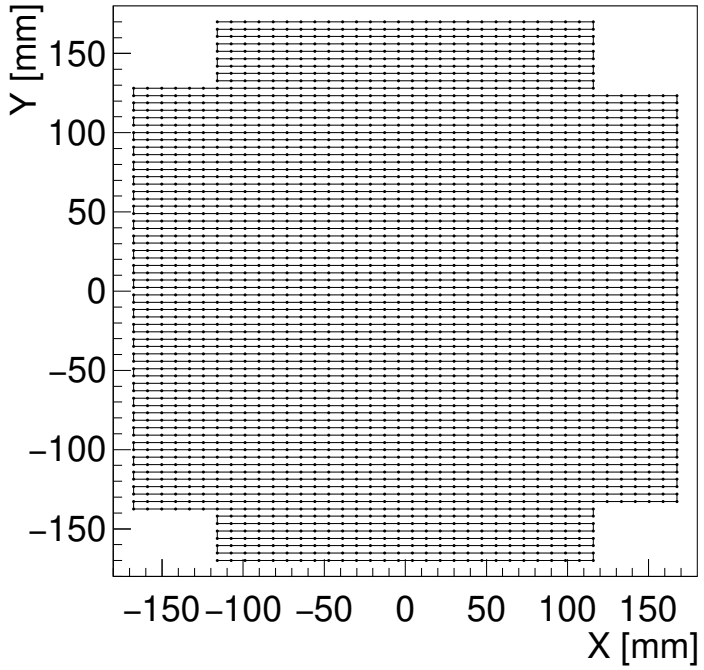

Figure 2.24: The typical distributions of beam center position on a emulsion module. The close circles shows the beam position and solid line shows the movement.

and to prevent radiation damage from the cosmic ray and the gamma ray came from natural isotopes.

2.6 SSD

In order to find Ξ^- tracks in emulsion by the prediction with a tracking detector, the prediction accuracy should be less than several dozen μm. Additionally, a thin detector was preferred because the life time of the Ξ^- hyperon is short (1.6×10^{-10} s). Therefore, Silicon Strip Detector (SSD) was adopted to detect Ξ^- tracks in the present experiment. Two SSDs were located to sandwich the emulsion cassette in the beam direction. The downstream SSD was used to reject Ξ^- hyperons which penetrated the module without nuclear interactions. Each SSD have four layers configuration (XYXY) with a strip pitch of 50 μm. The size of a silicon sensor was 77 mm (H) $\times$ 77 mm (W) $\times$ 0.3 mm (T). Resolutions of position and angle were 15 μm and 20 mrad, respectively. The analog signal of each strip was read by APV25 chip which was attached near the sensor and delivered to the APVDAQ VME module. The signal was converted to a digital signal by pulse shape sampling with 25 ns interval.

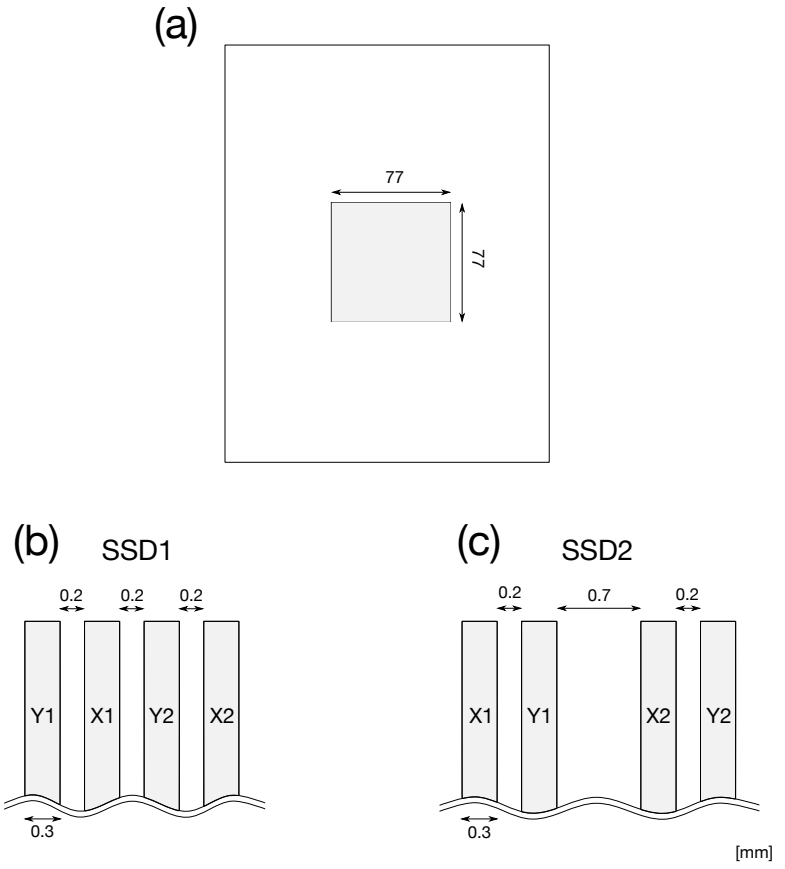

Figure 2.25: Schematic drawings of SSD. Gap of silicon sensors were different between SSD1 (b) and SSD2 (c).

2.7 Trigger

In order to accumulate data of the (K^-, K^+) events, incoming K^- and outgoing K^+ are chosen by a trigger system. Since the cross section of $p(K^-, K^+)\Xi^-$ reaction is smaller than many other reactions, *e.g.,* (K^-, π^+), (K^-, p), etc., the trigger condition is very important to obtain good efficiency of data acquisition. Identification of a particle was mainly done by aerogel Čerenkov counters. The threshold of each aerogel Čerenkov counters is shown in Fig. 2.26. Since KURAMA spectrometer has large angular acceptance, both of positive and negative charged particles passed through the spectrometer. A matrix trigger was used to select the appropriate momentum region of positive kaons. The detail of the trigger condition is as follows.

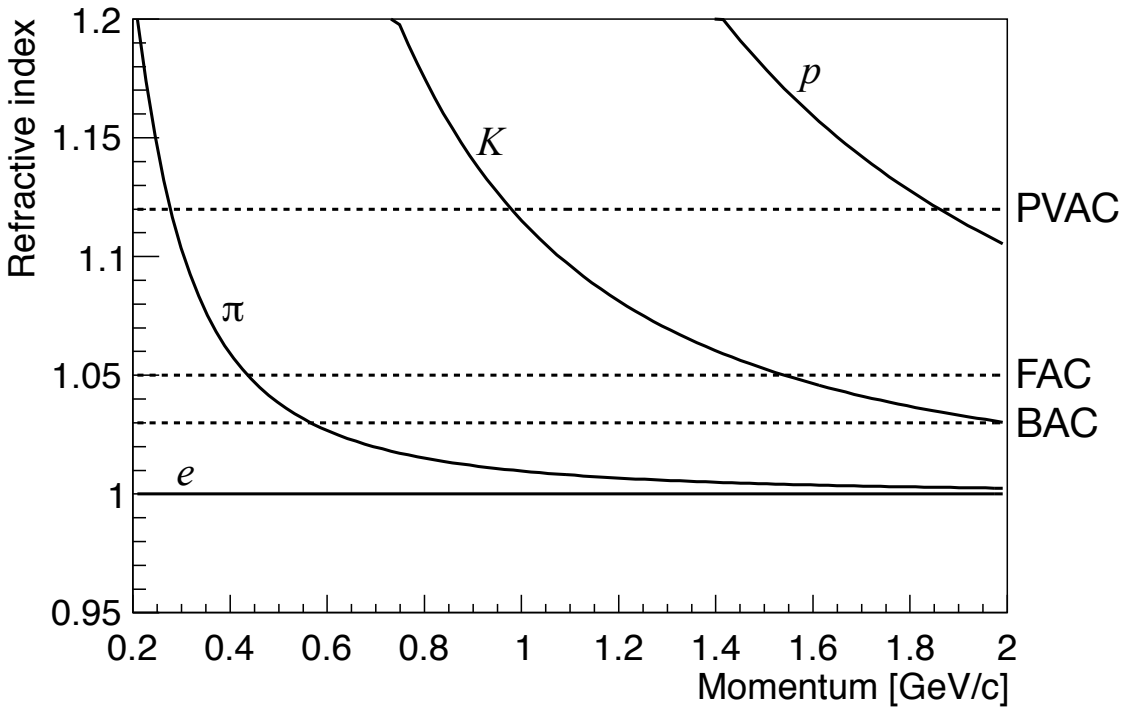

Figure 2.26: Thresholds of emission of a Čerenkov light for each particle as a function of particle momentum. The dotted lines indicate the refractive index of the radiator of each aerogel Čerenkov detectors.

2.7.1 Beam K^-

The trigger to collect K^- beam was defined as the following logic.

$$K_{in} = BH1 \times BH2 \times \overline{BAC1} \times \overline{BAC2}. \tag{2.1}$$

The coincidence of two timing counters (BH1 and BH2) was used to select particles which passed through the K1.8 beam line spectrometer. Since BH1 and BH2 have two PMT's on the top and bottom of a scintillator, a mean timer module was used to cancel the time difference depending on the hit position. The purity of K^- in the beam particle was about 82% in the present experiment owing to the double mass separation system in the K1.8 beam line. The main background was π^- and other light particles and the contamination of $\overline{p}$ was negligible. Figure 2.27 shows the distribution of time-of-flight between BH1 and BH2 with an unbiased trigger condition. The thresholds of emission of a Čerenkov light for π^- and K^- for BAC (index: 1.03) are 0.5 GeV/c and 2.0 GeV/c, respectively. The π^- background can be rejected by requiring BAC hits.

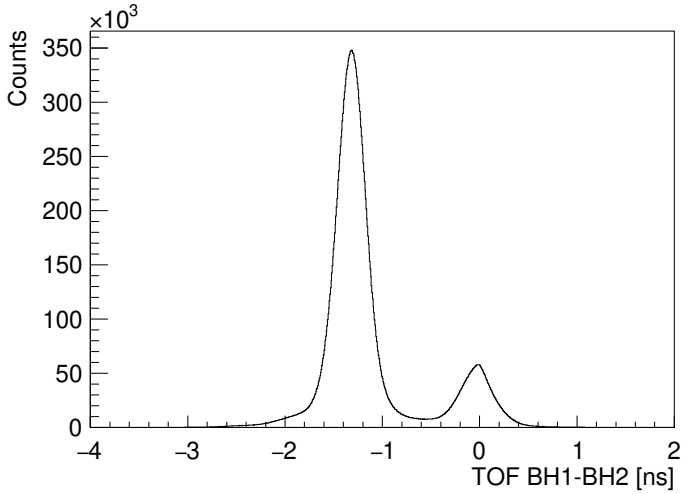

Figure 2.27: Time of flight of incident particles between BH1 and BH2. The origin is adjusted to π^-.

2.7.2 Scattered K^+

The trigger to collect scattered K^+ was defined as the following logic.

$$K_{out} = BH2 \times TOF \times PVAC \times \overline{FAC} \times 2D\text{-}Mtx \times \overline{3D\text{-}Mtx}. \tag{2.2}$$

The coincidence of two timing counters (BH2 and TOF) was used to select particles which passed through the KURAMA spectrometer. A mean timer module was also used for TOF. In the K^- induced reaction, protons which come from decays of hyperons make a large background. These protons mainly have low momentum. On the other hand, the momentum of a K^+ meson come from the $p(K^-, K^+)\Xi^-$ reaction with 1.8 GeV/c K^- ranges 1.0–1.4 GeV/c. The thresholds of emission of a Čerenkov light for a proton and

K^+ for PVAC (index: 1.12) are 2.0 GeV/c and 1.0 GeV/c, respectively. By requiring PVAC hits, proton background can be suppressed. FAC (index: 1.05) was used to reject K^- beam and pions which came from (K, π) reactions.

Matrix trigger

The matrix trigger was constructed by hit combinations of three counters, FBH, SCH, and TOF. When a charged particle passed through the KURAMA magnet field, its trajectory was strongly correlated with its momentum. Therefore, momentum and charge polarity could be selected with the hit combinations of those detectors. We prepare two types of matrix triggers, two dimensional matrix (2D-Mtx) and three dimensional matrix (3D-Mtx). The 2D-Mtx consisted of SCH and TOF, which are used to select 0.9-1.4 GeV/c K^+. Figure 2.28 shows the hit combination of SCH and TOF by selecting the K^+. When an event had hit combination inside of the red line, 2D-Mtx trigger signal was generated. The 3D-Mtx consisted of FBH, SCH, and TOF, which are used to veto K^- beam because FAC was not enough to reject it. Figure 2.29 shows the hit combination of SCH and TOF for K^- beam with a hit of FBH seg#16. When an event had hit combination inside of the red line, 3D-Mtx trigger signal was generated. Since FBH had 31 segments, the cut condition was tuned for each FBH hit segment.

The matrix trigger was produced by an FPGA module called Hadron Universal Logic (HUL) module. Digitized signals of FBH, SCH, and TOF were inputted to the HUL. The clustering of FBH signals to produce 31 segments from hit combination was also done by the FPGA in the HUL.

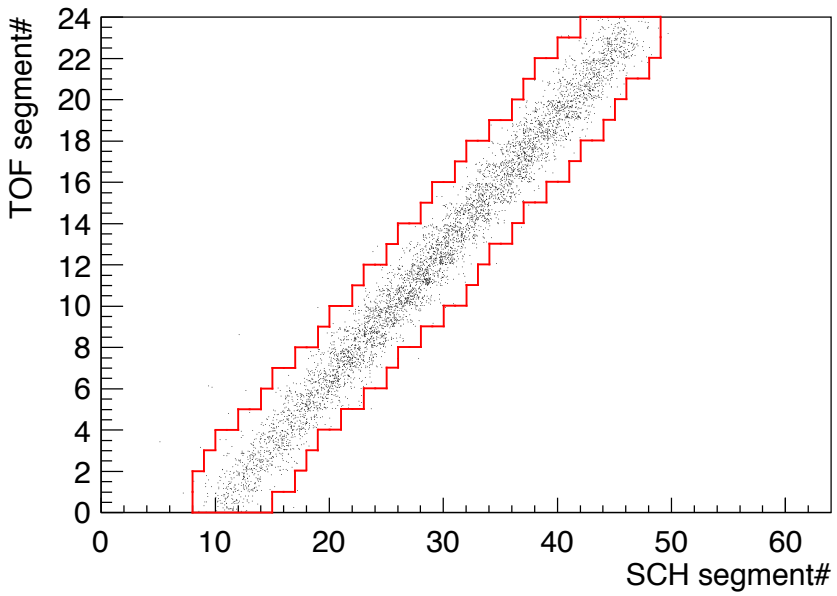

Figure 2.28: The hit combination between SCH and TOF for K^+ with a momentum of 0.9-1.4 GeV/c. The red area shows the accepted region for the 2D-Mtx.

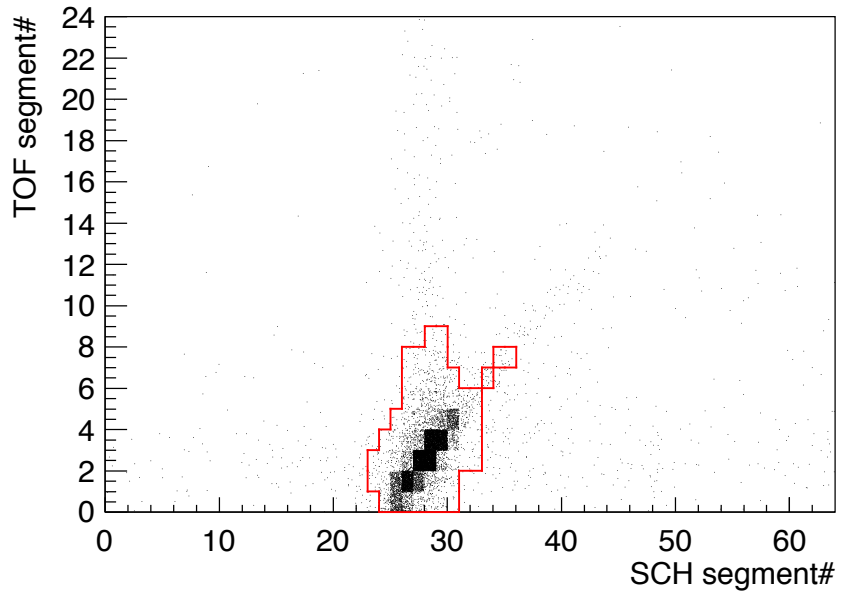

Figure 2.29: The hit combination between SCH and TOF for beam K^- with FBH#16 hit (center). The red area shows the accepted region for the 3D-Mtx.

2.7.3 Triggers for the data taking

The main trigger for the (K^-, K^+) reaction was defined the as following.

$$(K, K) = K_{in} \times K_{out}. \tag{2.3}$$

The typical trigger rate was 2000/spill with the K^- intensity of 2.8×10^5 /spill. In order to monitor the beam condition and the performance of detectors, an unbiased trigger to collect the events in which beam passed through both of the K1.8 beam line spectrometer and the KURAMA spectrometer was also constructed.

$$(Beam \times TOF) = BH1 \times BH2 \times TOF. \tag{2.4}$$

This trigger was mixed to the main trigger by being scaled with pre-scaler modules to keep the DAQ efficiency. These trigger signals were recorded by a TDC module to select the trigger condition in the analysis.

2.8 DAQ

A network controlled system was adopted to the data acquisition (DAQ) system of K1.8 beam line. Figure 2.30 shows a diagram of the DAQ system in the K1.8 beam line. Data from each detector was read out through each sub system. The trigger counters signals were recorded with ADC and TDC modules which were controlled by VME-CPU module (XVB601). Signals of BC3,4 and SDC1 were read by the COmmon Pipelined Platform for Electronics Readout (COPPER) module [43]. Signals of SDC2 and SDC3 were read

by the multi-hit TDC modules which were controlled by XVB601. Signals of SSD were recorded read by APVDAQ modules which were also controlled by XVB601. Signals of MPPC detectors were read by EASIROC module. In order to record count rate for each detector, HUL modules were used.

Digitized signals from each sub system were collected to the host computer. A part of data were decoded to check the performance of detectors in online analysis.

Signals from sub systems were read in event by event. Those systems were asynchronous. Trigger and spill information were send to each sub system from the master trigger module (MTM) to confirm event identity.

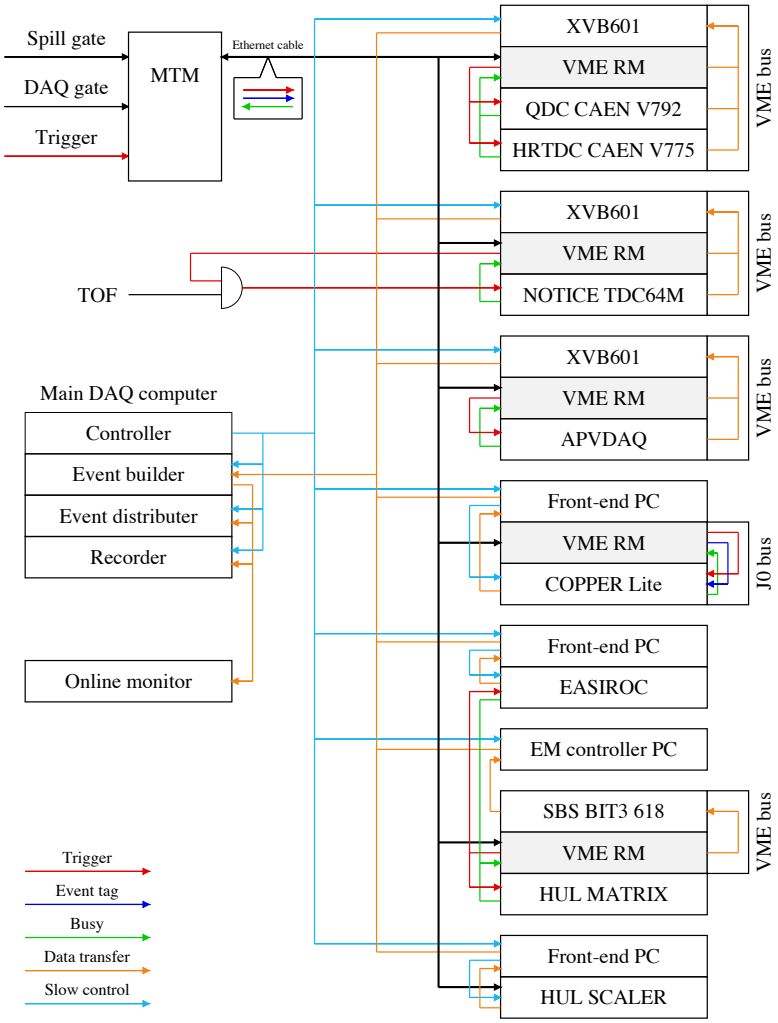

Figure 2.30: The schematic drawing of the DAQ flow.

2.9 Data summary

Beam exposure of the E07 was carried out in 2016 and 2017. A total of 118 modules produced from 2.1 tons emulsion gel were exposed to 1.13×10^{11} particles of the K^- beam. Beam condition was changed due to the accelerator condition in each period. Typical

beam conditions are listed in Table 2.7. In order to calibrate the relative position between the SSDs and each emulsion module, $\overline{p}$ beam through data was taken just before the K^- beam exposure at four corners of emulsion modules (See Sec. 4.3.2). The typical size and amount of $\overline{p}$ beam on a corner were 10 mm(σ) and 2.3×10^4 particles, respectively, with a beam rate of 700/spill. The typical DAQ efficiency was 94% in this condition. The unbiased trigger condition was adopted to these data taking. Photographic development of emulsion sheets was performed just after emulsion exposure. It takes two weeks for one sheet to finish all processes. All sheets were developed in Feb. 2018.

Table 2.7: Data summary for emulsion exposure

Year	Modules	Beam power [kW]	K^- intensity [$\times 10^3$/spill]	K^- purity [%]	Time [h/mod.]	Integrated K^- [$\times 10^9$/mod.]	DAQ Eff. [%]
2016	18	42	260	81	6.5	0.92	83
2017	8	44	310	83	5.6	1.0	84
2017	14	10–33	120–270	50–82	6.5–9.0	0.52–1.0	89–92
2017	78	37.5	280	82	6.0	1.0	89

In order to calibrate the spectrometers system, we took fundamental data by changing the experimental setup and beam conditions. The polyethylene target data was taken to check the elementary $p(K^-, K^+)\Xi^-$ reaction. The diamond target was exchanged to a polyethylene target with a size of 50 mm × 30 mm × 30 mm ($2.88\,g/cm^3$), which was the same size as the diamond target. The emulsion module was not installed at that time. The condition of beam and trigger was almost the same as that of the emulsion exposure. We also took the beam through data to calibrate detector positions and evaluate the momentum analysis of the KURAMA spectrometer by changing the beam condition. No magnetic field data was also taken by turning off the KURAMA magnet. The conditions of the beam through data is listed in Table 2.8. The typical beam intensity was 10^4/spill. The target and the emulsion module were uninstalled.

Table 2.8: Conditions of the beam through data.

Beam particle	Momentum [GeV/c]	KURAMA current [A]
K^-	1.8	0
K^-	1.8	2400
K^+	1.4	2400
K^+	1.2	2400
K^+	1.0	2400
π^+	1.4	2400
π^+	1.2	2400
π^+	1.0	2400

Chapter 3

Analysis I - Spectrometer

3.1 Outline

Double-Λ hypernuclei were searched by tracing Ξ^- tracks which were detected with the SSD. Therefore, the identification of Ξ^- tracks with the SSD is essential for the counter-emulsion hybrid method. In order to identify the $p(K^-, K^+)\Xi^-$ reaction, incoming K^- and outgoing K^+ were analyzed by two spectrometer systems. Then, Ξ^- tracks were searched from SSD hits according to the $p(K^-, K^+)\Xi^-$ kinematics. A Monte Carlo simulation was performed to optimize the criteria to select Ξ^- tracks. Several criteria were adopted to optimize the ratio of Ξ^- stopping event to the reconstructed Ξ^- tracks by keeping its efficiency. From the predictions with the SSD, the Ξ^- tracks were searched in emulsion sheets with micro scope systems.

In this chapter, the procedure to identify Ξ^- tracks for the emulsion analysis is explained.

3.2 K^- analysis

3.2.1 K^- identification

Incoming K^- was identified with the time-of-flight (TOF) timing between BH1 and BH2 (11 m). Figure 3.1 shows the time-of-flight distribution for incident particles accumulated by the production trigger. The contamination of π^- was negligible because they were rejected by BACs. The origin of TOF was adjusted to π^- for each BH1 segment. The typical TOF resolution was 150 ps after correction by ADC. The cut condition which is from -2.8 ns to 0.2 ns was applied to select K^+ with a large surviving ratio. 99.2% of total events was survived. This cut condition is shown as the arrows in Fig. 3.1.

3.2.2 K^- momentum analysis

The momentum of incoming K^- was analyzed by the beam line spectrometer with the 3rd-order transfer matrix method by measuring the position at the entrance of the spectrometer and the trajectory at the exit of it with corresponding detectors.

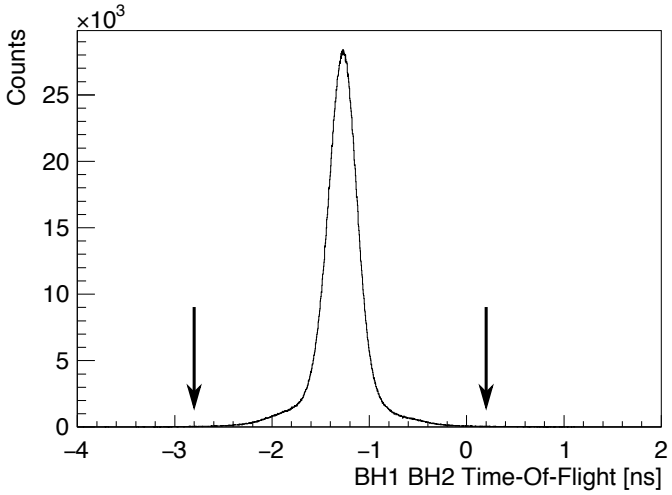

Figure 3.1: Distribution of Time-Of-Flight between BH1 and BH2.

Local tracking of BC3 and BC4

BC3 and BC4 are multi wired drift chambers equipped at the exit of the beam line spectrometer. Both chambers had six layers configuration (XX'UU'VV') with a wire pitch of 3 mm. Straight line fitting was performed to minimize the reduced chi-square as follows.

$$\begin{aligned}
\chi^2/ndf &= \frac{1}{n-4}\sum_{i=1}^{n} w_i(X_i - f(z_i))^2, \qquad (3.1)\\
X_i &= wp_i \pm dl_i(t_i),\\
f(z_i) &= x(z_i)\cos(\alpha_i) + y(z_i)\sin(\alpha_i),\\
x(z_i) &= x_0 + u_0 z_i,\\
y(z_i) &= y_0 + v_0 z_i.\\
w_i &= \frac{1}{\sigma_i^2}.
\end{aligned}$$

where, x_0, y_0, u_0, and v_0 are the parameters to indicate the position and angle of the track. The parameter n denote the number of hit planes in BC3 and BC4 and the tilt angle and Z position of i-th hit plane is shown as α_i and z_i, respectively. The hit position in each detector, X_i, was obtained by the position of hit wire (wp) and drift length (dl) which was calculated from the drift time (t) and the drift function. The weight factor w_i is corresponding to the intrinsic resolution, σ_i, of each plane. When a plane had multiple hit wires, all hit combinations were calculated to extract the most probable track by sorting them according to the χ^2/ndf. The typical reduced chi-square distribution is shown in Fig. 3.2. The threshold of 20 was set to select good events which is shown as an arrow.

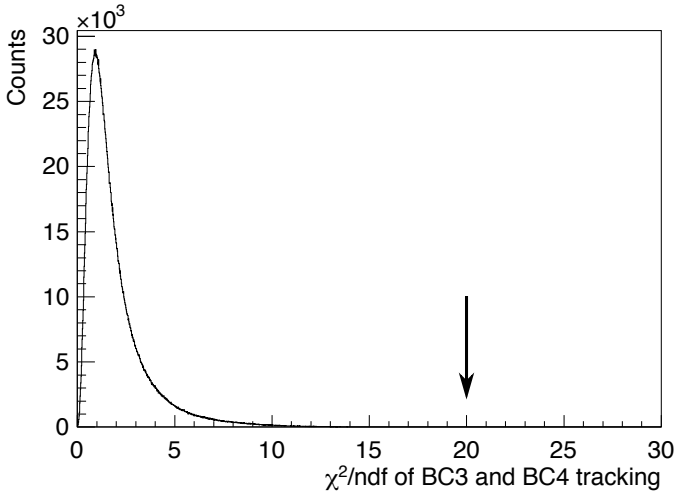

Figure 3.2: Distribution of reduced chi-square of BC3 and BC4 tracking.

K18 tracking

The transfer matrix of the K1.8 beam line was calculated by ORBIT [38] from the current setting of QQDQQ magnets. In order to perform the 3rd-order transfer matrix method, the following parameters were used: the X positions at the entrance and the trajectory, i.e. position and angle, at the exit. From the inverse transfer matrix and the particle trajectory of the final state, the momentum of the particle can be expressed by the X position of the initial state. Then, the momentum was calculated by general solution of a cubic equation. This analysis is named as K18 tracking. The position of incoming K^- was measured by BFT. Since BFT had two layers configuration(XX') with an overlap, neighbor signals were clustered. The typical distribution of reconstructed momentum of K^- beam is shown in Fig. 3.3. The designed value of momentum resolution is 3.3×10^{-4}(FWHM). The present momentum distribution is consistent with the expected momentum bite with the resolution.

3.3 K^+ analysis

3.3.1 Momentum analysis of outgoing particles

Local tracking of SSDs, SDC1, and SCH

The local straight tracking was performed with SSD1, SSD2, SDC1, and SCH. When the particle did not pass through the SSDs perpendicularly, several strips had hits and its charge deposit in a layer was shared depending on the distance between a strip and the particle position. Thus, the neighbor signals in an SSD layer were clustered and a hit position of each cluster was defined to be the centroid of the charge. Since SDC1 had honeycomb configuration, electric field around an anode wire had a circular shape. Then, a constructed track was assumed by iteration. In order to analyze this tracking in the same frame work as the local tracking of BC3 and BC4, a hit position of SDC1 were

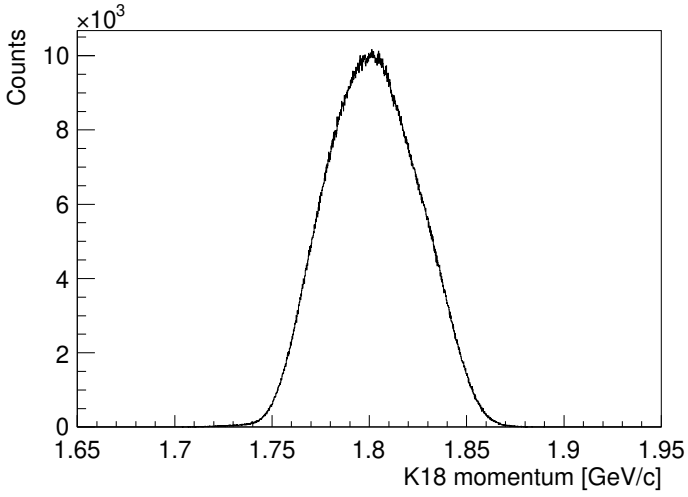

Figure 3.3: Distribution of K^- beam momentum obtained by K18 tracking.

tuned from the result of the last iteration as shown in Fig. 3.4. The reduced chi-square of a honeycomb chamber in l-th iteration is described as follows:

$$
\begin{aligned}
(\chi^2/ndf)^l &= \frac{1}{n-4}\sum_{i=1}^{n} w_i^l (X_i^l - f^l(z_i^l))^2, \qquad (3.2)\\
f^l(z_i) &= (x_0^l + u_0^l z_i^l)\cos\alpha_i + (y_0^l + v_0^l z_i^l)\sin\alpha_i,\\
\frac{df_i^l}{dz_i^l} &= u_0^l \cos\alpha_i + v_0^l \sin\alpha_i\\
\cos\theta_i^l &= \frac{1}{\sqrt{1+(\frac{df_i^l}{dz_i^l})^2}},\\
\sin\theta_i^l &= \frac{\frac{df_i^l}{dz_i^l}}{\sqrt{1+(\frac{df_i^l}{dz_i^l})^2}},\\
X_i^l &= \begin{cases} wp_i + dl_i\cos\theta_i^{l-1} & (f_i^{l-1} > wp_i),\\ wp_i - dl_i\cos\theta_i^{l-1} & (f_i^{l-1} < wp_i), \end{cases}\\
z_i^l &= \begin{cases} wz_i - dl_i\sin\theta_i^{l-1} & (f_i^{l-1} > wp_i),\\ wz_i + dl_i\sin\theta_i^{l-1} & (f_i^{l-1} < wp_i), \end{cases}\\
w_i^l &= \frac{1}{\sigma_i^2}\cos\theta_i^{l-1},
\end{aligned}
$$

where, the parameters θ and wz indicate the track angle and the z position of a hit wire, respectively. In the first iteration, the θ was treated as 0. Iteration was carried out several times until the reduced chi-square value converge *i.e.* the difference from the last iteration become less than 0.005. The typical distribution of the reduced chi-square is shown in Fig. 3.5 with the arrow which shows the threshold of 40 to select good tacking events.

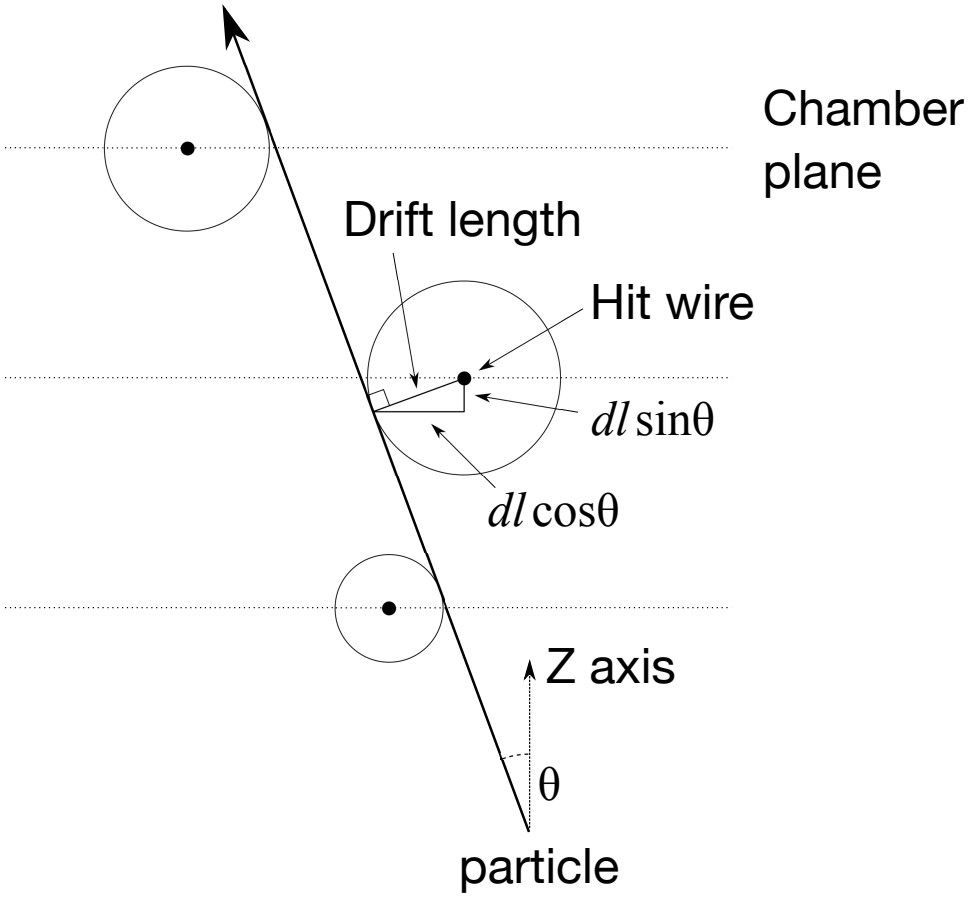

Figure 3.4: The schematic drawing of the concept of the analysis of honeycomb chambers.

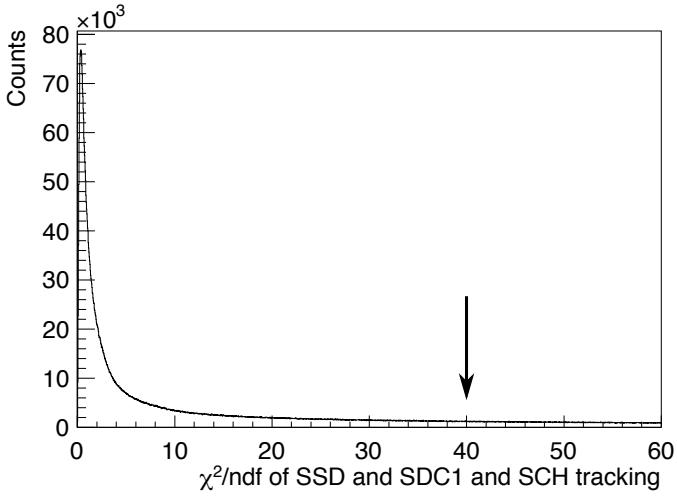

Figure 3.5: Distribution of reduced chi-square of SSD and SDC1 and SCH tracking.

Local tracking of SDC2 and SDC3

The local straight tracking was performed with SDC2 and SDC3. Since both of SDC2 and SDC3 had honeycomb-type wire configuration, the tracking was performed according to minimize the chi-square expressed as Eq. 3.2. The typical reduced chi-square distribution is shown in Fig. 3.6. The threshold of 30 to select good tracking events is shown as the arrow. Since SDC2 and SDC3 have XY configuration, there were ghost tracks, which did not exist but were constructed by wrong XY combination for multi tracks. These tracks were excluded by examining the difference between TOF hit and predicted position. The relation between X position of SDC2 and SDC3 tracking and TOF segment is shown in Fig. 3.7. Since TOF have two PMT's on the top and bottom, Y position can be deduced from the difference of time between them. The relation between Y position of SDC2 and SDC3 tracking and the time difference between the two PMTs of TOF is shown in Fig. 3.8. The right figures of Fig. 3.7 and Fig. 3.8 are the projected residual expressed as

$$R_x = X - 73 \times Seg + 665,$$
$$R_y = Y - 77 \times dT + 18,$$

respectively. X and Y represent the track positions on the TOF surface. The parameters Seg and dT show the hit segment and the difference between TDCs of the tow PMTs on TOF, respectively. The cut condition is defined as $-170 < R_x < 170$ and $-220 < R_y < 220$ those are shown as the arrows in Fig. 3.7 and Fig. 3.8.

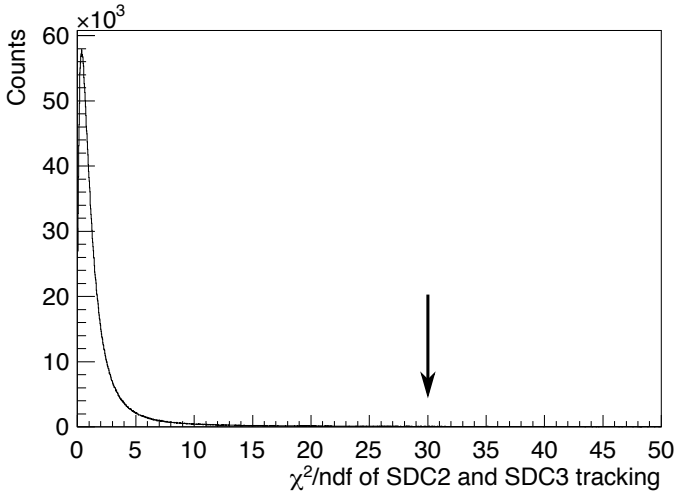

Figure 3.6: Distribution of reduced chi-square of SDC2 and SDC3 tracking.

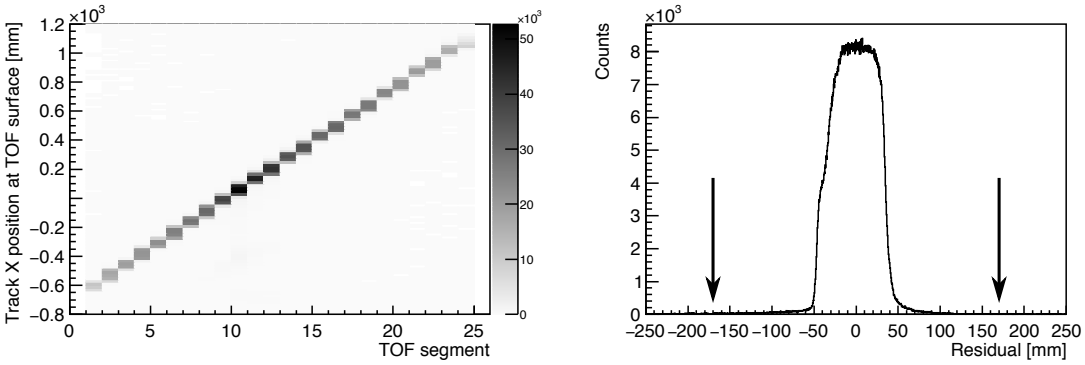

Figure 3.7: Correlation between TOF segment and X position of SDC2 and SDC3 tracking.

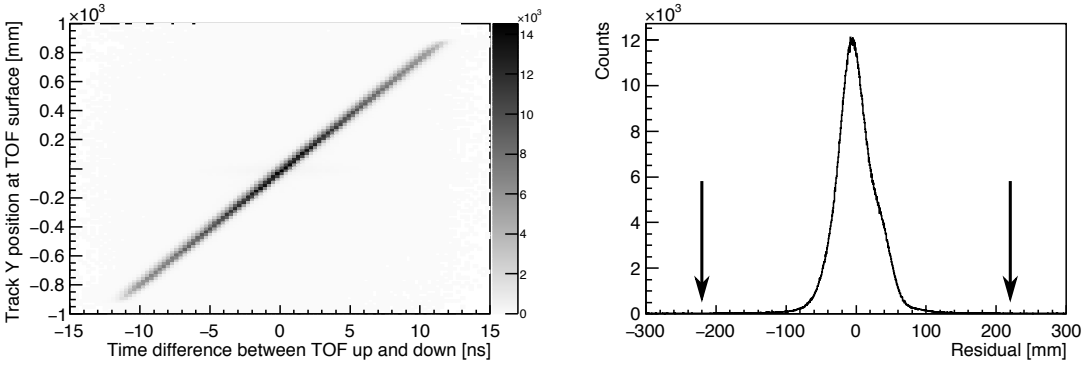

Figure 3.8: Correlation between the time difference between TOF top and bottom and Y position of SDC2 and SDC3 tracking.

KURAMA tracking

In order to analyze the momentum of the scattered particle, its trajectory in the KURAMA magnet field was reconstructed with the Runge-Kutta method [39] by combining the results of tracking of the entrance and the exit of the KURAMA spectrometer. This procedure was called as KURAMA tracking. Five parameters, momentum, positions (x, y) and angles (dx/dz, dy/dz) at TOF position, were used to the fitting. The magnetic field was calculated with ANSYS code [44]. The optimal momentum and trajectory of the outgoing particle were obtained by the iteration to reduce the following reduced chi-square

$$\chi^2_{KURAMA} = \frac{1}{n-5}\sum_{i=1}^{n}\left(\frac{X_i^{hit} - X_i^{track}}{\sigma_i}\right)^2, \tag{3.3}$$

where n is the number of hit layers in the KURAMA tracking. X_i^{hit} and X_i^{track} represent the hit position of the particle and the predicted position of the reconstructed track. The parameter σ_i shows the resolution of each detector. The convergence of the iteration was judged by the difference from the last calculation as the following criterion, $(\chi^2_{k+1} - \chi^2_k)/\chi^2_k < 10^{-3}$, where χ^2_k represents the result of the k-th iteration. The typical reduced chi-square distribution of the KURAMA tracking is shown in Fig. 3.9. Since the distribution have a large tail, the threshold of 10 was adopted to select good tracks. This cut window is indicated by an arrow. The momentum resolution of the KURAMA spectrometer was estimated by comparing to the K1.8 beam line spectrometer because its resolution is much better than that of the KURAMA spectrometer (See Sec 3.4).

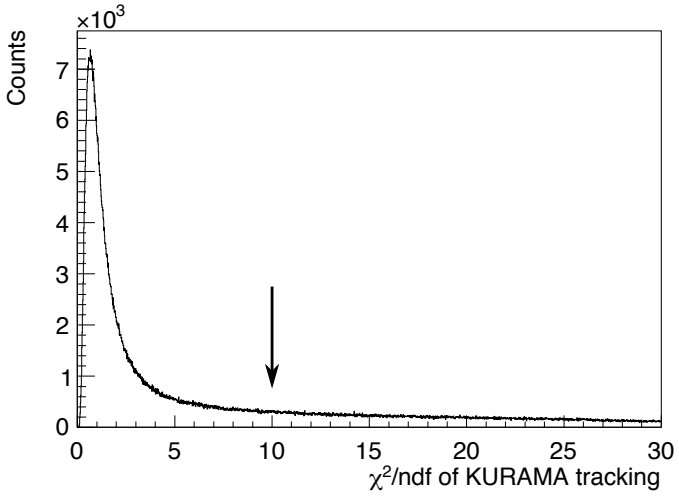

Figure 3.9: Distribution of reduced chi-square of KURAMA tracking.

3.3.2 K^+ identification

Scattered K^+ was identified by reconstructed mass and momentum. The mass of a scattered particle was reconstructed by the analyzed momentum and time-of-flight between the BH2 and TOF. The typical TOF resolution is 140 ps. The time offset for each TOF

segment was tuned to reproduce the PDG mass of K^+ ($493.677\,\mathrm{GeV}/c^2$). In order to select particles which came from a nuclear reaction in the target, vertex distribution obtained by the K18 and KURAMA tracking was examined. Scattered events were chosen as shown in Fig. 3.10. The cut condition is defined as $|x| < 40$ and $|y| < 20$, and $|z| < 80$. The distributions of reconstructed mass and the correlation between them and momentum are shown in Fig. 3.11 We set cut region to select K^+ as shown by the red line. The momentum region of $0.9\,\mathrm{GeV}/c < p < 1.5\,\mathrm{GeV}/c$ was chosen to select the quasi-free (K^-, K^+) reaction. The cut window was tuned for each momentum with $3\,\sigma$ of a squared mass. Figure 3.12 shows the cut window to select K^+.

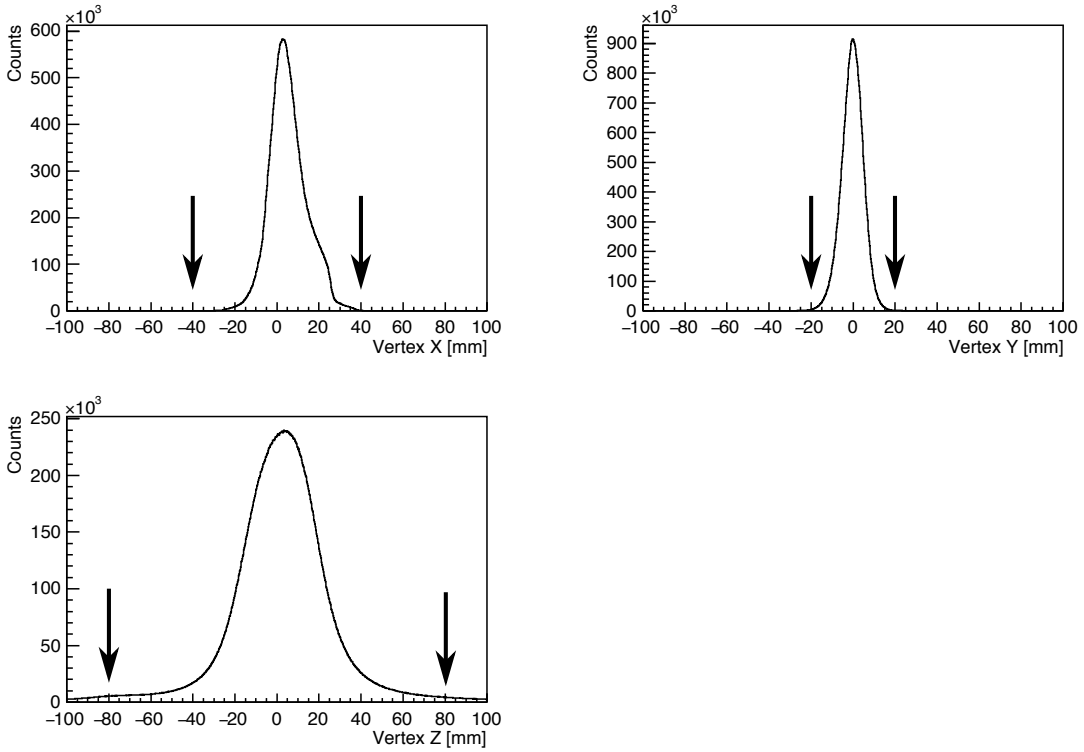

Figure 3.10: Distribution of the vertex obtained by the K18 and KURAMA tracking. The origin of XYZ coordinates is the designed center position of the target.

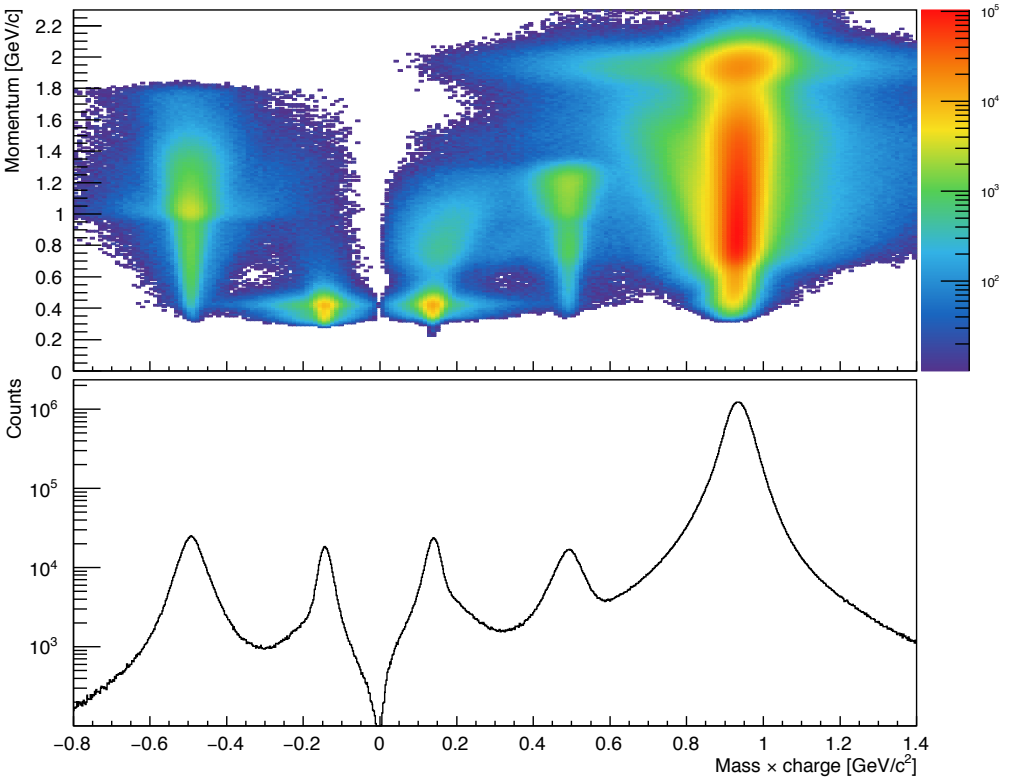

Figure 3.11: Distribution of reconstructed mass of particles in the KURAMA tracking.

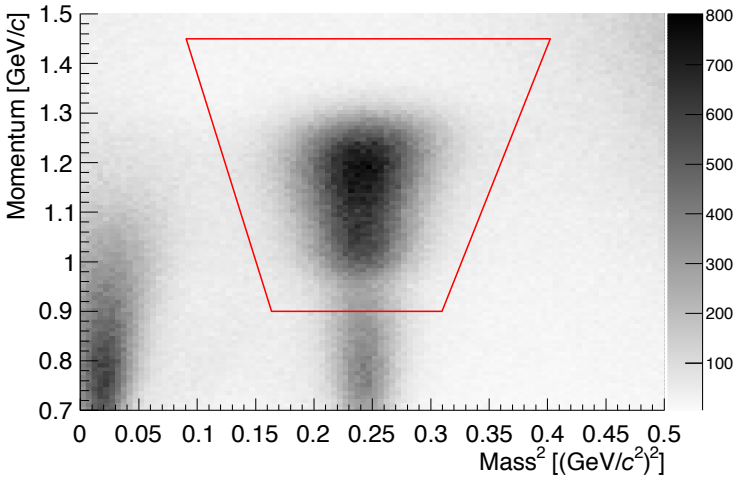

Figure 3.12: Cut region to select K^+ event which is shown as the red area. The slope of line was determined to select $3\,\sigma$ region in each momentum.

3.4 (K^-, K^+) analysis

By combining K18 tracking and KURAMA tracking, (K^-, K^+) kinematics was examined. Momentum resolution of KURAMA spectrometer was estimated by the beam-through data, in which beam passed through the K1.8 beam line spectrometer and the KURAMA spectrometer without the target and emulsion sheets. The distribution of the difference of momentum between the beam line spectrometer and KURAMA spectrometer shows resolution of KURAMA spectrometer because beam line spectrometer has much better resolution than that of KURAMA spectrometer. The momentum resolution of the beam line spectrometer was estimated as $\Delta p/p = 3.3 \times 10^{-4}$(FWHM) [13]. The momentum difference is shown in Fig. 3.13 The momentum resolution of KURAMA spectrometer was obtained to be $\Delta p/p = 2.7 \times 10^{-2}$(FWHM) at 1.2 GeV/$c$.

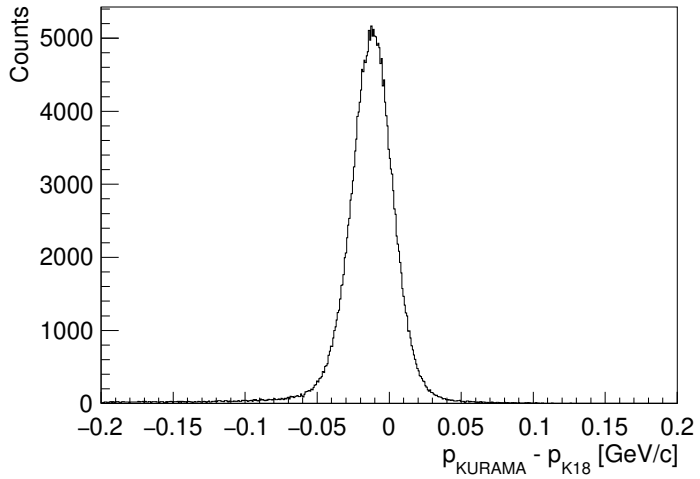

Figure 3.13: Distribution of momentum difference between K18 tracking and KURAMA tracking for 1.2 GeV/c π^- beam.

From Incoming K^- and outgoing K^+, missing momentum and missing mass were obtained. The polyethylene target (2.88 g/cm^3) data was used to calibrate the momentum of a scattered particle. The correlation between the missing mass and angle of the scattered particle is shown in Fig. 3.14. The dense regions indicate the peak of Ξ^- from the $p(K^-, K^+)\Xi^-$ reaction. The correlation caused by the difference between the calculation and real magnetic field depends on the path of the particle. The energy loss in the materials in the KURARA spectrometer such as PVAC, FAC, SCH also affected to the momentum of scattered particles. Therefore, the momentum of scattered particles was tuned to reproduce the PDG mass of Ξ^- (1321.71 GeV/c^2) by scaling their momentum depending on their angles as shown in Fig. 3.15. The distribution of the missing mass is shown in Fig. 3.16. The resolution of missing mass is obtained to be 10.4 MeV (σ). This result was consistent with a result of a Monte Carlo simulation, 9.9 MeV (σ).

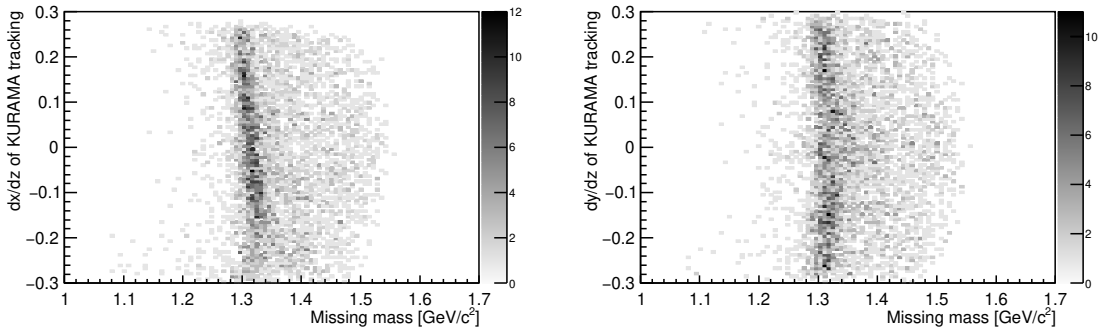

Figure 3.14: Correlation between the angle and missing mass before the correction.

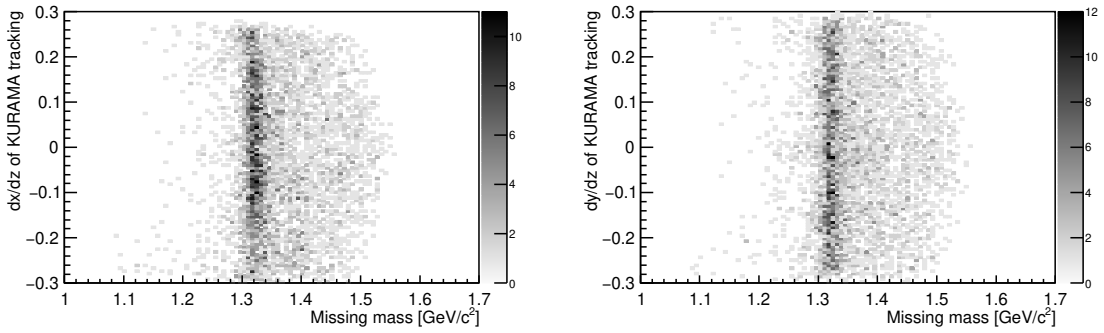

Figure 3.15: Correlation between the angle and missing mass after the correction.

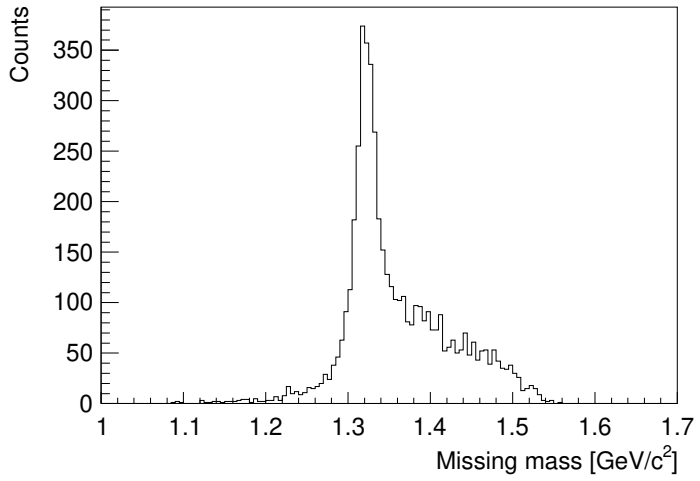

Figure 3.16: Distribution of missing mass in polyethylene target run.

3.5 Ξ^- selection

By tagging the (K^-, K^+) reaction, Ξ^- tracks were constructed from hits of the upstream SSD. Since the SSD was located close to the target, several particles related to nuclear reactions hit each SSD layer. From the huge number of hit combinations, Ξ^- tracks were extracted by several criteria. A Monte Carlo simulation with Geant4 code [46] was performed to determine the cut conditions. In the simulation, events were generated by JAM code [47] to emit K^+ by injecting $1.8\,\mathrm{GeV}/c$ K^- beam to ^{12}C target. Trigger conditions were also reproduced to correct the corresponding data set. The analysis of the simulation was done by the same procedure as the E07 data. The criteria to select Ξ^- is as follows:

(1) selecting the SSD hits with large energy deposit,

(2) examining consistency between track angle and clustering size,

(3) consistency among the energy deposits through four layers,

(4) consistency of the vertex point between K^+ and Ξ^-,

(5) kinematic constraints of the $p(K^-, K^+)\Xi^-$ reaction,

(6) selecting the target volume in the vertex fitting,

and

(7) examining the other particle track from the vertex.

(1) selecting the SSD hits with large energy deposit

The energy deposit of Ξ^- is larger than K^+ due to its low velocity. In order to reduce the ratio of fake Ξ^- tracks, we selected the SSD hits with high energy deposits for the tracking. Figure 3.17 shows the distribution of energy deposit of an SSD layer in the simulation which is normalized by the minimum ionizing particle (MIP) peak. The Ξ^- contribution shows clearly higher distribution than that of MIP. The distribution of energy deposit of each SSD layer was shown in Fig. 3.18. The energy deposit is required to be larger than twice that of MIP. The thresholds are indicated with arrows in Fig. 3.18.

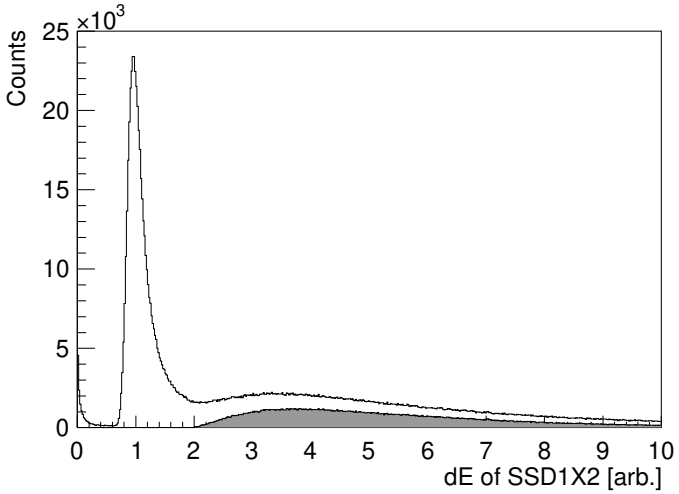

Figure 3.17: Distribution of energy deposit of each SSD layer in the simulation. Shaded region shows Ξ^-.

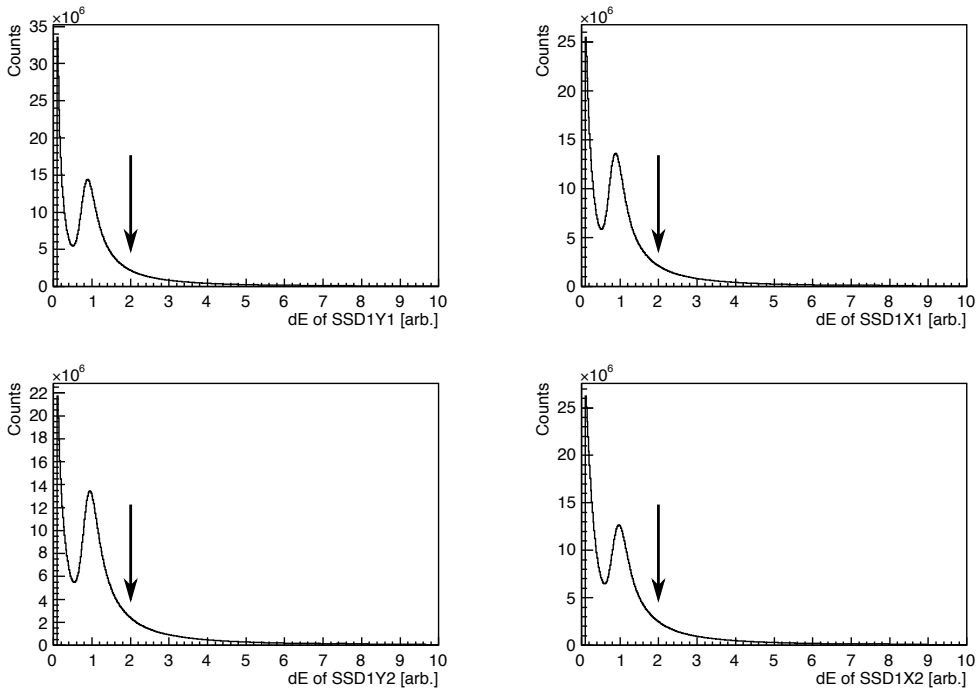

Figure 3.18: Distribution of energy deposit of each SSD layer. The enhancement of lower energy deposit were caused by noise of an SSD readout tip. Bump structure of Ξ^- is hidden by the noise and a background.

(2) examining the correlation between track angle and clustering size

One layer of SSD had a strip pitch of 50 μm and a thickness of 300 μm. When particles do not pass through the SSD layer perpendicularly, several strips have signals depending on the incident angles of the tracks as shown in Fig. 3.19. Then, from this geometrical conditions, the fake hits can be rejected in the correlation between the angle and the clustering size. The correlation of each layer is shown in Fig. 3.20. Cut regions were indicated as the red bands which is defined as $|ClSize - 6.2 \times |(dx, dy)/dz| - 0.7| < 2$ for each layer.

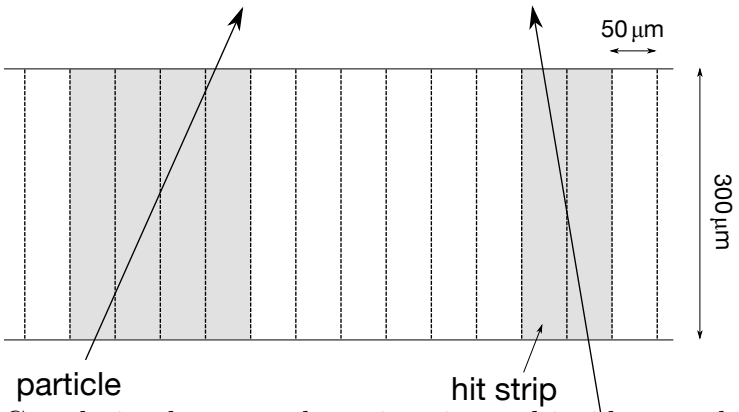

Figure 3.19: Correlation between clustering size and incident angle of each SSD layer.

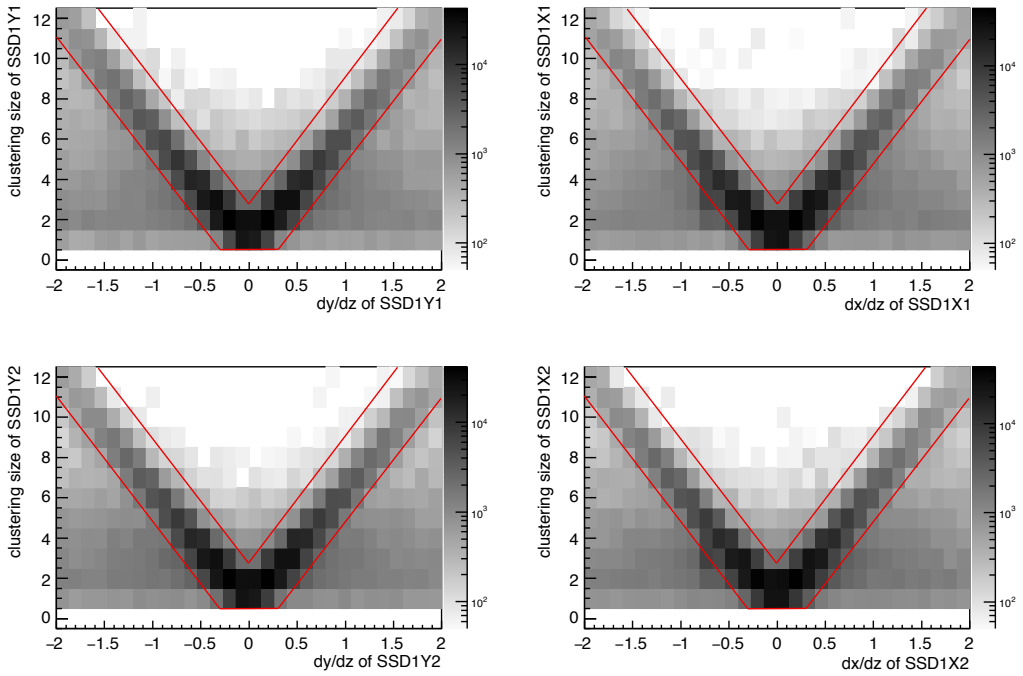

Figure 3.20: Correlation between clustering size and incident angle of each SSD layer.

(3) examining consistency among the energy deposits through four layers

This criterion was adopted to select tracks in which the same particle made hit on each layer. If a track was constructed with wrong hit combination, the deviation between energy deposits in four layers become large because another particle makes different energy deposit. We used the ratio of the unbiased variance and the mean value of energy deposits in the four layers, R, defined as the following equations:

$$R = V/E, \tag{3.4}$$

$$E = \frac{1}{4}\sum_{i=1}^{4} x_i, \tag{3.5}$$

$$V = \frac{1}{3}\sum_{i=1}^{4}(x_i - E)^2, \tag{3.6}$$

where, the x_i indicates the energy deposit of i-th layer. The distribution of R in the simulation is shown in Fig. 3.21. The shaded region shows the Ξ^- component. From this distribution, we set the threshold of 0.4 which is shown in Fig. 3.22 as an arrow.

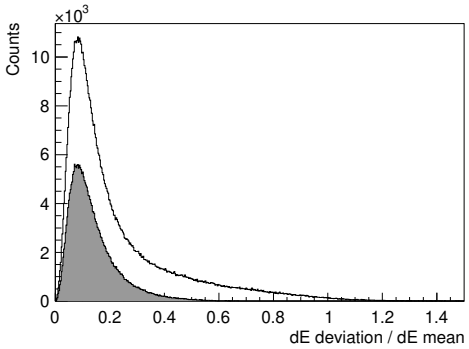

Figure 3.21: Distribution of the standard deviation of energy deposit in four layers of SSD in the simulation.

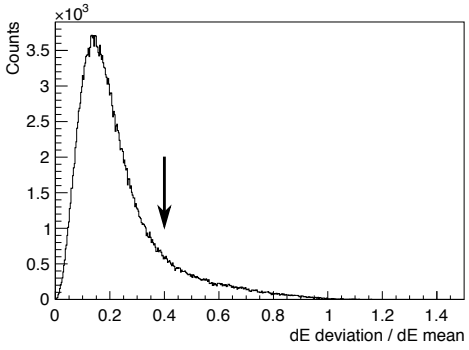

Figure 3.22: Distribution of the standard deviation of energy deposit in four layers of SSD.

(4) examining consistency of the vertex point between K^+ and Ξ^-

Tracks of K^+ and Ξ^- should be originated from the same vertex. Therefore, close two tracks were selected by examining the closest distance between them. The distribution of the closest distance is shown in Fig. 3.23. The threshold of 3 was indicated as the arrow.

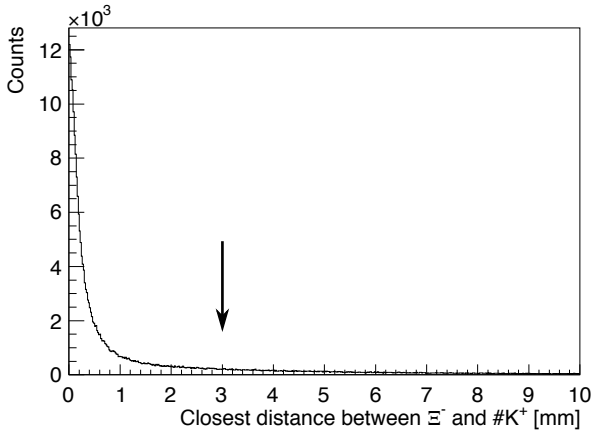

Figure 3.23: Distribution of the closest distance between the tracks of Ξ^- and K^+.

(5) examining kinematic constraints of the $p(K^-, K^+)\Xi^-$ reaction

Three tracks of K^-, K^+, and Ξ^- should intersect at one point. This condition was examined by the residual between K^- track and the vertex between K^+ and Ξ^- as shown in Fig. 3.24 (a). Since the tracks of K^+ and Ξ^- were measured precisely with the SSDs having the resolution of $15\,\mu m$, the position of this vertex is more accurate than that of K^-K^+ or $K^-\Xi^-$ vertices. The 1D and 2D plots of X and Y position residual is shown in Fig. 3.25. The selected region which is defined as $(x/4.38)^2 + (y/7.95)^2 < 1$ is indicated as the red circle in the 2D plot.

By assuming $p(K^-, K^+)\Xi^-$ kinematics, the missing momentum can be obtained from K^- and K^+ tracks. The angle residual between Ξ^- track and the missing momentum can be used to confirm Ξ^- production events (Fig. 3.24 (b)). The 1D and 2D plots of X and Y angle residual is shown in Fig. 3.26. In the case of quasi-free $p(K^-, K^+)\Xi^-$ reaction, Ξ^- angle deviated from that of the missing momentum due to the Fermi motion. Therefore, the distribution of the residual is mulch wider than the angle resolution of the SSD. The distribution of Fig. 3.26 is consistent with the simulation (Fig. 3.27). The selected region which is defined as $(x/0.87)^2 + (y/0.882)^2 < 1$ is indicated as the red circle in the 2D plot.

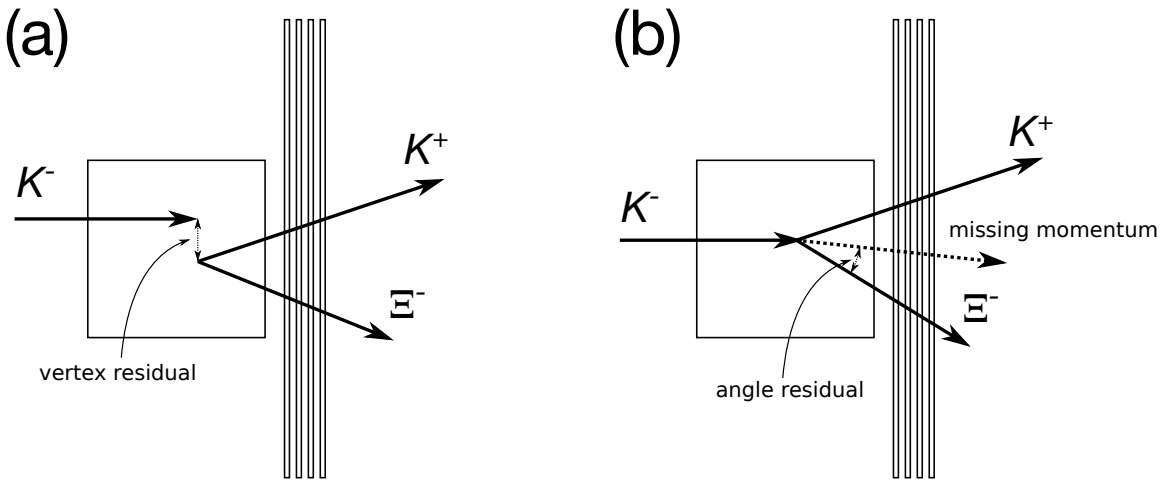

Figure 3.24: Schematic drawing of the residual of vertex (a) and angle (b). Sizes of detectors are not actual scale in this drawing.

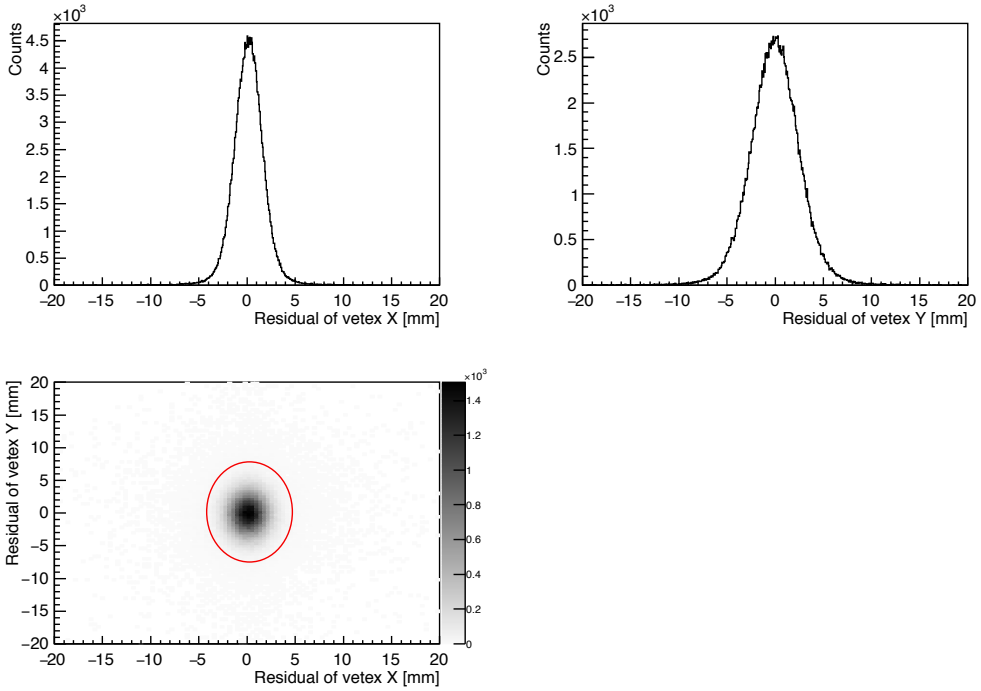

Figure 3.25: Distribution of the vertex residual.

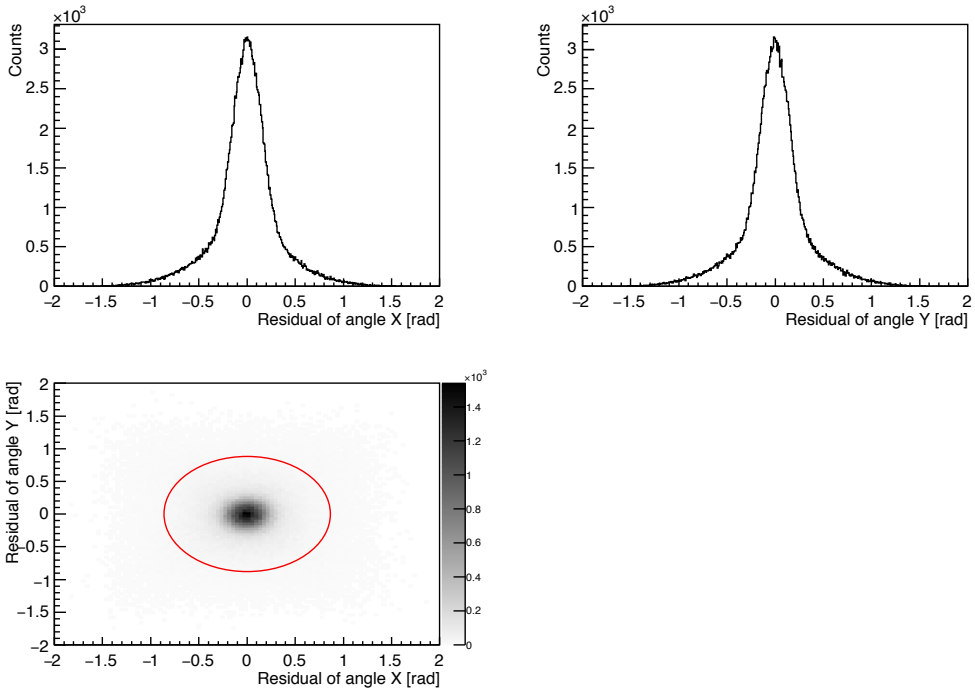

Figure 3.26: Distribution of the angle residual.

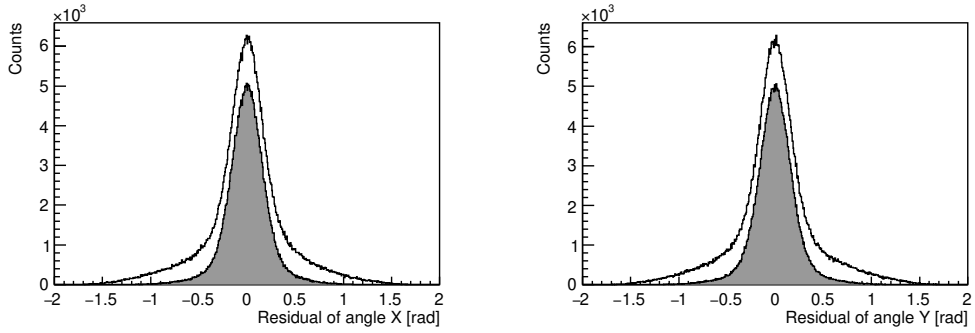

Figure 3.27: Distribution of the angle residual in the simulation.

(6) selecting the target volume in the vertex fitting

In order to select the reaction occurred in the target, the vertex obtained by fitting of K^-, K^+, and Ξ^- tracks was examined in the following method. The vertex position was estimated by MINUIT package [45] to minimize the reduced chi-square value defined with the distance between track and hit position in each detector as follows.

$$\chi^2/ndf = \frac{1}{n_{all}-9}\sum_{k=K^-,K^+,\Xi^-}\sum_{i=1}^{n_k} w_{k,i}(X^{hit}_{k,i} - f_k(z_{k,i}))^2, \tag{3.7}$$
$$n_{all} = n_{K^-} + n_{K^+} + n_{\Xi^-},$$
$$f_k(z_{k,i}) = (x_0 + u_k(z_{k,i} - z_0))\cos(\alpha_{k,i}) + (y_0 + v_k(z_{k,i} - z_0))\sin(\alpha_{k,i}),$$
$$w_{k,i} = 1/\sigma^2_{k,i},$$

where, $(n_{K^-}, n_{K^+}, n_{\Xi^-})$ indicate the number of hits in BC3 and BC4 for K^-, SSD1 and SSD2 for K^+, and SSD1 for Ξ^-, respectively. The parameters (x_0, y_0, z_0, u_k, v_k) denote the vertex position and the angle of each track, respectively. The hit position, z position, tilt angle, and intrinsic resolution for each hit plane are represented as $X^{hit}_{k,i}$, $z_{k,i}$, $\alpha_{k,i}$, and $\sigma_{k,i}$, respectively.

The distribution of the reduced chi-square is shown in Fig. 3.28. If its value is large, such candidate was excluded. The threshold of 10 is indicated as an arrow. The distribution of estimated x, y, and z axes of the vertex is shown in Fig. 3.29. The selected conditions is defined as $|x| < 28$, $|y| < 20$, $-25 < z$, and $Z < 18$ according to the target size.

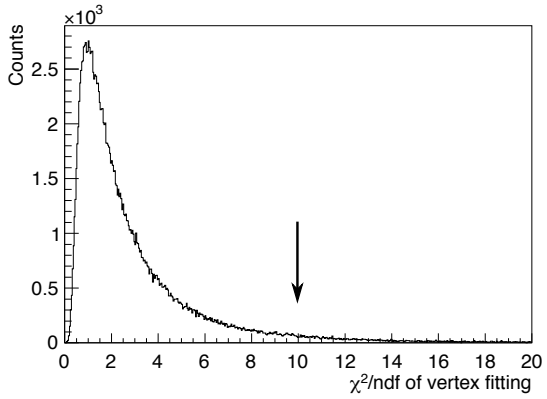

Figure 3.28: Distribution of χ^2/ndf in the vertex fitting.

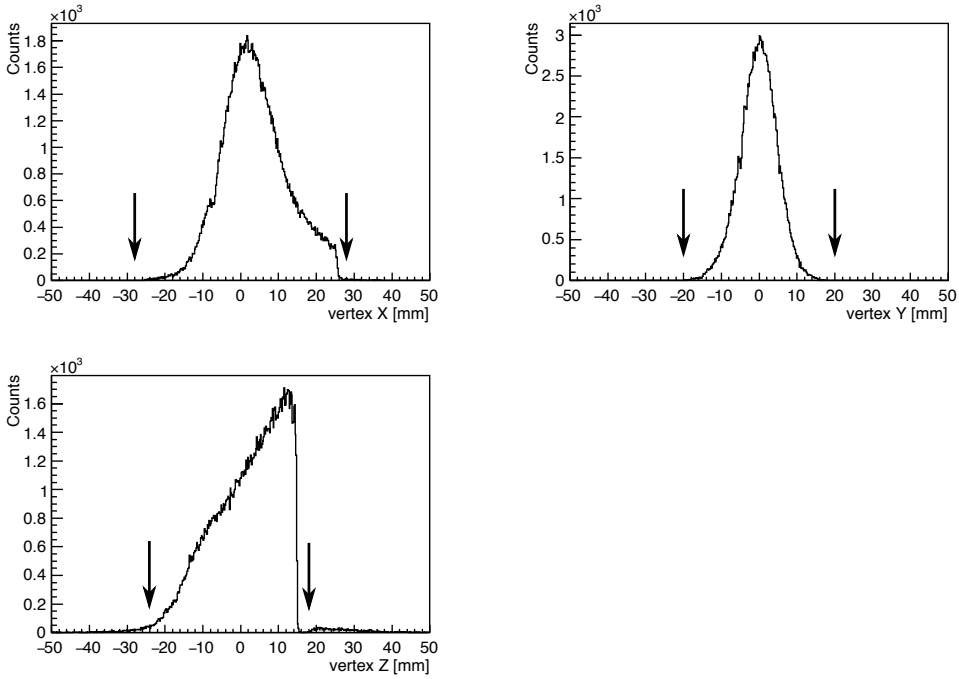

Figure 3.29: Distribution of vertex obtained by the fitting.

(7) examining the other particle track from the vertex

Protons from Ξ^- decay are contaminated in Ξ^- track candidates.

$$\Xi^- \to \Lambda + \pi^- \\ \hookrightarrow p + \pi^-$$

These decay events can be excluded by detecting π^- tracks with the SSD. Tracks of π^- was examined by difference from the vertex given by tracks of K^+ and Ξ^- in the following criteria.

(1) constructing tracks from hits of four layers of SSD1 which do not belong to Ξ^- or K^+ track

(2) extrapolating the constructed tracks to the z position of the vertex point obtained in the vertex fitting

(3) examining the residual from the x and y positions of the vertex

Figure 3.30 shows the XY residual of the π^- candidates. In the case of multi tracks in SSD1, the closest track to the vertex was selected as a π^- track candidate. The selected condition was defined as $|X| < 5$ and $|Y| < 5$ which are indicated as arrows in Fig. 3.30. The distribution of the energy deposit of π^- candidates is shown in Fig. 3.31. Tracks with small energy deposit were chosen with the threshold of 4 to exclude π^- in order to avoid excluding protons which associated to Ξ^- came from evaporation of a nucleus. Figure 3.32 shows the corresponding distribution in the simulation. The π^- component shows the low energy deposit.

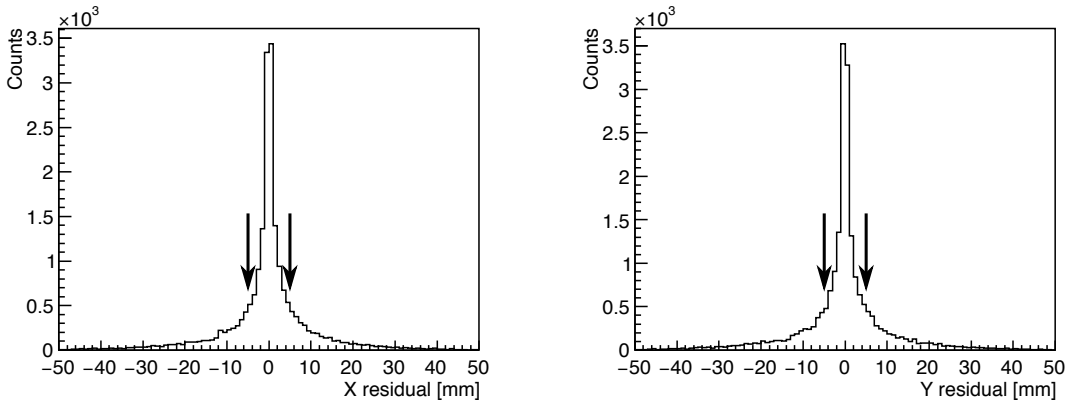

Figure 3.30: Distribution of the residual of π^- candidates.

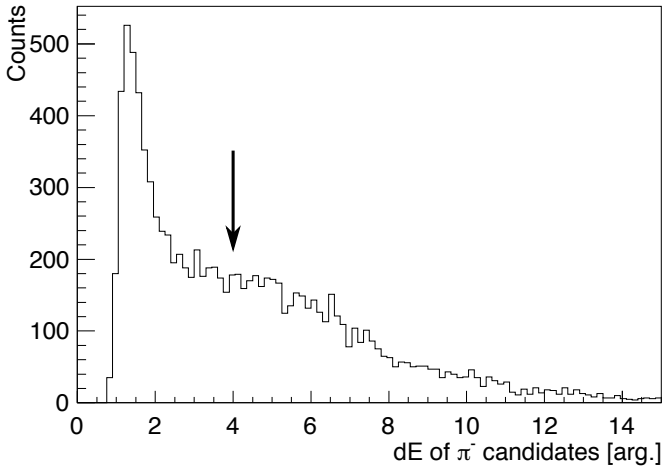

Figure 3.31: Distribution of the energy deposit π^- candidates.

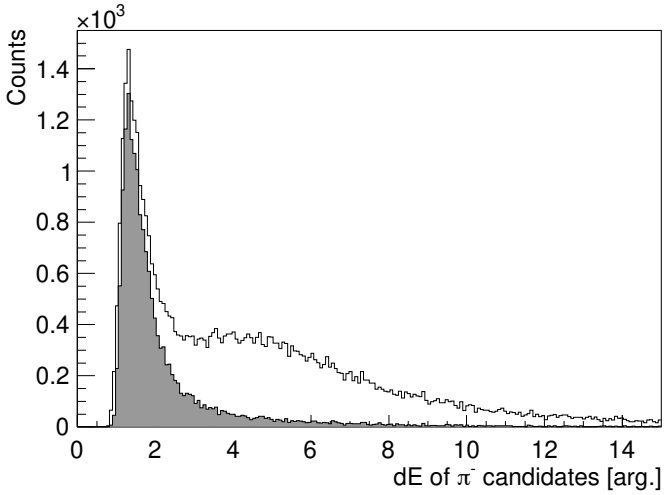

Figure 3.32: Distribution of the energy deposit π^- candidates in the simulation. Shaded region shows the π^- component.

From the above criteria, Ξ^- candidates were selected in the SSD hits. The distribution of the mean energy deposit of the SSD four layers for K^+ and Ξ^- in data and the simulation are shown in Fig. 3.33. The energy deposit is normalized by the path length in the SSD in order to associate the momentum of the particle. Although the data shows wider peak structure for K^+ due to noise and energy resolution, these spectra are consistent. Figure 3.34 shows the zenith angles of Ξ^- candidates and these are also consistent. Therefore, we confirmed that the simulation reproduced the data well.

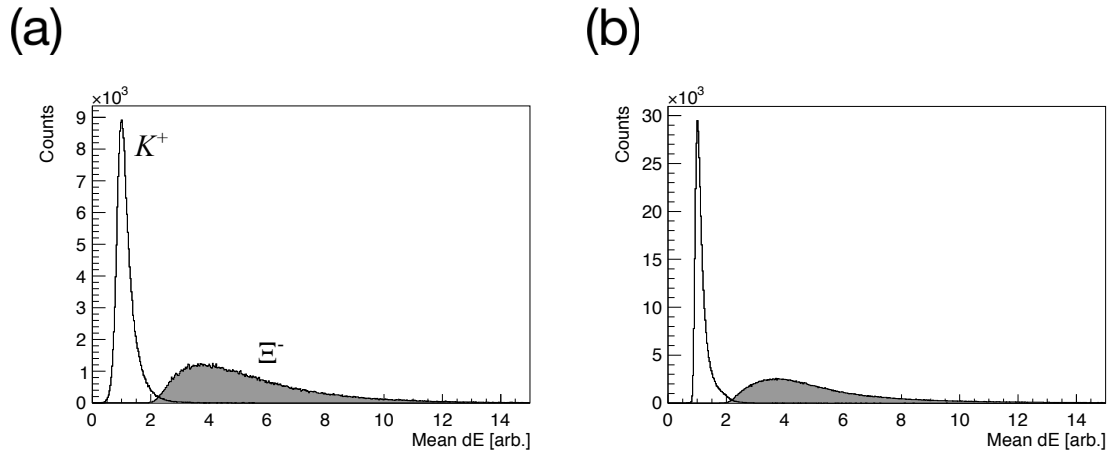

Figure 3.33: Distribution of the energy deposit of Ξ^- candidates and K^+. Shaded region shows Ξ^- candidates. (a) data (b) simulation.

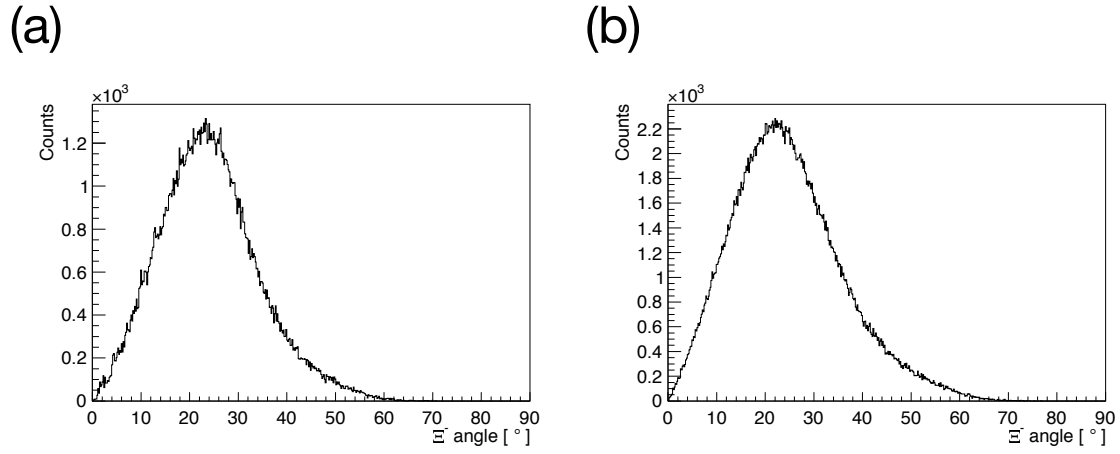

Figure 3.34: Distribution of the zenith angle of Ξ^- candidates. (a) data (b) simulation.

In order to observe double hypernuclei, we should detect the stopping point of Ξ^-. Since the ratio of the Ξ^- stopping events in the reconstructed Ξ^- tracks is small due to decays before the stopping or penetrating all emulsion sheets, it is time-consuming to scan all these candidates. The following criteria were further required to enhance the Ξ^- stopping probability.

(1) selecting large energy deposit events

(2) examining the Ξ^- track in SSD2

With these criteria, the Ξ^- stopping ratio was increased from 5.0% to 19% in the simulation. The detail of each criterion is shown as follows:

(1) selecting large energy deposit events

A Ξ^- which stops in an emulsion had large energy deposit on the SSDs because of the low momentum of Ξ^-. Figure 3.35 shows the mean energy deposit of four layers of SSD for Ξ^- tracks in the simulation. We set the dE/dx threshold for the Ξ^- stopping events at six times of the dE/dx for the MIP.

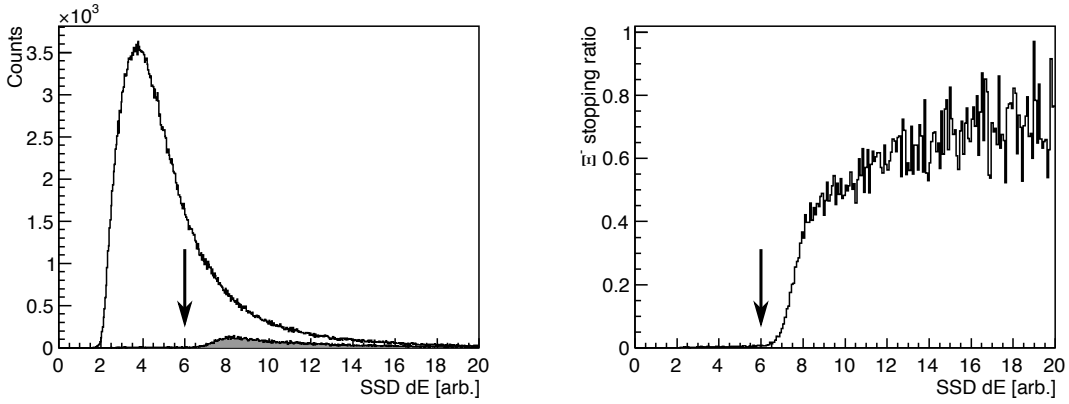

Figure 3.35: Distribution of energy deposit on SSD for Ξ^- obtained by the simulation. Shaded region shows Ξ^- which stopped in the emulsion module. Right figure shows Ξ^- stopping ratio at each energy deposit.

(2) examining the Ξ^- track in SSD2

A Ξ^- track can penetrate through the emulsion module. Since these tracks can be identified with the SSD2, the matching of the SSD1 track with the SSD2 hit was examined. The residual from the extrapolation of SSD1 track on a SSD2 layer was examined as shown in Fig. 3.36. Figure 3.37 shows the correlation between the energy deposit and the residual from the extrapolation of Ξ^- track on SSD2. The indicated region which is defined as $dE > 2$ and $|X| < 2.26$ ($|Y| < 2.32$) is tagged as Ξ^-. When the first(X) and second(Y) layers of SSD2 have extrapolation hit, such Ξ^- was excluded.

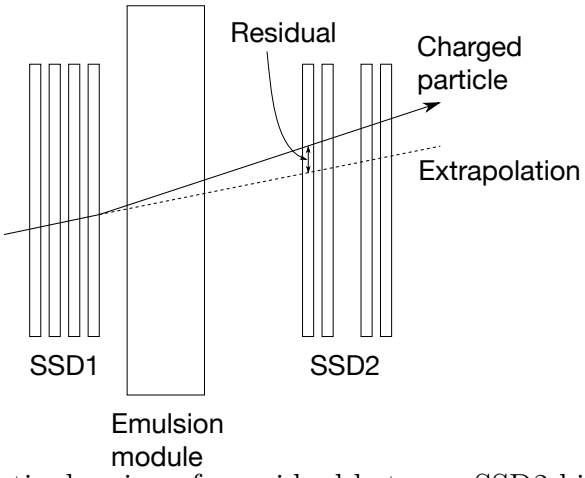

Figure 3.36: Schematic drawing of a residual between SSD2 hit position and a extrapolation from the SSD1 track. Sizes of detectors are not actual scale in this drawing.

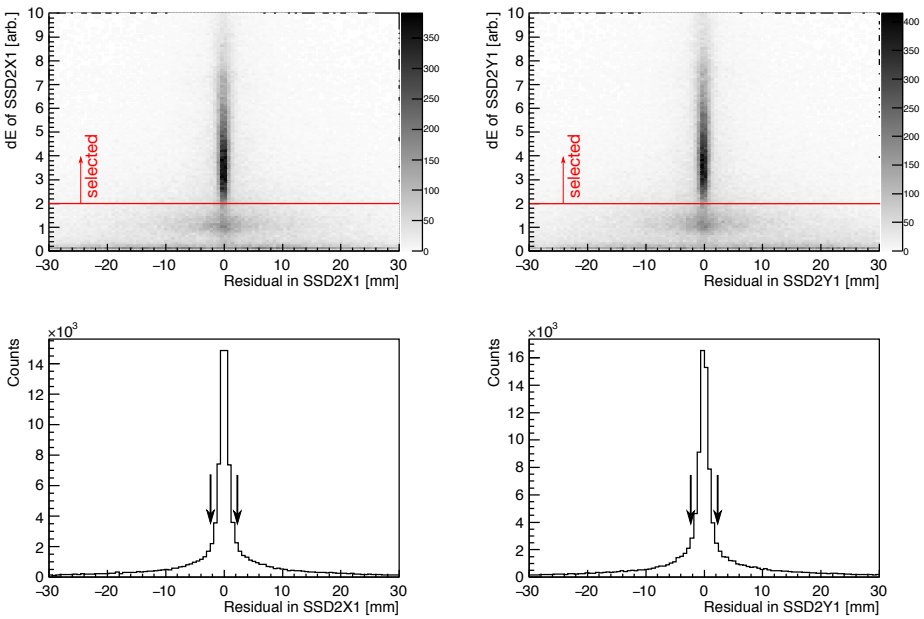

Figure 3.37: Distribution of the residual between SSD2 and the extrapolation from SSD1.

3.6 Ξ^- stopping yield estimation

From the criteria in the last section, Ξ^- candidates which have large stopping probability were selected. The Ξ^- stopping yield was estimated from the yield of Ξ^- candidates and the sopping ratio obtained by the simulation. However, the Ξ^- candidates were contaminated by particles which were produced in (K^-, p) and (K^-, π^+) reactions. Those components were estimated from the distribution of squared mass of outgoing particles after the Ξ^- selection criteria. Figure 3.38 shows the squared mass distribution of outgoing particles in the Ξ^- event candidates without the squared mass selection. The number of K^+ was obtained by fitting this distribution with the Gaussian and 1D-polynomial background. Since the momentum and the squared mass had a correlation, this fitting was done by dividing each momentum band (See Appendix A). Then, the Ξ^- stopping yield was estimated by taking the stopping probability into account which was obtained by the simulation. However, there were Ξ^- stopping events which should be recorded but was rejected by the Ξ^- selection criteria. Therefore, the total number of recorded Ξ^- stopping events was also estimated from the simulation. The result of Ξ^- stopping yield estimation is listed in Table 3.1. We can obtain 8500 Ξ^- stopping events with the criteria.

The number of tracks to trace in emulsion sheets is about 450/module. It takes one week to scan all sheets of one module in the current condition. In order to scan more Ξ^- stopping events, we prepared another cut criteria which can cover 94% of the total Ξ^- stop by scanning 850/module tracks additionally; we can collect 10^4 Ξ^- stop in future.

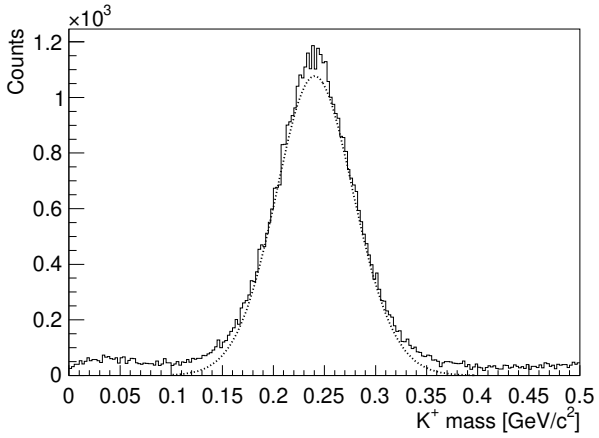

Figure 3.38: Distribution of the squared mass of K^+ after the Ξ^- selection criteria without squared mass cut. The dotted line shows the component of K^+ obtained by fitting with the Gaussian and 1D-polynomial function.

Table 3.1: Estimation of Ξ^- stopping yield.

Year	Modules	Ξ^- event	Ξ^- event with K^+ cut	Ξ^- stop	total Ξ^- stop
2016	18	5511	5000	750	930
2017	100	43957	41500	7800	10000

Chapter 4

Analysis II - Emulsion

4.1 Outline

From the sets of the predicted position and angle of the Ξ^- hyperons given with the SSD, they were traced through the emulsion sheets with automated microscope scanning systems [48]. At first, the most upstream sheet of an emulsion module was scanned to find the Ξ^- tracks. Once found, the Ξ^- track was traced to downstream through several emulsion sheets. When the microscope system detected the end point of the track in the sheet, the system took pictures around the Ξ^- stopping point and those were examined by human eyes. After an impressive event is observed, such an event was carefully analyzed to identify the nuclear species. The ranges and angles of the tracks were measured by fitting tracks around the vertices in the image analysis. The energies of the daughter particles were estimated from the ranges of the tracks with the Range energy formula. Possible nuclide combination was selected by checking the kinematic constraints at each vertex. In this chapter, the procedure to scan Ξ^- tracks in emulsion sheets and the method to analyze an observed event are explained.

4.2 Microscope scanning system

Developed emulsion sheets were scanned by microscope scanning systems. The microscope systems consisted of an image sensor, a movable stage controlled by a computer, and optics. Figure 4.1 shows the diagram of the system. The emulsion sheet was fixed on the glass stage by vacuum pumping in the observation. The Z axis of the coordinate system of the scanning was defined to the thickness direction. The stage is moved by stepping motors on XY axis recording its position with position encoders with a resolution of $1\,\mu$m attached on the rails. The brightness of microscope images was controlled by an LED which was attached under the stage. Silicone immersion oil was poured on the emulsion sheet to use oil-immersion objective lenses. Z position of the focal plane was tuned by moving the objective lens by a stepping motor. Its position was also recorded with a position encoder with a resolution of $0.1\,\mu$m. Optical images in the emulsion sheet were read by the CCD sensor through the objective lens. Several magnification types of objective lenses were used depending on the situation. Photographs obtained with the image sensor were recorded in pixel data which have $512(X) \times 440(Y)$ pixels with-8 bit

resolution of the brightness.

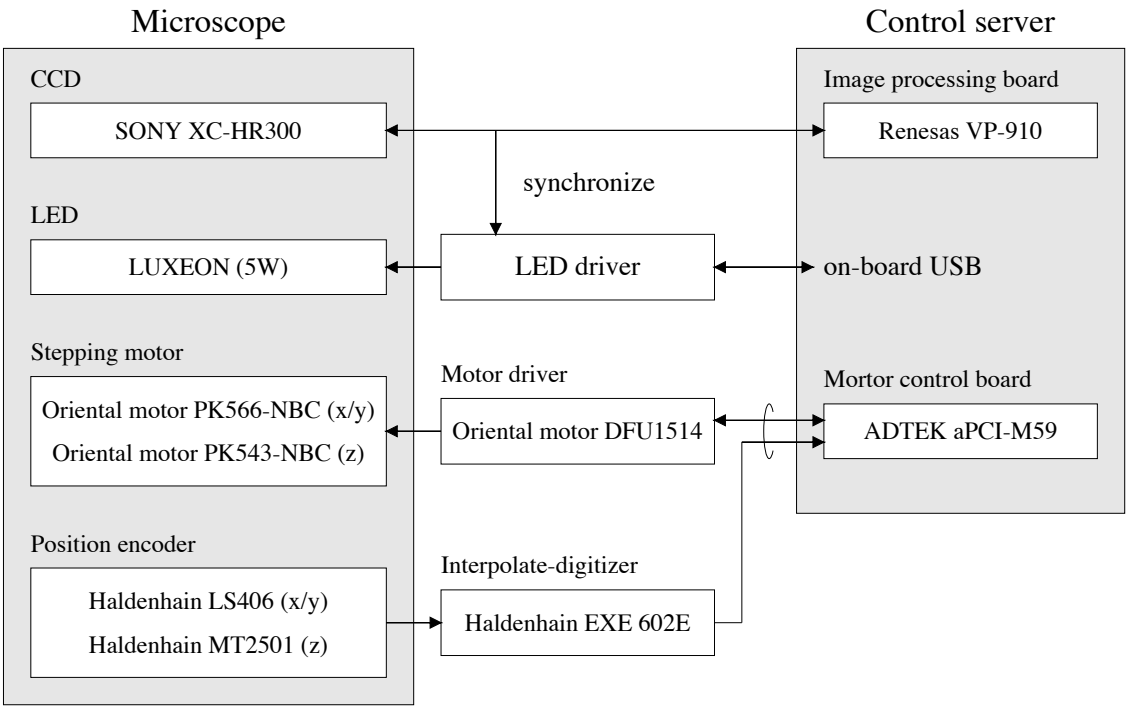

Figure 4.1: The diagram of the microscope scanning system.

4.3 Ξ^- following

4.3.1 Grid mark correction

Emulsion sheets were deformed from the beam exposure period due to the photograph development. These deformations were corrected using grid patterns which were printed just after beam exposure by irradiating strobe lightning with a template which was made from aluminum (2016 run) and copper (2017 run) plate having 50 μm holes with a distance of 1 cm. Each track position was corrected to reconstruct original positions of grid marks by an affine transformation. Figure 4.2 shows a typical deformation of a thick-type sheet.

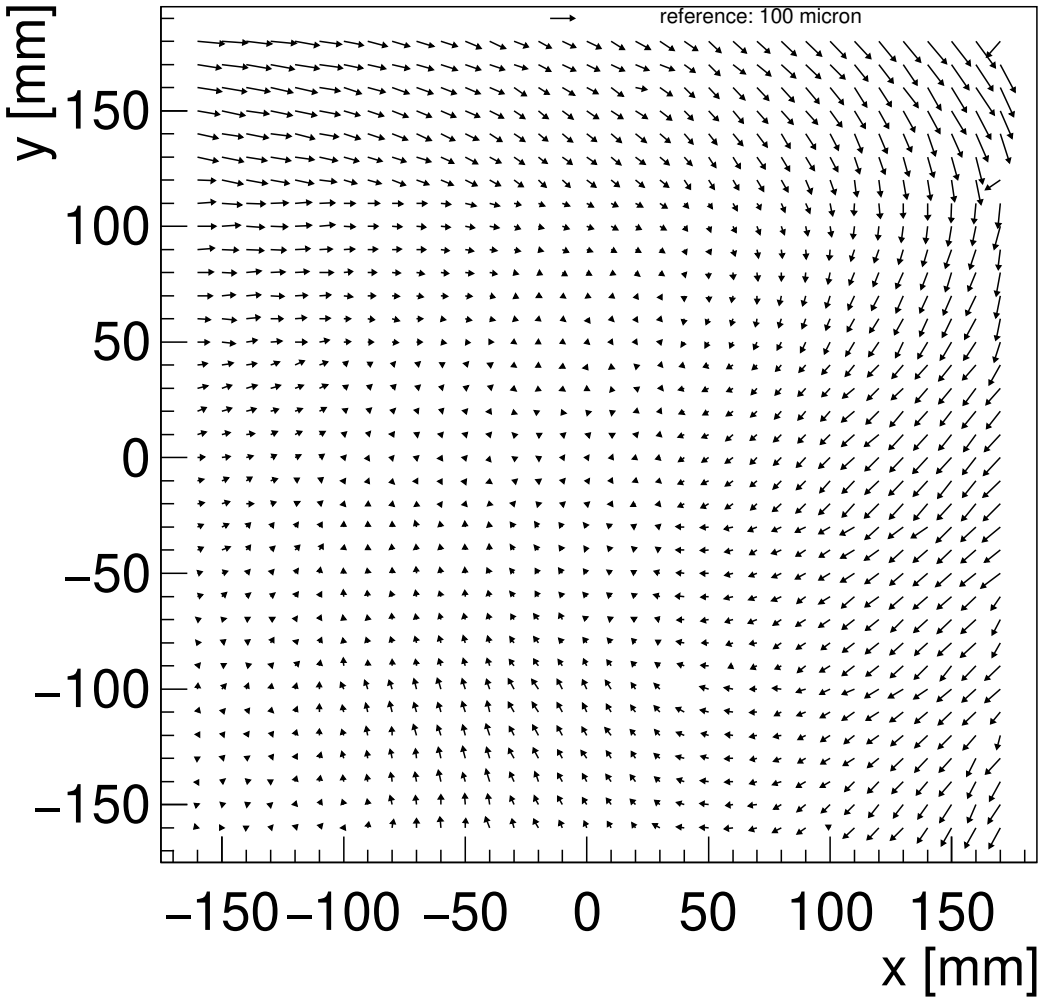

Figure 4.2: A typical deformation of a thin-type sheet. The angle and size of deformation in each position is shown as arrows. The reference of deformation size is shown in the top.

4.3.2 $\overline{p}$ pattern matching

In order to connect Ξ^- tracks to emulsion module from the SSD, the relative position between them should be aligned with a few dozen μm accuracy. Since the positions of emulsion sheets in the emulsion cassette varies depending on packing, every module should be calibrated. It was achieved with a $\overline{p}$ pattern matching method. 1.8 GeV/c $\overline{p}$ beam were irradiated on four corners of the module before the exposure of K^- beam. The density and exposed area of $\overline{p}$ beam were controlled to 10^3 particles/cm^2 and 10 mm (σ), respectively. Since $\overline{p}$ beam penetrated the SSD and the module straight, the same patterns of $\overline{p}$ tracks were recorded in the both. Therefore, alignment between the SSD and the module was adjusted by using this pattern matching.

The relative position of beam patterns was adjusted by checking all combinations of track position between the module and SSD. Tracks in emulsion were searched in both of the upstream and downstream layers. Detection procedure of emulsion tracks is written in Sec. 4.3.3. Figure 4.3 shows the result of the pattern matching. The accuracy of the relative position was obtained to be 20 μm.

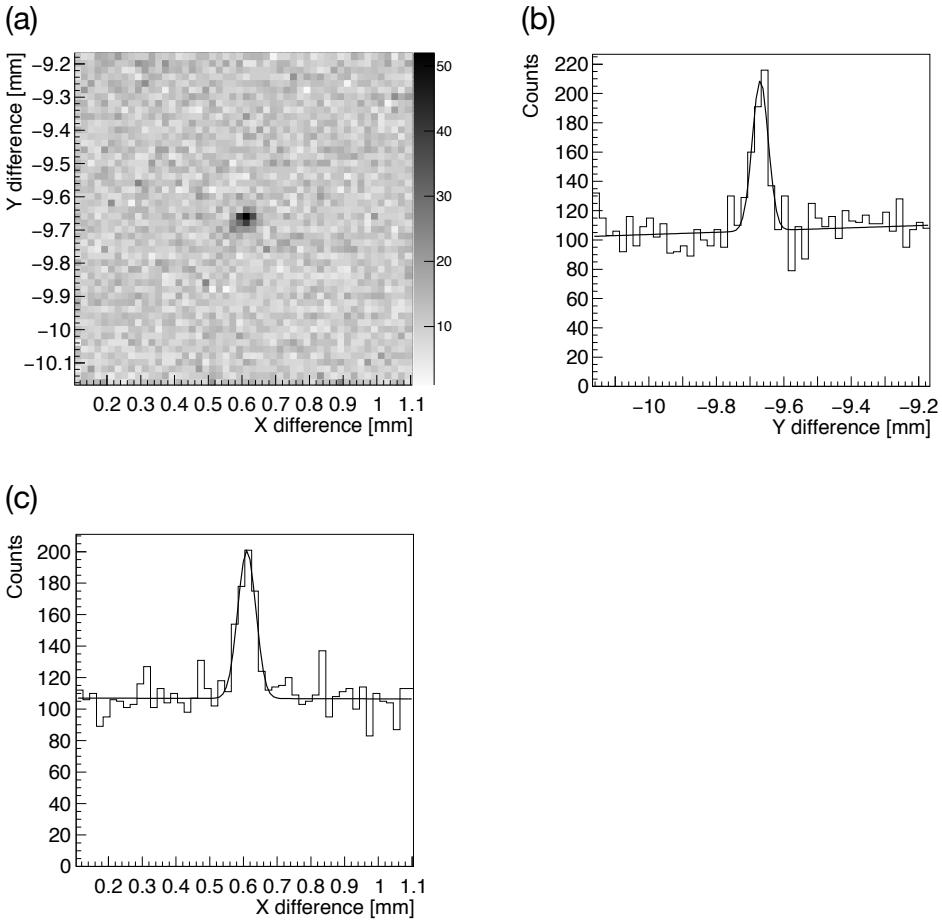

Figure 4.3: Result of the $\overline{p}$ pattern matching. The prominent peak indicates the correspondence of $\overline{p}$ beam patterns. (a) 2D plot (XY). (b) 1D plot (Y). (c) 1D plot (X).

4.3.3 Scanning of the first sheet

From the prediction of a Ξ^- track obtained from Section 3.5, they were searched in the first thin-type sheet within an area of about $\pm 400\,\mu m$ depending on the track angle for each prediction. The Ξ^- track was searched in both of upstream and downstream of emulsion layers. By checking the connection of tracks between two layers, tracks passing through the sheet were defined. In order to correct the shrinkage effect due to photographic development, the shrinkage factors of both emulsion layers were tuned to optimize the track connection. In order to connect the Ξ^- track to the first sheet, the distance between SSD and the emulsion module should be tuned precisely. It was done with 0.1 mm accuracy by checking the correlation between the angle of tracks and position difference from the prediction. Ξ^- track candidates to follow were chosen by checking differences from the predicted position and angle. Figure 4.4 shows the typical cut conditions which is defined as $dX^2 + dY^2 < 0.4^2$ and $dAX^2 + dAY^2 < 0.05^2$.

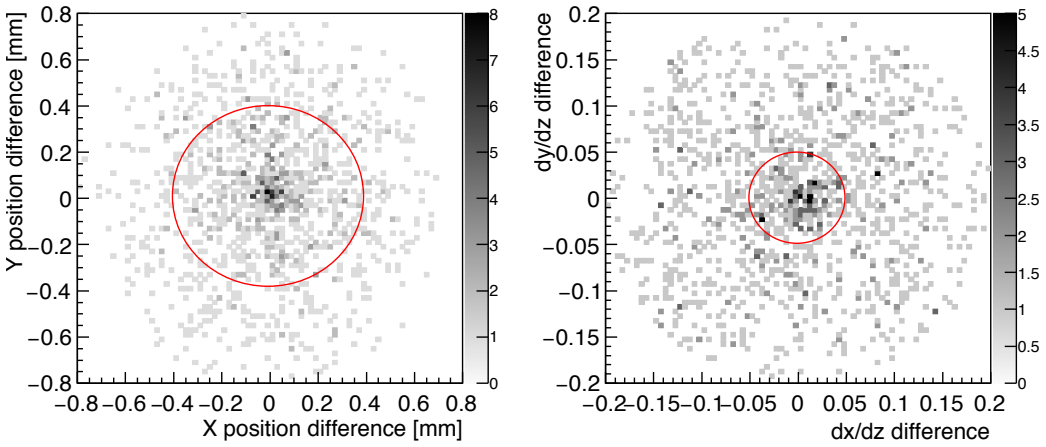

Figure 4.4: Cut condition of the first sheet scanning. (a) Position difference of the track from the prediction. (b) Angle difference of the track from the prediction.

4.3.4 Track following

Ξ^- tracks were followed from the first sheet to the downstream sheets with automated tracking systems [48]. The microscope system traced each track from the upstream to the downstream by recording its position. When a track penetrated an emulsion sheet, the exit position and angle were recorded with a beam track pattern around there. After all tracks were traced in one sheet, they were connected to the next sheet. Each track was searched by adjusting the relative position between two sheets with the pattern matching method around the track. This accuracy was obtained to be about $1\,\mu m$. When the system detects the end point of the track, the system took photographs around the stopping point. They were checked by human eyes and categorized into the following groups. Schematic drawings of each group are shown in Fig. 4.5.

(1) ρ stop : The Ξ^- track stop without nuclear fragments. The track become dizzy near the stopping point.

(2) σ stop : The Ξ^- track stop with any nuclear fragment. The track become dizzy near the stopping point.

(3) Ξ^- decay : $\Xi^- \to \Lambda + \pi^-$ decay event. The straight Ξ^- track disappear and a thin track is started from the end point.

(4) secondary interaction : The in-flight interaction between Ξ^- hyperon and a nucleus in the emulsion. The straight Ξ^- track is connected to nuclear fragments.

(5) beam interaction : The misidentification of Ξ^- track. The followed track is a fragment from an interaction between K^- beam and a nucleus in the emulsion. The followed track is connected to a star event caused by the K^- beam.

(6) through : The Ξ^- track penetrate all emulsion sheets.

(7) others

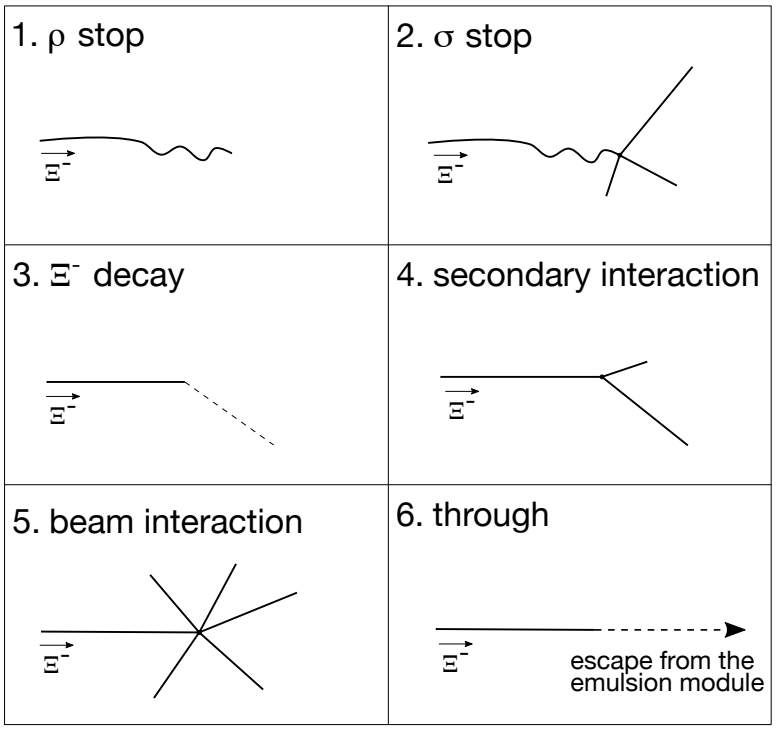

Figure 4.5: Schematic drawings of Ξ^- track categorization. An arrow in each drawing shows the direction of the track.

A part of σ stop events was categorized into double strangeness events, which include double- and twin-Λ hypernuclear events. Double-Λ hypernuclear events were identified by sequential two decay vertices associated with the Ξ^- stopping point. On the other hand, if two sets of decay vertices branched from the Ξ^- stopping point, such an event was categorized into twin-Λ hypernuclear event.

We have scanned 70 % of emulsions with fast analysis conditions to keep a good S/N ratio so far. The accumulated number of σ stop events was 1660 which include 27 double strangeness events. Among them, a clear double-Λ hypernuclear event, "MINO", was included. The detailed analysis of this event is explained in chapter 5.

4.4 Measurement of track range and angle

The ranges and the angles of tracks are required to perform the kinematic analysis for an observed event. Thus, we have developed a measurement algorithm to obtain the ranges and the angles by fitting digital images of photographs. Several hundred photographs were taken for the observed event by changing the focal length (Z axis) to scan enough depth of tracks in the event. Each image was subtracted by Gaussian blurred image to enhance the tracks from the background. Figure 4.6 shows the effect of this procedure.

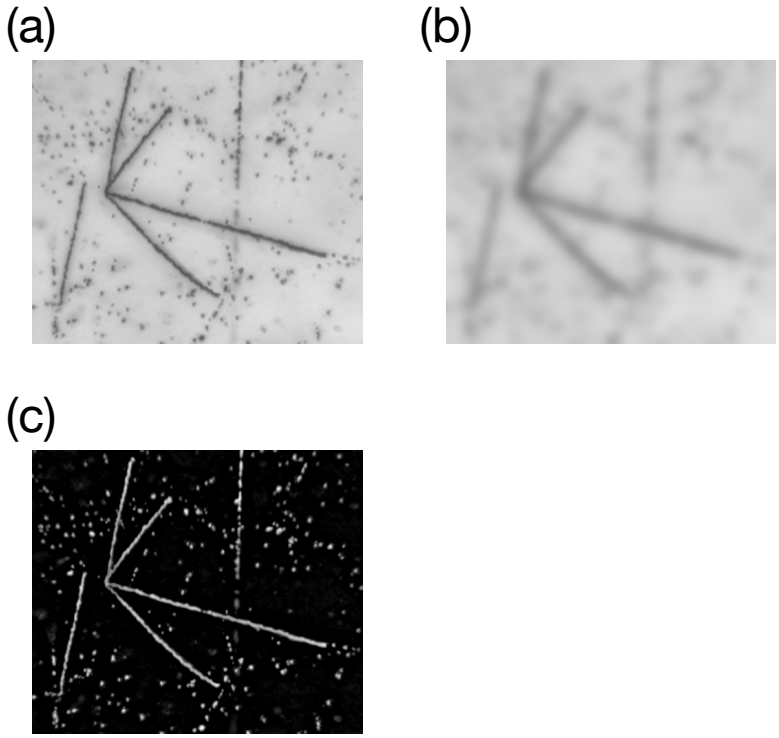

Figure 4.6: The effect of subtracting blurred image.(a) An original photograph. This photograph was obtained by summarizing several photographs in the different Z coordinate to contain all tracks of an α decay event. (b) A blurred photograph from (a). (c) A subtracted photograph ((a) - (b)). The brightness of each pixel was scaled to make particle tracks conspicuous. This procedure was adopted to each Z coordinate photograph for the image analysis.

In order to perform the linear fitting for tracks from the vertex, tracks were parameterized in θ_i, ϕ_i, and the vertex position (x_0, y_0, z_0). Z coordinate was multiplied by the shrinkage factor (described in Section 4.6 in detail) to reproduce the track before the photograph development. Parameters θ_i and ϕ_i denote a zenith and azimuthal angles of

i-th track, respectively. The fitting was evaluated by chi-square value obtained by the distance between the fitting function and points on the tracks (See Fig. 4.7) as follows:

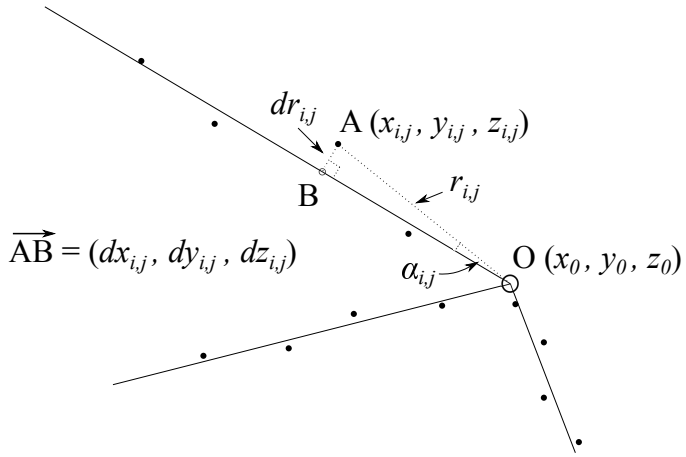

Figure 4.7: Schematic drawing of the evaluation of χ^2. (closed circle) fitted points, (solid line) estimated track.

$$
\begin{aligned}
\chi^2/ndf &= \frac{1}{2N_{all} - N_{par}} \sum_{i=1}^{n} \sum_{j=1}^{m_i} w_{i,j} (r_{i,j} \sin\alpha_{i,j})^2, \qquad (4.1)\\
N_{all} &= \sum_{i=1}^{n} m_i,\\
N_{par} &= 3 + 2n,\\
r_{i,j} &= \sqrt{(x_{i,j} - x_0)^2 + (y_{i,j} - y_0)^2 + (z_{i,j} - z_0)^2},\\
\cos\alpha_{i,j} &= \frac{(x_{i,j} - x_0)\sin\theta_i \cos\phi_i + (y_{i,j} - y_0)\sin\theta_i \sin\phi_i + (z_{i,j} - z_0)\cos\theta_i}{r_{i,j}},\\
\sin\alpha_{i,j} &= \sqrt{1 - \cos^2\alpha_{i,j}},\\
w_{i,j} &= \frac{1}{(\frac{\sigma_x dx_{i,j}}{dr_{i,j}})^2 + (\frac{\sigma_y dy_{i,j}}{dr_{i,j}})^2 + (\frac{\sigma_z dz_{i,j}}{dr_{i,j}})^2},\\
&\begin{cases}
dx_{i,j} = r_{i,j}\cos\alpha_{i,j}\sin\theta_i\cos\phi_i - (x_{i,j} - x_0),\\
dy_{i,j} = r_{i,j}\cos\alpha_{i,j}\sin\theta_i\sin\phi_i - (y_{i,j} - y_0),\\
dz_{i,j} = r_{i,j}\cos\alpha_{i,j}\cos\theta_i - (z_{i,j} - z_0),\\
dr_{i,j} = r_{i,j}\sin\alpha_{i,j} = \sqrt{dx_{i,j}^2 + dy_{i,j}^2 + dz_{i,j}^2}.
\end{cases}
\end{aligned}
$$

where, n indicates the number of track and m_i denotes the number of points used in the i-th track fitting. Ten points in $10\,\mu$m from the vertex were typically used for each track. The coordinate of j-th fitted point on i-th track is indicated as $(x_{i,j}, y_{i,j}, z_0)$. The weight factor $w_{i,j}$ depends on the angle of a perpendicular line to the track. The resolutions of $\sigma_x = 0.2\,\mu$m, $\sigma_y = 0.2\,\mu$m, and $\sigma_z = 0.5\,\mu$m, which were typical values obtained by past

measurements were adopted in this analysis. The optimal fitting result was obtained by iteration. Procedures of angle measurement are as follows:

(1) set initial points on tracks by human hands

(2) obtain θ_i, ϕ_i, and vertex position (x_0, y_0, z_0) by fitting

(3) iterate picking up the points and fitting until the parameters converge

Ten points were picked up as samples of hit positions which were defined as fitting in XY plane and Z axis of the images. Figure 4.8 shows the typical distributions of the brightness in the XY plane perpendicularly to the azimuthal angle (b) and in the Z axis (c) on the predicted point. The position of each image pixel have discrete value according to its size. Thus, the brightness of an arbitrary position was obtained by interpretation from neighbor corners of the lattice of pixels. Figure 4.9 shows a sample of the result of the angle measurement.

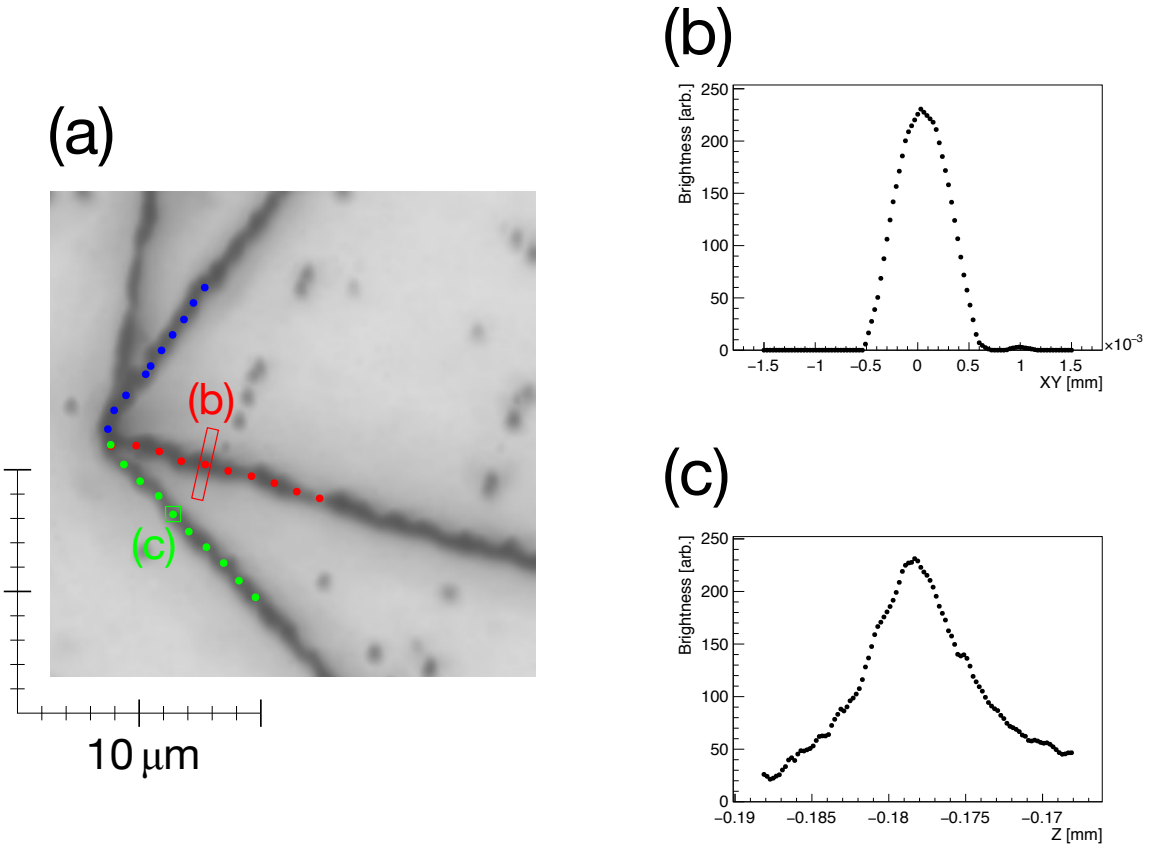

Figure 4.8: A sample of points on tracks to fit an α decay event. (a) Ten points on each track which are picked up from the last iteration result. (b) The typical distribution of brightness on the XY plane. This sample shows the red box region in (a). (c) The typical distribution of brightness on the Z axis. This sample shows the green box region in (a).

The ranges of tracks were obtained by connecting short segments. In the case of a short track which was fully contained in the field of view of the image sensor, each short

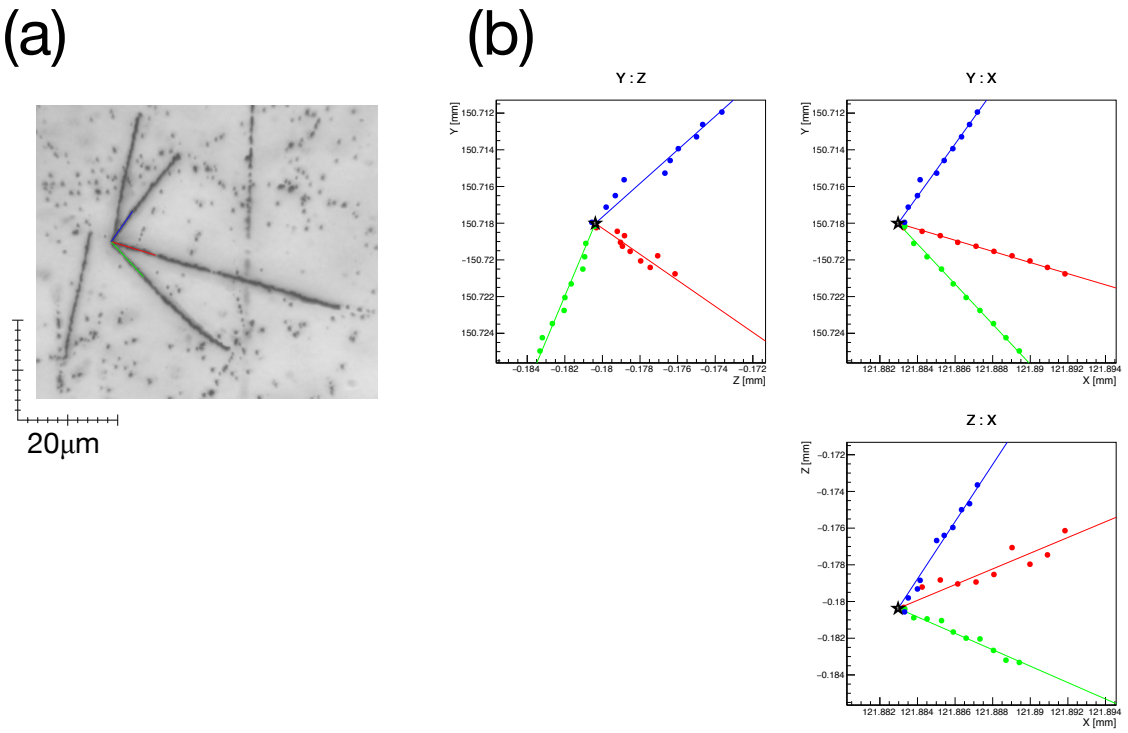

Figure 4.9: The typical result of the angle fitting of an α decay event. (a) Fitting regions are shown on each track with colored lines. The typical length of the fitting region is $10\,\mu$m from the vertex. (b) A result of the angle fitting. Since the fitting was performed in three dimensions, each two dimensional projection are shown.

segment of typically $5\,\mu$m were determined by the fitting; they were obtained by the fitting with ten points which were picked up in the same way as the angle measurement and connected from the vertex to the end point of each track. Figure 4.10 shows a sample of the result of the range measurement.

If the range of track was larger than the window size of the image sensor, it was measured by moving the stage manually. The measurement error was evaluated by measuring the track several times. If the track passed across several sheets, the range was estimated in each sheet and summed. The range in materials except for the emulsion layer (*e.g.* polystyrene base, SSD, etc) was converted to that in the emulsion by considering energy loss ratio. The shrinkage factor and the density of the sheets which did not include the Ξ^- stopping point were regarded as the same value of the measured one. These differences are negligible because the range straggling effect (Section 4.5.2) is dominant for the long track,

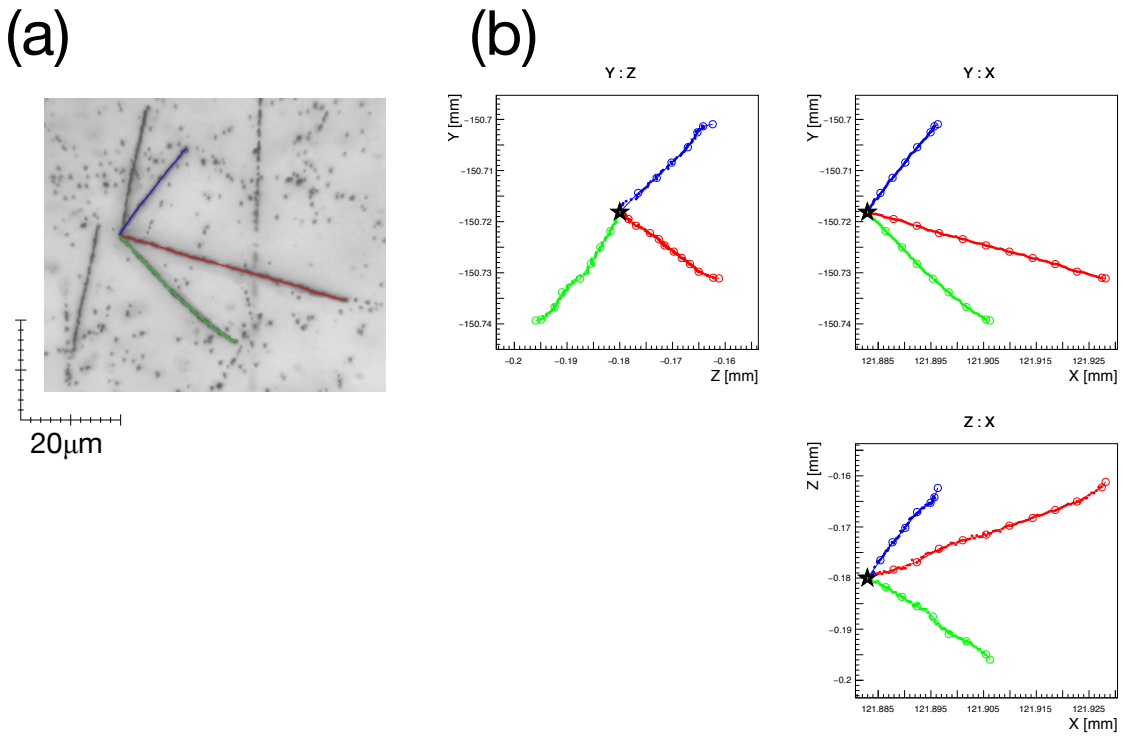

Figure 4.10: The typical result of the range measurement of an α decay event. (a) Fitting result is shown on each track with colored lines. (b) A result of the range measurement by the fitting. Each track is divided into 5 μm short segments (open colored circle) to measure the bent tracks. Each short rack is obtained by fitting ten points (close colored circle) which are picked up from the track like the angle measurement.

4.5 Energy calculation

4.5.1 Range-energy formula

The kinetic energy of a charged particle was obtained by the following range-energy formula given by Barkas *et al.*, [49, 50].

$$R = \rho \left(\frac{M}{Z^2} \cdot \lambda(\beta) + R_{ext} \right), \tag{4.2}$$

where R, Z, and M are the parameters of range, charge, and mass of a particle in the unit of the proton mass, respectively. The parameter of ρ, usually unity, denotes a factor to convert the range in our emulsion to the equivalent range in the standard emulsion (Ilford G5 emulsion with the density of $3.815\,\mathrm{g/cm^3}$). R_{ext} means a range extension caused by electron capture for positive charged ions.

$$R_{ext} = MZ^{2/3}C_z(\beta/Z), \tag{4.3}$$

$$\frac{\lambda_s}{\lambda} = \frac{rd-1}{rd_s-1} + \frac{r(d_s-d)}{rd_s-1} \cdot \frac{\lambda_s}{\lambda_w}, \tag{4.4}$$

C_Z is a phenomenological function of β/Z. $\lambda(\beta)$ represents a range of a proton at the velocity of β. λ_s and λ_w are ranges in the standard emulsion and water, respectively. The parameter d is a density of our emulsion which is determined by the range-energy calibration (Sec. 4.6). The factor r is the increasing ratio of emulsion volume to the mass of added water, which has the unit of $\mathrm{cm^3/g}$. The value of r was measured as 0.884 for our emulsion.

4.5.2 Range straggling

Even if the energies of charged particles are monochromatic, their ranges vary due to a range straggling effect. The range straggling, ΔR, was calculated in the following formula

$$\Delta R(T) = \frac{\sqrt{M}}{Z^2} \cdot \Delta R_p \left(\frac{T}{M} \right), \tag{4.5}$$

where Z, M, and T represent charge, mass in units of the proton mass, and kinetic energy of the particle, respectively. A parameter ΔR_p denotes the range straggling of proton, which is calculated as

$$(\Delta R_p(T))^2 = 4\pi n_e Z^2 e^4 \int_0^T \frac{(1-\beta^2/2)}{(1-\beta^2)\langle dE/dR \rangle^3} dE, \tag{4.6}$$

where n_e, $\langle dE/dR \rangle$, and e represent the electron density in the stopping material, the mean rate of energy loss, and the elementary charge, respectively. The range straggling was taken into account for the ambiguity of measured ranges in the kinematic analysis.

4.6 Measurement of density and shrinkage factor of emulsion

For kinematic analysis, range-energy calibration was performed by α tracks with a monochromatic energy of 8.784 MeV from a decay of ^{212}Po contaminated in an emulsion to determine its density. The α tracks in the thorium series isotopes can be easily identified because it has the largest kinetic energy, *i.e.*, longest range, in five α tracks as shown in Fig. 4.6 (a). Isotopes in the thorium series are shown in Fig. 4.11 [51–56]. The events with α decay chain were searched for around the event by using the Overall scanning method [57]. Since the emulsion layers were shrunk along the beam direction due to the photographic development, the shrinkage factor of the layer was measured by the α particles. Therefore, the ranges of related particles before development were obtained by multiplying the shrinkage factor. The shrinkage factor and the average range of the α track were obtained as follows.

As described in section 4.4, range of tracks was divided into short segments. Range of track before shrink can be calculated in the following equation.

$$R(S) = \sum_{i=1}^{n} \sqrt{\Delta x_i^2 + \Delta y_i^2 + (S \cdot \Delta z_i)^2}, \tag{4.7}$$

where Δx_i, Δy_i, Δz_i represent the length of the i-th short segment in xyz coordinates without the shrinkage correction. Parameter S is the shrinkage factor. The mean range and the shrinkage factor can be obtained to minimize a chi-square which is expressed as follows:

$$\chi^2/ndf = \frac{1}{N-2} \sum_{k=1}^{N} \left(\frac{(R - R_k(S))}{\sigma_k} \right)^2, \tag{4.8}$$

where a parameter R represents the range of the α track. Resolution of track measurement is expressed as σ which varies depending on zenith angle of the track. By the measurement of 102 α tracks, the mean range and the shrinkage factor were obtained to be $50.77 \pm 0.12\,\mu$m and 1.98 ± 0.02 for the 7th sheet of the 69th module in which the MINO event was observed (Fig. 4.12). From this result and the range-energy formula (Eq. 4.2-4.4), the density of the emulsion sheet was determined to be $3.486 \pm 0.013\,\mathrm{g/cm^3}$.

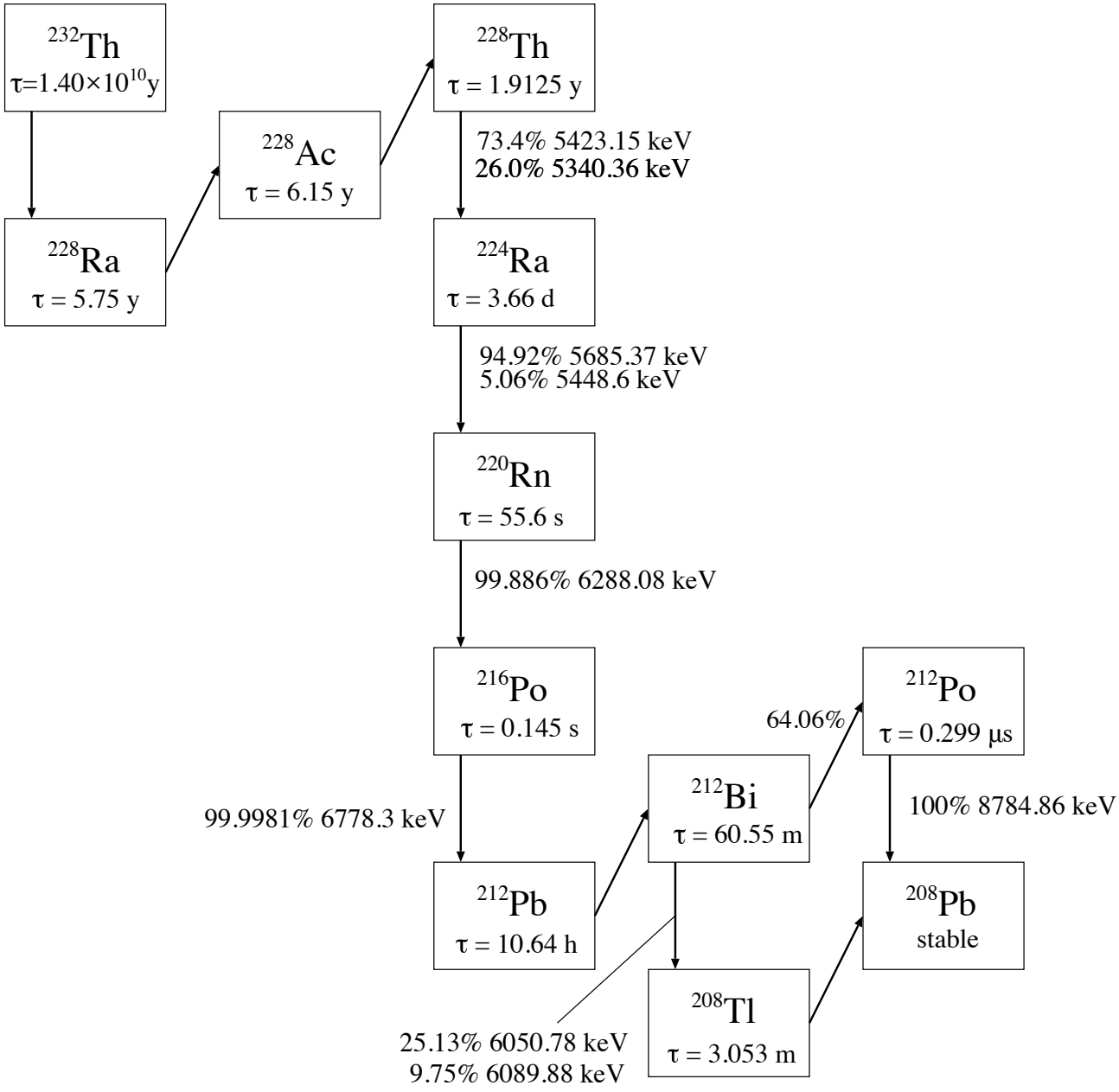

Figure 4.11: Thorium series.

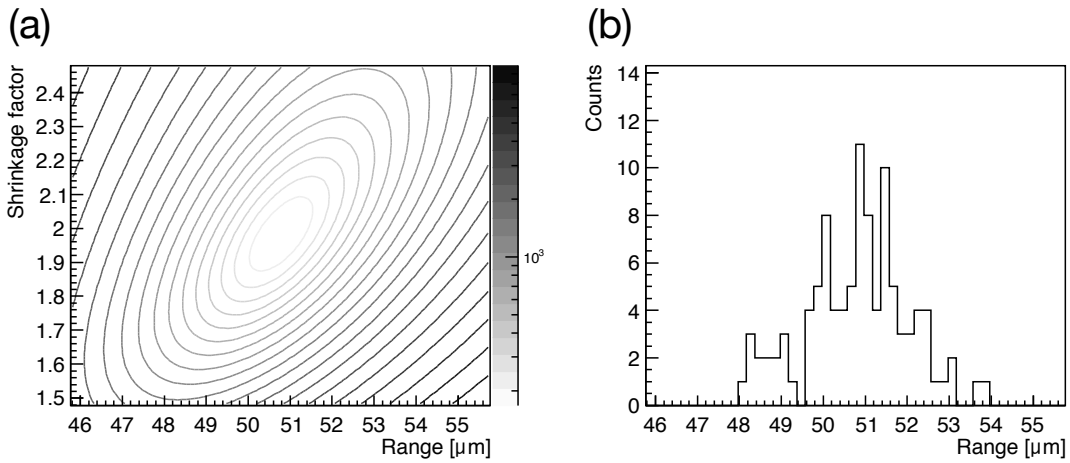

Figure 4.12: Result of the α track calibration for the emulsion layer in which the MINO event was observed. (a) χ^2 distribution in different values of parameters R and S. (b) The distribution of α track range with the optimum shrinkage factor.

Chapter 5

Interpretation of the MINO event and discussion

5.1 MINO event

A new double-Λ hypernuclear event was observed in the seventh sheet of the 69th module in the beam exposure. The momentum and reconstructed mass of the tagged K^+ in this event were $1.27\,\mathrm{GeV}/c$ and $0.54\,\mathrm{GeV}/c^2$, respectively. An overlaid photograph and a schematic drawing of the event are shown in Fig. 5.1. We named this event "MINO"[1].

The Ξ^- hyperon came to rest at vertex A, from which three charged particles (#1, #3, and #4) were emitted. The particle of track #1 decayed to three charged particles (#2, #5, and #6) at vertex B. The particle of track #2 decayed again to three charged particles (#7, #8, and #9) at vertex C. Measured ranges and angles of the tracks are summarized in Table 5.1. If the Ξ^- hyperon was captured by a heavy nucleus such as Ag or Br, a short track like #3 with a range of less than $32\,\mu$m could not be emitted due to the Coulomb barrier [26]. Therefore, we have concluded that the Ξ^- hyperon was captured by a light nucleus such as ^{12}C, ^{14}N, or ^{16}O. The particles of tracks #6 and #9 escaped from the module into the downstream SSD after passing several emulsion sheets. These tracks could be connected to the SSD by extrapolating the tracks at the exit point from the last emulsion sheet. The particle of track #6 was recorded in all layers of the SSD2 with large energy posit. Among them, the last layer had smaller energy deposit and smaller clustering size from the viewpoint of track angles. Therefore, the particle of track #6 was found to be stopped in the last layer. On the other hand, the particle of track #9 was observed by all layers of the SSD2 with similar energy deposits. Then, the particle of track #9 was considered to penetrate all layers of the SSD2. The ranges of #6 and #9 in the SSD were $4500 \pm 200\,\mu$m and $2200 \pm 20\,\mu$m in emulsion equivalent, respectively.

[1]The name of the southern part of Gifu prefecture, Japan, where the event was found.

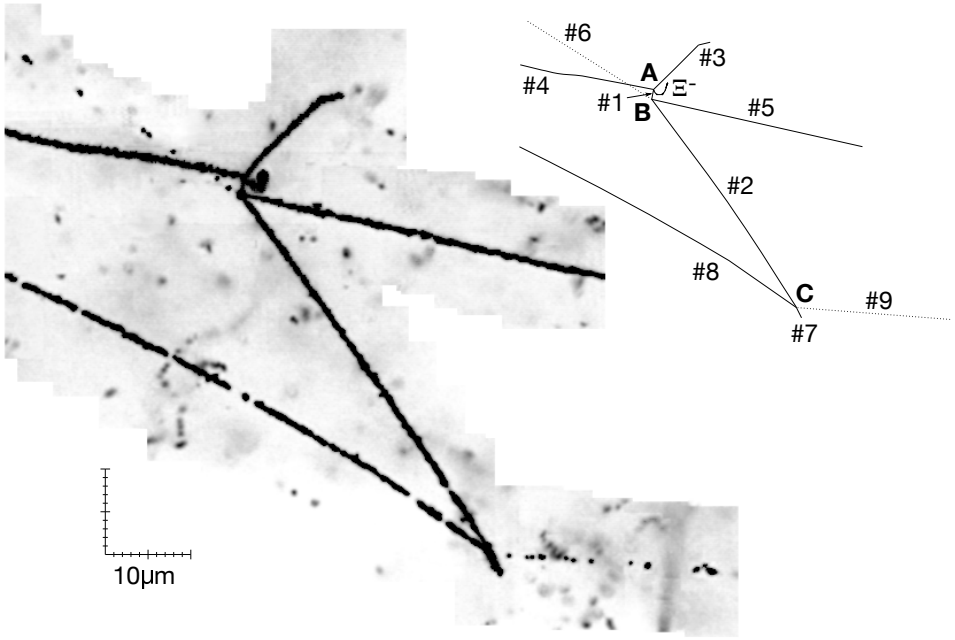

Figure 5.1: A photograph of the MINO event and its schematic drawing. The overlaid photograph is produced by connecting focused regions. Tracks #4, #5, #6, #8, and #9 are not fully shown in this photograph because these tracks are too long in this view scale.

Table 5.1: Measured ranges and angles of the tracks in the MINO event. The zenith and azimuthal angles are presented in columns θ and ϕ, respectively.

Vertex	Track ID	Range [μm]	θ [degree]	ϕ [degree]	Comment
A	#1	2.1 ± 0.2	83.7 ± 8.9	256.1 ± 5.3	double-Λ hypernucleus
	#3	17.5 ± 0.2	121.9 ± 1.9	48.2 ± 1.3	
	#4	65.7 ± 0.5	41.7 ± 1.7	166.7 ± 2.1	
B	#2	50.6 ± 0.3	90.2 ± 2.0	306.3 ± 1.3	single-Λ hypernucleus
	#5	122.1 ± 0.2	61.4 ± 1.8	347.0 ± 1.5	
	#6	>23170	106.2 ± 0.6	147.7 ± 0.4	stopped in the SSD
C	#7	5.0 ± 0.2	31.1 ± 2.8	297.0 ± 4.0	
	#8	116.7 ± 0.2	100.3 ± 1.9	144.2 ± 1.3	
	#9	>7378	147.4 ± 0.3	355.7 ± 0.5	passed through the SSD

5.2 Event interpretation

5.2.1 Criteria to estimate the optimum interpretation

For the observed decay event, all the assumptions were examined by taking all possible combinations of nuclide for the parent and daughter particles in each vertex by requiring the following criteria:

(1) consistency in the charge and the mass number and the strangeness

(2) conservations of energy and momentum

Therefore, we prepared a list of masses of nuclides based on the past measurements to cover possible daughter particles from initial states of ^{12}C, ^{14}N, or $^{16}\mathrm{O} + \Xi^-$. Masses of single-Λ hypernuclei are also listed which were obtained in the past experiments. There are several single-Λ hypernuclei of which mass is not measured. For these, we estimated the mass from extrapolation in isotopes. Then, we calculated the masses of double-Λ hypernuclei by regarding the $\Lambda\Lambda$ bonding energy, $B_{\Lambda\Lambda}({}^{A}_{\Lambda\Lambda}Z)$, as twice of $B_{\Lambda}({}^{A-1}_{\Lambda}Z)$. The masses of nuclides we prepared are listed in Appendix B.

(1) consistency in the charge and the mass number and the strangeness

The total charge (Z) and the mass number (A) should be conserved between the parent and daughter particles. If violated, such candidates were rejected. The strangeness (S) of a particle could be assigned from the decay topology.

(2) conservations of energy and momentum

Since the running time of hypernucleus before stopping in an emulsion is shorter than the decay life time, the hyperfragment decays after stopping in an emulsion. Thus, the total momentum of decay daughters should be zero. The kinetic energies of decay daughters can be obtained from their masses, charges, and ranges as described in Sec. 4.5.1. Therefore, conservation of energy and momentum can be examined from the ranges and angles obtained in the range measurement. The straggling effect was taken into account for range errors. If the conservations were not consistent within $3\,\sigma$, such candidates were discarded.

In case of neutral particles such as Λ, n, π^0 emitted from a decay vertex, their tracks were invisible. Therefore, the possibility of neutral particles emission was evaluated with the missing momentum for neutral particles. In the case that more than one neutral particle were emitted, they are treated as having the same velocity. In such a condition, the total kinetic energy of daughters become the minimum.

5.2.2 The kinematic fitting

After examining the above criteria (1)(2), the kinematic fitting is applied to each candidate [58]. This is based on the Lagrange multipliers method. Constraints are expressed as follows:

$$\boldsymbol{H}(\boldsymbol{\alpha},\boldsymbol{\beta}) = 0, \tag{5.1}$$
$$\begin{cases} H_1 = \sum_{i=1}^{n} \sqrt{m_i^2 + p_i^2} - m_0, \\ H_2 = \sum_{i=1}^{n} p_i \sin\theta_i \cos\phi_i, \\ H_3 = \sum_{i=1}^{n} p_i \sin\theta_i \sin\phi_i, \\ H_4 = \sum_{i=1}^{n} p_i \cos\theta_i, \end{cases}$$

where, m, p, θ, and ϕ represent mass, momentum, zenith angle, and azimuthal angle, respectively. The subscript 0 corresponds to the parent nuclide and the others show i-th daughter nuclide. The known parameters (*e.g.* p_i, θ_i, ϕ_i) and unknown variables (*e.g.* a mass of double hypernuclei, a momentum of the particle which escaped from the emulsion) are denoted as $\boldsymbol{\alpha}$ and $\boldsymbol{\beta}$, respectively. Both of them are expressed as the vector with the length of a and b. The parameter b should be less than or equal to the number of constrains which is four in this case. Equation 5.1 constraints the conservations of the energy and the momentum at the decay event. Then, the linearized equations can be obtained as follows by expanding around a convenient point ($\boldsymbol{\alpha_A}$, $\boldsymbol{\beta_A}$):

$$\boldsymbol{0} = \frac{\partial \boldsymbol{H}}{\partial \boldsymbol{\alpha}}|_{\boldsymbol{\alpha_A},\boldsymbol{\beta_A}}(\boldsymbol{\alpha} - \boldsymbol{\alpha_A}) + \frac{\partial \boldsymbol{H}}{\partial \boldsymbol{\beta}}|_{\boldsymbol{\alpha_A},\boldsymbol{\beta_A}}(\boldsymbol{\beta} - \boldsymbol{\beta_A}) + \boldsymbol{H}(\boldsymbol{\alpha_A},\boldsymbol{\beta_A}) \equiv \boldsymbol{D\eta} + \boldsymbol{Ez} + \boldsymbol{d}, \tag{5.2}$$

$$D_{i,j} = \frac{\partial H_i}{\partial \alpha_j}|_{\boldsymbol{\alpha_A},\boldsymbol{\beta_A}},$$
$$E_{i,j} = \frac{\partial H_i}{\partial \beta_j}|_{\boldsymbol{\alpha_A},\boldsymbol{\beta_A}},$$
$$d_i = H_i(\boldsymbol{\alpha_A},\boldsymbol{\beta_A}),$$

where, the size of $\boldsymbol{D}$ and $\boldsymbol{E}$ are the $4 \times a$ and $4 \times b$, respectively. Then, the χ^2 can be defined as follows:

$$\chi^2 = (\boldsymbol{\eta} - \boldsymbol{\eta_0})^t \boldsymbol{V}_{\eta_0}^{-1} (\boldsymbol{\eta} - \boldsymbol{\eta_0}) + 2\boldsymbol{\lambda}^t (\boldsymbol{D\eta} + \boldsymbol{Ez} + \boldsymbol{d}), \tag{5.3}$$
$$\boldsymbol{\eta_0} = \boldsymbol{\alpha_0} - \boldsymbol{\alpha_A},$$
$$\boldsymbol{V}_{\eta_0} = \begin{pmatrix} \sigma_1^2 & 0 & \cdots & 0 \\ 0 & \sigma_2^2 & \cdots & 0 \\ \vdots & \vdots & \ddots & \vdots \\ 0 & 0 & \cdots & \sigma_a^2, \end{pmatrix},$$

where, the $\boldsymbol{\alpha_0}$ indicates the initial parameters, which are the measured values. The measurement errors are expressed as σ_i. The $\boldsymbol{\lambda}$ represents the Lagrange multipliers. The parameters $\boldsymbol{\alpha}$ and $\boldsymbol{\beta}$ can be obtained to minimize the chi-square value (See Appendix C). The degree of freedom (DOF) of this fitting is $4 - b$.

5.2.3 Calculation of the ΛΛ binding energy

From the above kinematic fitting at production or decay vertex of a double-Λ hypernucleus, the mass of the double-Λ hypernucleus, $M({}^{A}_{\Lambda\Lambda}Z)$, can be determined. Then, the values of $B_{\Lambda\Lambda}$ and $\Delta B_{\Lambda\Lambda}$ are obtained as follows:

$$B_{\Lambda\Lambda}({}^{A}_{\Lambda\Lambda}Z) = M({}^{A-2}Z) + 2M(\Lambda) - M({}^{A}_{\Lambda\Lambda}Z), \tag{5.4}$$

$$\Delta B_{\Lambda\Lambda}({}^{A}_{\Lambda\Lambda}Z) = B_{\Lambda\Lambda}({}^{A}_{\Lambda\Lambda}Z) - 2B_{\Lambda}({}^{A-1}_{\Lambda}Z), \tag{5.5}$$

where, the B_Λ is the Λ binding energy of a single hypernucleus. It should be noted that, at the production vertex, the $B_{\Lambda\Lambda}$ and $\Delta B_{\Lambda\Lambda}$ values depend on the Ξ^- binding energy, B_{Ξ^-}, which is defined as:

$$B_{\Xi^-} = M(A) + M(\Xi^-) - M(A + \Xi^-), \tag{5.6}$$

where, A represents a nucleus and $M(A+\Xi^-)$ is the mass of an atomic bound system of Ξ^- and the nucleus. Therefore, the values of $B_{\Lambda\Lambda} - B_{\Xi^-}$ ($\Delta B_{\Lambda\Lambda} - B_{\Xi^-}$) were obtained.

5.2.4 Interpretation of the MINO event

Vertex C

First, we focus on the vertex C. Three charged particles were emitted with a coplanarity of 0.001 ± 0.043. The coplanarity is defined as $(\overrightarrow{r_1} \times \overrightarrow{r_2}) \cdot \overrightarrow{r_3}$, where $\overrightarrow{r_i}$ is a unit vector of a track angle. It indicates that three particles were emitted in a plane; thus, neutron emission is unlikely. The possibility of neutron emission is discussed in the end of this section. From all nuclide combinations for both mesonic and non-mesonic decays of known single-Λ hypernuclei, possible decay modes were selected using the following criteria. (1) An angular difference between track #9 and the momentum sum of track #7 and #8 should be back-to-back with $3\,\sigma$ confidence. (2) Momenta and energies should be conserved with $3\,\sigma$ by applying the kinematic fitting with the DOF of 3. Here, the range of #9 was parameterized to conserve the total momentum and reconstruct the mass of a single-Λ hypernucleus. Possible decay modes at vertex C are listed in Table 5.2. When the χ^2 value of the kinematic fitting was larger than 14.2, such decay modes were rejected. In this fitting case, such setting corresponds to a p-value of 0.27%, *i.e.*, $3\,\sigma$ cut condition. Taking this into account, the possible candidate of #2 was identified to be ${}^{5}_{\Lambda}$He in the case of no neutron emission. The lower limit of the range of #9 was obtained to be 7378 (in emulsion) + 2200 (in SSD) μm considering the track length in the SSD. The interpretation of ${}^{5}_{\Lambda}$He is consistent with this requirement.

Vertex B

Next, we checked vertex B. The particle of track #1 decayed to three charged particles including a very thin track (#6). The range of #6 was measured to be 23170 (in the emulsion) + 4500 (in the SSD) μm. If the particle of track #6 is π^-, the total visible energy by decay daughters (#2, #5, and #6) is at least 47.7 MeV. Since this energy is larger than the Q value of any π^- mesonic decay mode, it is impossible that the track #6

Table 5.2: Possible decay modes at vertex C in the case of no neutron emission. Candidates which are accepted by the angular constraint and the conservation of momentum and energy in $3\,\sigma$ cut condition are listed. The χ^2 value and the total range of #9 were obtained from the kinematic fitting.

Single-Λ hypernucleus (#2)		#7	#8	#9	χ^2	Range (#9) [μm]	Comment
${}^{4}_{\Lambda}$He	$\rightarrow$	^{3}He	p	π^-	33.1	16800	rejected
${}^{5}_{\Lambda}$He	$\rightarrow$	^{4}He	p	π^-	5.23	16270	
${}^{8}_{\Lambda}$Li	$\rightarrow$	^{6}Li	d	π^-	93.6	7906	rejected
${}^{9}_{\Lambda}$Li	$\rightarrow$	^{7}Li	d	π^-	105	10660	rejected

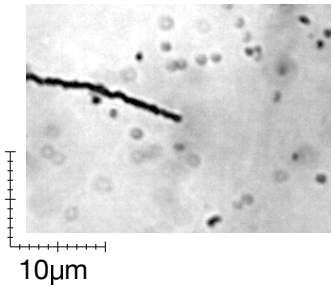

Figure 5.2: A photograph of the end point of track #5.

is π^-. Thus, the charge of #1 should be more than $3\,e$. The maximum allowed charge of #1 is $5\,e$ by assuming Ξ^- was captured in ^{16}O because three charged particles were emitted at vertex A. Therefore, the nuclide of #1 is determined to be ${}_{\Lambda\Lambda}$Be or ${}_{\Lambda\Lambda}$B.

The coplanarity of vertex B was calculated to be 0.007 ± 0.019. Among the decay modes with ${}^{5}_{\Lambda}$He as particle #2 without neutron emission, only the following decay mode satisfied the kinematic consistency.

$$ {}^{13}_{\Lambda\Lambda}\mathrm{B} \rightarrow {}^{5}_{\Lambda}\mathrm{He} + {}^{6}\mathrm{He} + d. $$

However, this decay mode was rejected because there was no electron track associated with the end point of track #5 as seen in Fig. 5.2. If it is ^{6}He, it should decay to ^{6}Li$+e^-+\overline{\nu}$ with a half-life of 806.7 ms [59]. Thus, neutron(s) should be emitted at vertex B although the coplanarity is so small. Regarding the decay modes with neutron(s) at vertex B, all nuclide combinations were examined for charged particles. In the kinematic analysis, the range of #6 was calculated by assuming a double-Λ hypernucleus with $\Delta B_{\Lambda\Lambda} = 0$, where the missing momentum was carried by unobserved neutron(s). In the case of multiple neutron emissions, all neutrons were treated as having the same momentum. This setting gives the minimum kinetic energy of neutrons and the maximum kinetic energy of #6, which corresponds to the maximum range of #6. If the maximum range was not consistent with the measurement, such assignment was rejected. Since non-mesonic decays have large Q values, many decay modes remained for the case of #1 being ${}_{\Lambda\Lambda}$Be or ${}_{\Lambda\Lambda}$B nuclides as summarized in Table 5.3.

Table 5.3: Possible decay modes at vertex B.

Double-Λ hypernucleus (#1)		#2	#5	#6	
${}^{9}_{\Lambda\Lambda}$Be	→	${}^{5}_{\Lambda}$He	p	p	$2n$
${}^{10}_{\Lambda\Lambda}$Be	→	${}^{5}_{\Lambda}$He	(p,d)	p	$(3n,2n)$
${}^{11}_{\Lambda\Lambda}$Be	→	${}^{5}_{\Lambda}$He	(p,d,t)	p	$(4n,3n,2n)$
${}^{12}_{\Lambda\Lambda}$Be	→	${}^{5}_{\Lambda}$He	(p,d,t)	p	$(5n,4n,3n)$
${}^{13}_{\Lambda\Lambda}$Be	→	${}^{5}_{\Lambda}$He	(p,d,t)	p	$(6n,5n,4n)$
${}^{11}_{\Lambda\Lambda}$B	→	${}^{5}_{\Lambda}$He	^{3}He	p	$2n$
${}^{12}_{\Lambda\Lambda}$B	→	${}^{5}_{\Lambda}$He	(^{3}He,^{4}He)	p	$(3n,2n)$
${}^{12}_{\Lambda\Lambda}$B	→	${}^{5}_{\Lambda}$He	^{4}He	d	n
${}^{13}_{\Lambda\Lambda}$B	→	${}^{5}_{\Lambda}$He	(^{3}He,^{4}He)	p	$(4n,3n)$
${}^{14}_{\Lambda\Lambda}$B	→	${}^{5}_{\Lambda}$He	^{4}He	p	$4n$
${}^{15}_{\Lambda\Lambda}$B	→	${}^{5}_{\Lambda}$He	^{4}He	p	$5n$

Vertex A

Finally, we analyzed vertex A, where three tracks were observed. All nuclide combinations making the track #1 to be ${}_{\Lambda\Lambda}$Be or ${}_{\Lambda\Lambda}$B were checked. In case of the decay with neutron emission, the momentum of neutron(s) was assumed to be the missing momentum. In the case of more than one neutron emission, only a lower limit of $\Delta B_{\Lambda\Lambda}$ could be obtained. Possible decay modes are listed in Table 5.4. Since the coplanarity of vertex A was calculated to be 0.000 ± 0.099, neutron emission was unlikely. However, even if neutron emit from a vertex, the coplanarity become consistent with zero with a probability of a few %. Then, we took account of the NAGARA event in which $\Delta B_{\Lambda\Lambda}$ was obtained to be 0.67 ± 0.17 MeV. From this result, $\Delta B_{\Lambda\Lambda} - B_{\Xi^-}$ should not be a large value. Therefore, candidates of decay modes at vertex A are (1), (2) and (3).

If the particle #1 decayed before stopping, its kinetic energy was larger than the estimation which was calculated from its range. In order to examine other possible decay modes, the kinematic fitting was performed by regarding the momentum of the particle #1 as a parameter. However, no other decay modes survived. Then, it was confirmed that particle #1 decayed after stopping.

Table 5.4: Possible decay modes at Vertex A. Error of $\Delta B_{\Lambda\Lambda}$ shows the result of the kinematic fitting derived from our measurement. Candidates which have $\Delta B_{\Lambda\Lambda} - B_{\Xi^-} < 20\,\mathrm{MeV}$ are listed.

Ξ^- capture		#1	#3	#4		$\Delta B_{\Lambda\Lambda} - B_{\Xi^-}$ [MeV]	
$^{16}\mathrm{O} + \Xi^-$	$\rightarrow$	$^{10}_{\Lambda\Lambda}\mathrm{Be}$	$^4\mathrm{He}$	t		1.40 ± 0.09	(1)
$^{16}\mathrm{O} + \Xi^-$	$\rightarrow$	$^{11}_{\Lambda\Lambda}\mathrm{Be}$	$^4\mathrm{He}$	d		1.64 ± 0.08	(2)
$^{16}\mathrm{O} + \Xi^-$	$\rightarrow$	$^{12}_{\Lambda\Lambda}\mathrm{Be}$	$^4\mathrm{He}$	p		-2.95 ± 0.08	(3)
$^{14}\mathrm{N} + \Xi^-$	$\rightarrow$	$^{10}_{\Lambda\Lambda}\mathrm{Be}$	p	p	$3n$	$>14.18 \pm 0.64$	
$^{14}\mathrm{N} + \Xi^-$	$\rightarrow$	$^{10}_{\Lambda\Lambda}\mathrm{Be}$	p	d	$2n$	$>15.94 \pm 1.22$	
$^{14}\mathrm{N} + \Xi^-$	$\rightarrow$	$^{10}_{\Lambda\Lambda}\mathrm{Be}$	d	p	$2n$	$>12.18 \pm 0.72$	
$^{14}\mathrm{N} + \Xi^-$	$\rightarrow$	$^{10}_{\Lambda\Lambda}\mathrm{Be}$	d	d	n	16.29 ± 1.92	
$^{14}\mathrm{N} + \Xi^-$	$\rightarrow$	$^{10}_{\Lambda\Lambda}\mathrm{Be}$	t	p	n	7.08 ± 1.05	
$^{14}\mathrm{N} + \Xi^-$	$\rightarrow$	$^{11}_{\Lambda\Lambda}\mathrm{Be}$	p	p	$2n$	$>10.60 \pm 0.93$	
$^{14}\mathrm{N} + \Xi^-$	$\rightarrow$	$^{11}_{\Lambda\Lambda}\mathrm{Be}$	p	d	n	17.43 ± 2.41	
$^{14}\mathrm{N} + \Xi^-$	$\rightarrow$	$^{11}_{\Lambda\Lambda}\mathrm{Be}$	d	p	n	10.30 ± 1.38	
$^{14}\mathrm{N} + \Xi^-$	$\rightarrow$	$^{12}_{\Lambda\Lambda}\mathrm{Be}$	p	p	n	10.21 ± 1.79	
$^{16}\mathrm{O} + \Xi^-$	$\rightarrow$	$^{10}_{\Lambda\Lambda}\mathrm{Be}$	$^4\mathrm{He}$	p	$2n$	$>9.35 \pm 0.47$	
$^{16}\mathrm{O} + \Xi^-$	$\rightarrow$	$^{10}_{\Lambda\Lambda}\mathrm{Be}$	$^4\mathrm{He}$	d	n	7.73 ± 0.40	
$^{16}\mathrm{O} + \Xi^-$	$\rightarrow$	$^{11}_{\Lambda\Lambda}\mathrm{Be}$	$^4\mathrm{He}$	p	n	4.42 ± 0.91	
$^{16}\mathrm{O} + \Xi^-$	$\rightarrow$	$^{12}_{\Lambda\Lambda}\mathrm{Be}$	$^3\mathrm{He}$	p	n	19.30 ± 0.82	
$^{16}\mathrm{O} + \Xi^-$	$\rightarrow$	$^{13}_{\Lambda\Lambda}\mathrm{B}$	p	p	$2n$	$>14.20 \pm 1.34$	
$^{16}\mathrm{O} + \Xi^-$	$\rightarrow$	$^{13}_{\Lambda\Lambda}\mathrm{B}$	d	p	n	16.55 ± 2.09	
$^{16}\mathrm{O} + \Xi^-$	$\rightarrow$	$^{14}_{\Lambda\Lambda}\mathrm{B}$	p	p	n	18.44 ± 2.65	

Table 5.5: Momenta and angles of the MINO event which were obtained by the kinematic fitting. Three interpretations is shown for vertex A. Vertex B is not shown because the number of possible decay modes is large.

Vertex	Track ID	Nuclide	Momentum [MeV/c]	θ [degree]	ϕ [degree]
A	#1	${}^{10}_{\Lambda\Lambda}$Be	134.1 ± 4.1	96.3 ± 2.1	266.0 ± 1.7
	#3	^{4}He	178.5 ± 0.9	121.1 ± 1.8	48.2 ± 1.3
	#4	t	148.3 ± 0.7	41.4 ± 1.6	164.9 ± 2.0
A	#1	${}^{11}_{\Lambda\Lambda}$Be	137.1 ± 3.6	86.5 ± 2.0	257.8 ± 1.5
	#3	^{4}He	178.4 ± 0.9	120.9 ± 1.8	48.7 ± 1.3
	#4	d	112.9 ± 0.6	41.8 ± 1.7	165.2 ± 2.0
A	#1	${}^{12}_{\Lambda\Lambda}$Be	140.6 ± 3.1	75.6 ± 1.8	248.3 ± 1.3
	#3	^{4}He	178.4 ± 0.9	120.6 ± 1.8	49.2 ± 1.3
	#4	p	70.3 ± 0.4	41.9 ± 1.7	165.7 ± 2.1
C	#7	^{4}He	104.7 ± 1.5	26.5 ± 0.9	291.3 ± 1.6
	#8	p	84.0 ± 0.4	99.3 ± 1.4	144.7 ± 1.2
	#9	π^-	95.4 ± 0.1	147.5 ± 0.3	355.7 ± 0.5

Summary of the interpretation

From the above considerations, candidates for production and decay modes are interpreted as follows:

$$\begin{aligned} {}^{16}\mathrm{O} + \Xi^- \rightarrow ({}^{10}_{\Lambda\Lambda}\mathrm{Be},\ {}^{11}_{\Lambda\Lambda}\mathrm{Be},\ {}^{12}_{\Lambda\Lambda}\mathrm{Be}) + {}^{4}\mathrm{He} + (t,\ d,\ p), \\ \hookrightarrow {}^{5}_{\Lambda}\mathrm{He} + (p, d, t) + p + xn, \\ \hookrightarrow {}^{4}\mathrm{He} + p + \pi^-. \end{aligned}$$

The nuclide of the double hypernucleus was uniquely identified as a ${}_{\Lambda\Lambda}$Be. The momenta and angles of each particle which were obtained by the kinematic fitting are shown in Table 5.5. The $B_{\Lambda\Lambda}$ and $\Delta B_{\Lambda\Lambda}$ values depend on the Ξ^- binding energy (B_{Ξ^-}). If we assume that the Ξ^- hyperon was captured in the atomic 3D state of ^{16}O with the theoretically estimated B_{Ξ^-} value of 0.23 MeV [29], $B_{\Lambda\Lambda}$ ($\Delta B_{\Lambda\Lambda}$) for each decay mode are obtained to be 15.05 ± 0.11 MeV (1.63 ± 0.14 MeV), 19.07 ± 0.11 MeV (1.87 ± 0.37 MeV), and 13.68 ± 0.11 MeV (-2.7 ± 1.0 MeV), for ${}^{10}_{\Lambda\Lambda}$Be, ${}^{11}_{\Lambda\Lambda}$Be, and ${}^{12}_{\Lambda\Lambda}$Be, respectively. These values are summarized in Table 5.6 together with their statistical and systematic errors. The statistical error was obtained from the kinematic fitting caused by the measurement error and the range straggling and the systematic error was caused by the mass of the Ξ^- hyperon and $B_\Lambda({}^{A-1}_{\Lambda}Z)$. The mass of the Ξ^- and Λ hyperon was taken as 1321.71 ± 0.07 MeV and 1115.683 ± 0.006 MeV, respectively [61].

In this analysis, we took 8.2 ± 0.5 MeV for $B_\Lambda({}^{11}_{\Lambda}\mathrm{Be})$ by linear extrapolation from B_Λ of ${}_{\Lambda}$Be isotopes with values of 5.16 ± 0.08 MeV (${}^{7}_{\Lambda}$Be) [60], 6.84 ± 0.05 MeV (${}^{8}_{\Lambda}$Be) [60], 6.71 ± 0.04 MeV (${}^{9}_{\Lambda}$Be) [60], and $8.60 \pm 0.07 \pm 0.16$ MeV (${}^{10}_{\Lambda}$Be) [62] because ${}^{11}_{\Lambda}$Be has not yet been observed. However, this simple extrapolation is not proper estimation because the difference of core structure affect the Λ binding energy. D. J. Millener, C. B. Dover, and A. Gal suggested the $B_\Lambda({}^{11}_{\Lambda}\mathrm{Be})$ of 10.46 MeV by adding 0.22 MeV to $B_\Lambda({}^{11}_{\Lambda}\mathrm{B})$ [63]. They took into account the charge difference between $B_\Lambda({}^{10}_{\Lambda}\mathrm{Be})$ and $B_\Lambda({}^{10}_{\Lambda}\mathrm{B})$ for this

Table 5.6: Result of $B_{\Lambda\Lambda}$ and $\Delta B_{\Lambda\Lambda}$ for MINO event. The statistical and systematic errors are shown. The Ξ^- hyperon was assumed to be captured in the atomic 3D state of ^{16}O ($B_{\Xi^-} = 0.23\,\mathrm{MeV}$).

Nuclide	$B_{\Lambda\Lambda}$ [MeV]	$\Delta B_{\Lambda\Lambda}$ [MeV]	$B_\Lambda(^{A-1}_{\Lambda}Z)$ [MeV]
$^{10}_{\Lambda\Lambda}$Be	$15.05 \pm 0.09 \pm 0.07$	$1.63 \pm 0.09 \pm 0.11$	6.71 ± 0.04 [60]
$^{11}_{\Lambda\Lambda}$Be	$19.07 \pm 0.08 \pm 0.07$	$1.87 \pm 0.08 \pm 0.36$	$8.60 \pm 0.07 \pm 0.16$ [62]
$^{12}_{\Lambda\Lambda}$Be	$13.68 \pm 0.08 \pm 0.07$	$(-2.7 \pm 0.08 \pm 1.0)$	8.2 ± 0.5 (extrapolation)

Table 5.7: χ^2 and p-value of the kinematic fitting at vertex A.

Decay mode	χ^2	p-value [%]
$^{16}\mathrm{O} + \Xi^- \to {}^{10}_{\Lambda\Lambda}\mathrm{Be} + {}^4\mathrm{He} + t$	11.5	0.93
$^{16}\mathrm{O} + \Xi^- \to {}^{11}_{\Lambda\Lambda}\mathrm{Be} + {}^4\mathrm{He} + d$	7.28	6.35
$^{16}\mathrm{O} + \Xi^- \to {}^{12}_{\Lambda\Lambda}\mathrm{Be} + {}^4\mathrm{He} + p$	11.3	1.02

calculation. In this case the $\Delta B_{\Lambda\Lambda}(^{12}_{\Lambda\Lambda}\mathrm{Be})$ is $-7.2\,\mathrm{MeV}$. The interpretation of $^{12}_{\Lambda\Lambda}$Be have such a systematic uncertainty.

Double-Λ hypernucleus can be generated as an excited state. In such a case, $\Delta B_{\Lambda\Lambda}$ of a ground state is increased by its excited energy to compensate the energy conservation. Since the mass of the double-Λ hypernucleus could not be measured at the vertex B in this event, it was determined by the vertex A only. Then, excited states of the double-Λ hypernucleus should be taken into account.

The probabilities of the three interpretations were evaluated with the chi-square value of the kinematic fitting with DOF of 3. Chi-square and p-value for these three decay modes are summarized in Table 5.7. It is found that the most probable interpretation of this event is $^{11}_{\Lambda\Lambda}$Be from the chi-square values.

In the above analysis, it is assumed that no neutron was emitted at vertex C. The interpretation at vertex C is important because the analysis of vertex B is not effective in selecting possible candidates from the kinematics due to the large Q values of non-mesonic decays. If we assume neutron emission, the following decay modes are also accepted.

$$^3_{\Lambda}\mathrm{H} \to p + p + \pi^- + n, \quad \text{(i)}$$

$$^4_{\Lambda}\mathrm{H} \to d + p + \pi^- + n. \quad \text{(ii)}$$

In these cases, interpretations of $_{\Lambda\Lambda}$Li nuclides for the track #1 in vertex A also remain. However, this possibility is very unlikely: The branching ratio of $^3_{\Lambda}$H and $^4_{\Lambda}$H decays were measured in a past experiment [64]. Among about 2000 $^3_{\Lambda}$H and $^4_{\Lambda}$H decays, less than 30 instances of decay mode (i) and 5 of (ii) have been observed. A theoretical calculation also supports this small possibility *e.g.,* 0.6% for decay mode (i) [65].

5.3 Discussion

The newly observed double-Λ hypernuclear event is interpreted as the production and decay of either $^{10}_{\Lambda\Lambda}$Be, $^{11}_{\Lambda\Lambda}$Be, or $^{12}_{\Lambda\Lambda}$Be nucleus. The present result was compared with the

Table 5.8: Summary of ${}_{\Lambda\Lambda}$Be double-Λ hypernuclei observed in past experiments. Multiple interpretations are listed in MIKAGE, DEMACHIYANAGI, and HIDA events.

Event	Target	Nuclide	$B_{\Lambda\Lambda}$ [MeV]	$\Delta B_{\Lambda\Lambda}$ [MeV]	Comment
MIKAGE [28]	^{12}C	${}^{6}_{\Lambda\Lambda}$He	10.01 ± 1.71	3.77 ± 1.71	
	^{12}C	${}^{11}_{\Lambda\Lambda}$Be	22.15 ± 2.94	3.95 ± 3.00	
	^{14}N	${}^{11}_{\Lambda\Lambda}$Be	23.05 ± 2.59	4.85 ± 2.63	
DEMACHIYANAGI [28]	^{12}C	${}^{10}_{\Lambda\Lambda}$Be*	11.90 ± 0.13	-1.52 ± 0.15	most probable
	^{12}C	${}^{11}_{\Lambda\Lambda}$Be	$22.44^{+1.70}_{-1.09}$	$4.22^{+1.75}_{-1.18}$	
	^{14}N	${}^{13}_{\Lambda\Lambda}$B	$27.94^{+3.16}_{-2.02}$	$5.20^{+3.17}_{-2.03}$	
HIDA [28]	^{14}N	${}^{12}_{\Lambda\Lambda}$Be	22.48 ± 1.21		
	^{16}O	${}^{11}_{\Lambda\Lambda}$Be	20.83 ± 1.27	2.61 ± 1.34	
Danysz [30–32]	^{12}C	${}^{10}_{\Lambda\Lambda}$Be	14.7 ± 0.4	1.3 ± 0.4	consistent with the NAGARA

past measurements and theoretical calculations.

5.3.1 Candidates of ${}_{\Lambda\Lambda}$Be double-Λ hypernuclei in the past experiments

Candidates of ${}_{\Lambda\Lambda}$Be double-Λ hypernuclei which were observed in the past experiments are listed in Table 5.8. The MIKAGE, DEMACHIYANAGI, and HIDA events were observed in the KEK E373 experiment [28]. These events have several interpretations. In the case of the double-Λ hypernuclear event observed by Danysz [25], an interpretation consistent with the NAGARA event is shown [30–32].

The MIKAGE event can be interpreted in the three different ways as follows:

$$
\begin{aligned}
{}^{12}\mathrm{C} + \Xi^{-} &\rightarrow {}^{6}_{\Lambda\Lambda}\mathrm{He} + {}^{6}\mathrm{Li} + n, && (1)\\
&\hookrightarrow {}^{3}_{\Lambda}\mathrm{H} + p + 2n.\\
{}^{12}\mathrm{C} + \Xi^{-} &\rightarrow {}^{11}_{\Lambda\Lambda}\mathrm{Be} + p + n, && (2)\\
&\hookrightarrow {}^{9}_{\Lambda}\mathrm{Li} + p + n.\\
{}^{14}\mathrm{N} + \Xi^{-} &\rightarrow {}^{11}_{\Lambda\Lambda}\mathrm{Be} + {}^{3}\mathrm{He} + n, && (3)\\
&\hookrightarrow {}^{9}_{\Lambda}\mathrm{Li} + p + n.
\end{aligned}
$$

Two charged particles with a neutron were emitted from the point where the Ξ^{-} was captured by the nucleus. Then, one of them decayed to two charged particles and one of the daughter particle decayed to two particles in the mesonic mode. From the kinematic analysis of the decay vertex of single-Λ hypernucleus, its nuclide was identified to be ${}^{3}_{\Lambda}$H, ${}^{7}_{\Lambda}$He, or ${}^{9}_{\Lambda}$Li. Then, by combining the kinematic analysis of the production and decay vertices of the double-Λ hypernucleus, above three decay modes were turned out to be possible. The errors of $B_{\Lambda\Lambda}$ and $\Delta B_{\Lambda\Lambda}$ were large due to neutron(s) emission at the production vertex. Since the mesonic decay rate of a ${}^{9}_{\Lambda}$Li nucleus is not so large (about 20%), interpretation (1) was considered to be more likely.

The DEMACHIYANAGI event is possibly interpreted as the following decay modes:

$$^{12}\mathrm{C} + \Xi^- \rightarrow {}^{10}_{\Lambda\Lambda}\mathrm{Be} + t. \quad (1)$$
$$^{12}\mathrm{C} + \Xi^- \rightarrow {}^{11}_{\Lambda\Lambda}\mathrm{Be} + p + n. \quad (2)$$
$$^{14}\mathrm{N} + \Xi^- \rightarrow {}^{13}_{\Lambda\Lambda}\mathrm{B} + p + n. \quad (3)$$

Two charged particles were emitted in collinear topology from the Ξ^- capture position. Then, one of them decayed sequentially in the non-mesonic modes. The kinematic analysis was performed at production vertex of the double-Λ hypernucleus, then above three interpretation were accepted to be consistent with previous data. Since two particles were emitted back-to-back topology, interpretation (1) was considered to be the most probable one. The $B_{\Lambda\Lambda}$ and $\Delta B_{\Lambda\Lambda}$ values were obtained to be 11.90 ± 0.13 MeV and -1.52 ± 0.15 MeV, respectively. Since the $\Delta B_{\Lambda\Lambda}$ was negative contrary to the NAGARA result, this state is considered to be an excited state. In such a case, the $\Delta B_{\Lambda\Lambda}$ of ground state is increased by its excitation energy. A calculation by E. Hiyama *et al.* supports that the ${}^{10}_{\Lambda\Lambda}$Be was produced as a 2^+_1 state [33].

Two interpretations are possible for the HIDA event as follows:

$$^{14}\mathrm{N} + \Xi^- \rightarrow {}^{12}_{\Lambda\Lambda}\mathrm{Be} + p + p + n. \quad (1)$$
$$^{16}\mathrm{O} + \Xi^- \rightarrow {}^{11}_{\Lambda\Lambda}\mathrm{Be} + p + {}^{4}\mathrm{He} + n. \quad (2)$$

Three charged particles with neutron(s) were emitted after the Ξ^- was captured by a nucleus. Then, one of them decayed sequentially in the non-mesonic modes. Nuclide of double-Λ hypernucleus was identified to be ${}_{\Lambda\Lambda}$Be or ${}_{\Lambda\Lambda}$B from the charge conservation. The kinematic analysis was performed at the production vertex of the double-Λ hypernucleus, then the above two interpretations were accepted. Those errors were large due to neutron(s) emission.

The double-Λ hypernucleus observed by Danysz *et al.,* is considered to be ${}^{10}_{\Lambda\Lambda}$Be.

$$^{12}\mathrm{C} + \Xi^- \rightarrow {}^{10}_{\Lambda\Lambda}\mathrm{Be} + d + n,$$
$$\hookrightarrow {}^{9}_{\Lambda}\mathrm{Be}^* + p + \pi^-.$$

Two π^- mesons were emitted from two vertices derived from the Ξ^- capture. This event was originally considered to be the ${}^{10}_{\Lambda\Lambda}$Be or ${}^{11}_{\Lambda\Lambda}$Be with the $\Delta B_{\Lambda\Lambda}$ of 4.5 ± 0.4 MeV and 3.2 ± 0.6 MeV, respectively. However, after the observation of the NAGARA event this interpretation was re-examined by considering the excited state of the daughter single-Λ hypernucleus. Then, the above decay mode was accepted as reasonable with the $B_{\Lambda\Lambda}$ and $\Delta B_{\Lambda\Lambda}$ of 14.7 ± 0.4 MeV and 1.3 ± 0.4 MeV, respectively [32].

5.3.2 Theoretical calculation of ${}_{\Lambda\Lambda}$Be double-Λ hypernuclei

Several theoretical calculations were performed for ${}_{\Lambda\Lambda}$Be double hypernuclei. Results of these calculations are listed in Table 5.9.

E. Hiyama *et al.* calculated the energy states of ${}^{10}_{\Lambda\Lambda}$Be and ${}^{11}_{\Lambda\Lambda}$Be with the Gaussian expansion method [33]. They decomposed the double hypernuclei into three species of particles (α, Λ, and n) int the cluster models of $\alpha\alpha\Lambda\Lambda$ and $\alpha\alpha n\Lambda\Lambda$ for ${}^{10}_{\Lambda\Lambda}$Be and ${}^{11}_{\Lambda\Lambda}$Be,

Table 5.9: Results of calculation ${}_{\Lambda\Lambda}$Be double-Λ hypernuclei.

Author	Nuclide	$B_{\Lambda\Lambda}$ [MeV]
E. Hiyama *et al.* [33]	${}^{10}_{\Lambda\Lambda}$Be	14.74
	${}^{11}_{\Lambda\Lambda}$Be	18.23
A.Gal, D.J.Millener [66]	${}^{10}_{\Lambda\Lambda}$Be	14.97 $\pm$ 0.22
	${}^{11}_{\Lambda\Lambda}$Be	18.40 $\pm$ 0.28
	${}^{12}_{\Lambda\Lambda}$Be	20.72 $\pm$ 0.20
W.Y.Li *et al.* [67]	${}^{10}_{\Lambda\Lambda}$Be	15.00
Y. K.En'yo [68]	${}^{10}_{\Lambda\Lambda}$Be	14.80, 17.57, 13.64
	${}^{11}_{\Lambda\Lambda}$Be	17.22, 19.98, 16.00
	${}^{12}_{\Lambda\Lambda}$Be	18.74, 20.32, 18.04

respectively. Five kinds of bonding ($\Lambda-\Lambda$, $\Lambda-n$, $\Lambda-\alpha$, $\Lambda-\alpha$, $\alpha-\alpha$, and $\alpha-n$) are involved in the calculation. These interactions were determined to reproduce (i) Energies of the low-lying states and scattering phase shifts in the αn and $\alpha\alpha$ systems, (ii) Λ-binding energies B_Λ in ${}^{5}_{\Lambda}$He (=$\alpha\Lambda$), ${}^{6}_{\Lambda}$He (=$\alpha n\Lambda$), and ${}^{9}_{\Lambda}$Be (=$\alpha\alpha\Lambda$), (iii) double-Λ binding energies $B_{\Lambda\Lambda}$ in ${}^{6}_{\Lambda\Lambda}$He (=$\alpha\Lambda\Lambda$), *i.e.* the NAGARA event. The $\Lambda\Lambda$ interaction was tuned to reproduce the NAGARA event. There was no other adjustable parameter. Obtained values of $B_{\Lambda\Lambda}$ of 0^+ and 2^+ states were 14.74 MeV and 11.88 MeV, respectively. Those reproduced the binding energy of the Danysz's event (14.7 ± 0.4MeV) and the DEMACHIYANAGI event (11.9 ± 0.13MeV) well. In the case of the ${}^{11}_{\Lambda\Lambda}$Be, the $\Lambda\Lambda$ binding energy $B_{\Lambda\Lambda}$ was obtained to be 18.23 MeV for the $3/2^-$ ground state.

A shell model calculation was done by A. Gal and D. J. Millener [66]. They calculated the binding energies of p-shell double-Λ hypernuclei estimated by the following simple equation:

$$B^{SM}_{\Lambda\Lambda} = 2\overline{B}_\Lambda({}^{A-1}_{\Lambda}Z) + \langle V_{\Lambda\Lambda}\rangle_{SM},$$

where $\overline{B}_\Lambda({}^{A-1}_{\Lambda}Z)$ is separation energies of the $(2J+1)$-averaged g.s. doublet in single-Λ hypernuclei and $\langle V_{\Lambda\Lambda}\rangle_{SM} = 0.67 \pm 0.17$ MeV (NAGARA). The ΛN interaction was given by the several parameters which were determined with the observed γ ray in single-Λ hypernuclear experiment. They reproduced the $\Lambda\Lambda$ binding energies of observed ${}^{10}_{\Lambda\Lambda}$Be (DEMACHIYANAGI with the excited energy of 3.04 MeV) and ${}^{13}_{\Lambda\Lambda}$B (E176) well [26].

W. Y. Li *et al.* investigated properties of ^{8}Be, ${}^{9}_{\Lambda}$Be, and ${}^{10}_{\Lambda\Lambda}$Be by the beyond-mean-field Skyrme-Hartree-Fock model with the SLy4+SLL4 interaction, which is the up-to-date Skyrme-type $N\Lambda$ interaction. They described the energy spectrum of ${}^{9}_{\Lambda}$Be with a three-body cluster. However, obtained Λ binding energy, 7.29 MeV, was overestimated compared with the experimental value by about 0.5 MeV. They investigated ${}^{10}_{\Lambda\Lambda}$Be state as a test of the model calculation. The values of $B_{\Lambda\Lambda}$ were estimated to be 15.00 MeV and 12.49 MeV for 0^+ (g.s.) and 2^+ state, respectively. It should be noticed that the attractive $\Lambda\Lambda$ interaction, $\langle V_{\Lambda\Lambda}\rangle$, was not taken into account. Then, the double-$\Lambda\Lambda$ binding energy was obviously larger than the observed data if it was corrected by adding the $\langle V_{\Lambda\Lambda}\rangle$.

Y. K. En'yo calculated $0s$-orbit states in p-shell double-Λ hypernuclei by applying microscopic cluster models to core nuclear part and a potential model for Λ hyperon [68]. The $\Lambda\Lambda$ binding energy for ${}^{10}_{\Lambda\Lambda}$Be, ${}^{11}_{\Lambda\Lambda}$Be, ${}^{12}_{\Lambda\Lambda}$Be were obtained with three types of the

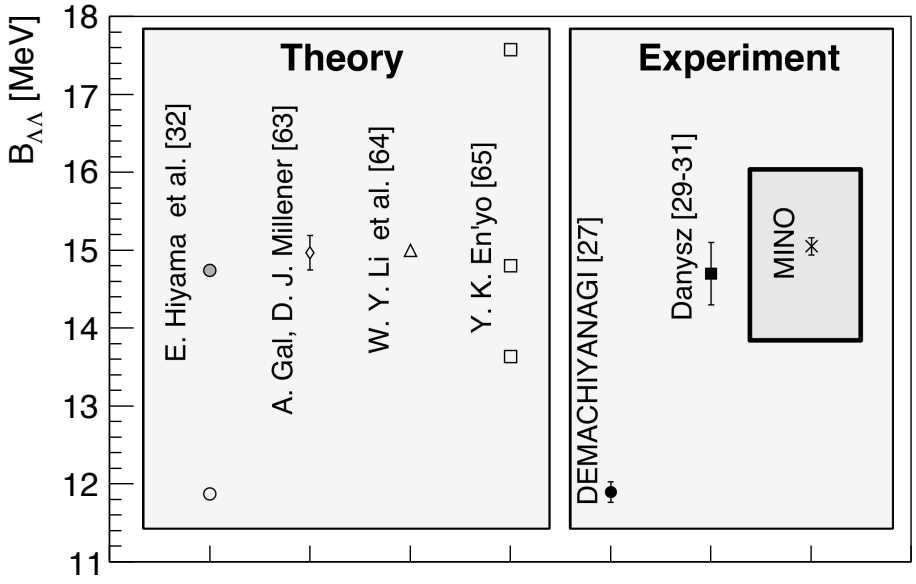

Figure 5.3: Comparison of $B_{\Lambda\Lambda}$ of ${}^{10}_{\Lambda\Lambda}$Be obtained in the theoretical calculations and in the past measurements. The excited state 2^+ (close circle) and the ground state 0^+ (open circle) are shown in the results of E. Hiyama *et al.*

parameter k_f, Fermi momentum of nuclear matter, *i.e.*, ESC08a(DI), ESC08a(Hyb), and ESC08a(DD). The parameter was tuned to reproduce the NAGARA event ($B_{\Lambda\Lambda} =$ 0.67MeV). ESC08a(Hyb) shows good agreement with the $\Lambda\Lambda$ binding energy of the DEMACHIYANAGI event and the B_Λ of single-Λ hypernuclei in $A \geq 12$.

5.3.3 Comparison of ${}_{\Lambda\Lambda}$Be double-Λ hypernuclei

${}^{10}_{\Lambda\Lambda}$Be double-Λ hypernucleus

The obtained $B_{\Lambda\Lambda}$ value for ${}^{10}_{\Lambda\Lambda}$Be in the present analysis is 15.05 ± 0.11 MeV. This is consistent with the DEMACHIYANAGI event ($B_{\Lambda\Lambda} = 11.9 \pm 0.13$) by considering the difference of the energy level of the ground state (0^+) and the excited state (2^+). Additionally, the double-Λ hypernucleus ${}^{10}_{\Lambda\Lambda}$Be with $B_{\Lambda\Lambda} = 14.7 \pm 0.4$ MeV observed by Danysz is also consistent with the present result [30–32]. Theoretical calculations also support this result; all theoretical results introduced in Sec. 5.3.2 are consistent with the present measurement within the errors. Therefore, it is reasonable to consider that ${}^{10}_{\Lambda\Lambda}$Be was produced in the ground state.

${}^{11}_{\Lambda\Lambda}$Be double-Λ hypernucleus

The present result of ${}^{11}_{\Lambda\Lambda}$Be interpretation ($B_{\Lambda\Lambda} = 19.07 \pm 0.11$ MeV) is consistent with the past results given by HIDA and MIKAGE events by considering their large er-

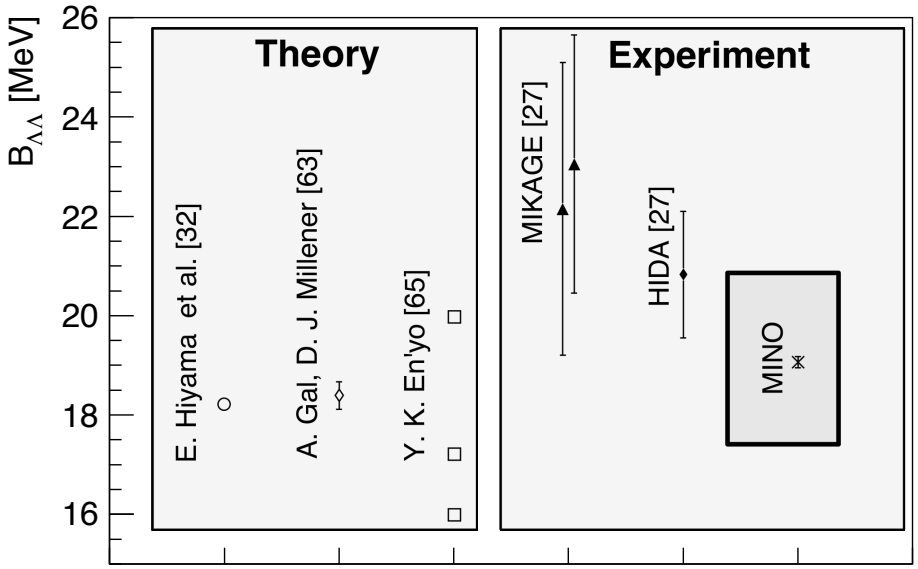

Figure 5.4: Comparison of $B_{\Lambda\Lambda}$ of ${}^{11}_{\Lambda\Lambda}$Be obtained by the theoretical calculations and the past experiments.

rors, in which $B_{\Lambda\Lambda}$ values were reported to be 22.15 ± 2.94 MeV, 23.05 ± 2.59 MeV, and 20.83 ± 1.27 MeV [28]. The present measurement has a much smaller error on $B_{\Lambda\Lambda}$ than the past events because no neutron was emitted at the production vertex of the double-Λ hypernucleus. E. Hiyama *et al.*, and A. Gal and D. J. Millener showed a similar results; $B_{\Lambda\Lambda}$ values were estimated to be 18.23 MeV and 18.40 ± 0.28 MeV, respectively. The difference between these calculations and the measured value is less than 1 MeV. However, the difference is large in statistical error. On the other hand, Y. K. En'yo reported a different value of 17.22 MeV based on ESC08a(Hyb). This is obviously inconsistent with the present result.

${}^{12}_{\Lambda\Lambda}$Be double-Λ hypernucleus

The present result of $B_{\Lambda\Lambda}$ for ${}^{12}_{\Lambda\Lambda}$Be interpretation is 13.68 ± 0.11 MeV. By assuming $B_{\Lambda}({}^{11}_{\Lambda}\mathrm{Be}) = 8.2 \pm 0.5$ MeV from the extrapolation, $\Delta B_{\Lambda\Lambda}$ becomes a negative value (-2.7 ± 1.0 MeV), which is not consistent with the past results. This result indicates that the ${}^{12}_{\Lambda\Lambda}$Be was generated in an excited state. The core nucleus, ^{10}Be, has excited states whose energies are in the range of 3.368 MeV to 6.263 MeV [69]. If the level of ${}^{12}_{\Lambda\Lambda}$Be is assumed to be that of ^{10}Be, $\Delta B_{\Lambda\Lambda}$ for the ground state of ${}^{12}_{\Lambda\Lambda}$Be can becomes positive. The HIDA event is interpreted in which the ${}^{12}_{\Lambda\Lambda}$Be is produced with the $B_{\Lambda\Lambda}$ of 22.48 ± 1.21 MeV. This value is much larger than the present result. In the theoretical calculation, $B_{\Lambda\Lambda}$ values of the ground state were obtained to be 20.72 ± 0.20 MeV [66] and 18.74 MeV [68]. If the ${}^{12}_{\Lambda\Lambda}$Be was generated with an excited energy of $5 - 7$MeV, the present result is consistent.

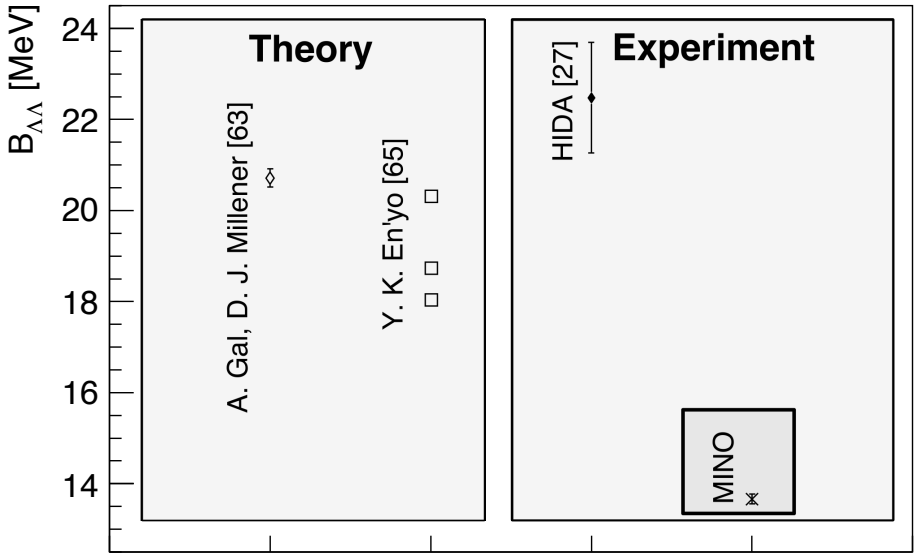

Figure 5.5: Comparison of $B_{\Lambda\Lambda}$ of ${}^{12}_{\Lambda\Lambda}$Be obtained by the theoretical calculations and the past experiments.

5.3.4 Mass dependence of the $\Lambda\Lambda$ bonding energy

Three interpretations, generations of ${}^{10}_{\Lambda\Lambda}$Be, ${}^{11}_{\Lambda\Lambda}$Be, and ${}^{12}_{\Lambda\Lambda}$Be*, are accepted from the above consideration. Among them, ${}^{11}_{\Lambda\Lambda}$Be is the most probable one from the analysis described in Sec. 5.2. In this scenario, the present $\Delta B_{\Lambda\Lambda}$ for ${}^{11}_{\Lambda\Lambda}$Be was obtained to be 1.87 ± 0.37 MeV. This value is larger than that for the NAGARA event; 0.67 ± 0.17 MeV. This difference may come from the difference of the core nuclear structure caused by ΛN interaction; for example the shrinkage of the core nucleus may affect the $\Delta B_{\Lambda\Lambda}$ value. This tendency is consistent with the calculations. However, the calculated value of $B_{\Lambda\Lambda}$ is different from the present result although the NAGARA and the DEMACHIYANAGI events are well reproduced [33, 66, 68]. Taking into account in the α-cluster model, the ${}^{11}_{\Lambda\Lambda}$Be core ^{9}Be can be expressed as $\alpha\alpha n$ (Fig. 5.6). This result suggests that there are other effects from the $\Lambda\Lambda$ and/or ΛN interaction which is caused by an additional neutron from ${}^{10}_{\Lambda\Lambda}$Be. This will be a hint to solve the interaction in many body system such as $n\Lambda\Lambda$ three-body interaction.

In order to perform a systematic study of the $\Lambda\Lambda$ binding energy, observation of new double-Λ hypernuclear species are necessary. In particular, $B_{\Lambda\Lambda}$ values for small p-shell double-Λ hypernuclei are considered to depend on the cluster structure strongly [68]. Therefore, experimental inputs help us to create a realistic model of the structure of double-Λ hypernuclei. Further, light s-shell double-Λ hypernuclei, ${}^{4}_{\Lambda\Lambda}$H, ${}^{5}_{\Lambda\Lambda}$H, and ${}^{5}_{\Lambda\Lambda}$He, are important to investigate the $\Lambda\Lambda$ interaction. Since the $\Lambda\Lambda - \Xi N$ conversion was not forbidden by the Pauli principle in these nuclei, the $\Lambda\Lambda - \Xi N$ coupling effect may enhance the $\Lambda\Lambda$ binding energy.

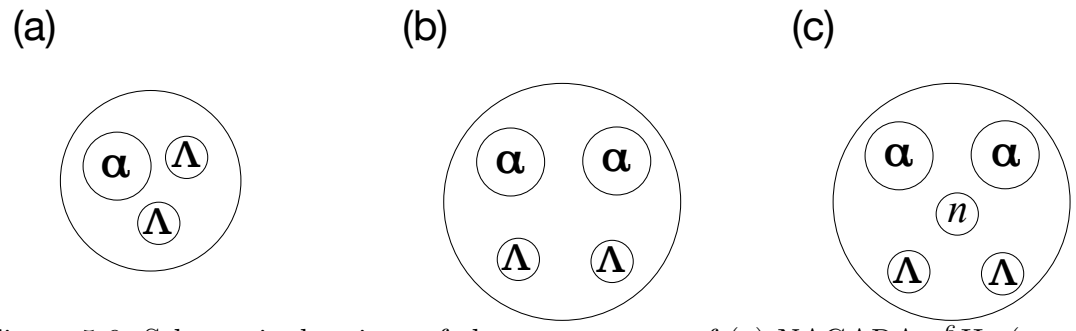

Figure 5.6: Schematic drawings of cluster structure of (a) NAGARA ${}^{6}_{\Lambda\Lambda}\mathrm{He}$ ($\alpha+\Lambda+\Lambda$), (b) DEMACHIYANAGI ${}^{10}_{\Lambda\Lambda}\mathrm{Be}$ ($\alpha+\alpha+\Lambda+\Lambda$), and (c) ${}^{11}_{\Lambda\Lambda}\mathrm{Be}$ ($\alpha+\alpha+n+\Lambda+\Lambda$).

The emulsion scanning of the J-PARC E07 experiment is still ongoing. The observed number of double strangeness events is about 30% of our goal so far. More double-Λ hypernuclei will be observed in the near future, which will give us new knowledge of the $\Lambda\Lambda$ interaction.

Chapter 6

Conclusion

Double-Λ hypernuclei have been investigated to understand the baryon-baryon interaction in $SU(3)_f$ symmetry. Hybrid emulsion experiments are effective to detect the sequential weak decays specific for the double-Λ hypernuclei.

The J-PARC E07 experiment was performed to accumulate more than 100 double strangeness events through the (K^-, K^+) reaction. The Ξ^-'s were produced from $^{12}\mathrm{C}(K^-, K^+)$ reaction and stopped in emulsions. Beam exposure of the E07 has been completed in 2017. A total of 118 modules produced from 2.1-tons emulsion gels were exposed to 1.13×10^{11} particles of the K^- beam. We have succeeded to detect an impressive new double-Λ hypernuclear event, "MINO". This event was uniquely identified to be a ${}_{\Lambda\Lambda}$Be hypernucleus production and decay by taking account of the NAGARA event. Possible interpretations are

$$
\begin{aligned}
{}^{16}\mathrm{O} + \Xi^- \rightarrow ({}^{10}_{\Lambda\Lambda}\mathrm{Be},\ {}^{11}_{\Lambda\Lambda}\mathrm{Be},\ {}^{12}_{\Lambda\Lambda}\mathrm{Be}) + {}^{4}\mathrm{He} + (t,\ d,\ p),\\
\hookrightarrow {}^{5}_{\Lambda}\mathrm{He} + (p, d, t) + p + xn,\\
\hookrightarrow {}^{4}\mathrm{He} + p + \pi^-.
\end{aligned}
$$

$B_{\Lambda\Lambda}$ ($\Delta B_{\Lambda\Lambda}$) of three double-Λ hypernuclei , ${}^{10}_{\Lambda\Lambda}$Be, ${}^{11}_{\Lambda\Lambda}$Be and ${}^{12}_{\Lambda\Lambda}$Be, were obtained to be 15.05 ± 0.11 MeV (1.63 ± 0.14 MeV), 19.07 ± 0.11 MeV (1.87 ± 0.37 MeV), and 13.68 ± 0.11 MeV (-2.7 ± 1.0 MeV), respectively, by assuming the Ξ^- capture in the atomic 3D state with B_{Ξ^-} of 0.23 MeV. The negative $\Delta B_{\Lambda\Lambda}$ value of ${}^{12}_{\Lambda\Lambda}$Be indicates it was produced in the excited state. The most probable interpretation was found to be the production and decay of the ${}^{11}_{\Lambda\Lambda}$Be nucleus from the kinematic fitting with χ^2 of 7.28 (DOF=3).

By comparing the present result with the past experiments, the present interpretation of ${}^{10}_{\Lambda\Lambda}$Be or ${}^{11}_{\Lambda\Lambda}$Be is consistent in terms of the $B_{\Lambda\Lambda}$ value. The present result has quite good accuracy because no neutron was emitted from the double-Λ hypernuclear production vertex. In the case of ${}^{11}_{\Lambda\Lambda}$Be, the present result has a larger $B_{\Lambda\Lambda}$ value than the theoretical calculations.

Emulsion scanning is still ongoing. About 30% of estimated Ξ^- stopping events has been observed so far. Further impressive events are expected to be observed in the near future.

Acknowledgements

The present work has been completed with the help of numerous people. I would like to thank the all persons who supported me by their works, advices, and encouragements.

First of all, I would like to express the deepest appreciation to my supervisor, Prof. Tomofumi Nagae. He guided me into the researching world of the nuclear physics and taught me the interesting of the strangeness physics. I received a lot of advices to write this thesis from him.

I am deeply grateful to the three spokespersons of the E07 experiment, Prof. Kazuma Nakazawa, Prof. Hirokazu Tamura, and Prof. Ken'ichi Imai. They gave me a precious opportunity to conduct the present experiment and become a doctoral candidate. Valuable discussions with them helped me to carry out the experiment and analyze the present data.

I would like to thank all the E07 collaborators. In particular, I owe a very important debt to Dr. Junya Yoshida. He is an expert of the emulsion experiment. I learned various techniques and information about the emulsion from him. He has developed the emulsion scanning system and is working hard to operate it still now. I could not finish my work without his thoughtful support. I would like to express my gratitude to Dr. Yudai Ichikawa. I learned a lot of experimental techniques, analysis methods, physics motivations, and so on from him from when I was a master course student. His zeal for physics always stimulate my motivation. I could grow up to a scientist thanks to him. I am indebted to Dr. Hwang Sanghoon and Dr. Kenji Hosomi. They helped me to develop E07 detectors and to make a plan to conduct the experiment. The E07 experiment was successfully carried out thank to their efforts. I would like to show my appreciation to Prof. Toshiyuki Takahashi, Dr. Mifuyu Ukai, Dr. Takeshi Yamamoto and Dr. Hitoshi Takahashi. They supported me to perform the experiment and give me useful advices in meetings when I faced the problem. I would like to offer my special thanks to Dr. Shuhei Hayakawa and Ms. Manami Fujita. They were also doctoral candidates of the E07 experiment and worked with me to complete the experiment. We shared an irreplaceable time in the experiment. I owe my gratitude to Dr. Masahiro Yoshimoto. He improved the scanning system drastically well. Emulsion scanning was performed because of his outstanding effort. I would like to express my appreciation to Dr. Shinji Kinbara. He led mass production of emulsion sheets and worked hard in the E07 beam time. I spend a long time to enjoy my research life in Tokai with him. I want to express my sincere gratitude to Mr. Ayumi Kasagi. He found the MINO event by the microscope scanning and helped me to analyze the event. His works are worthy of high praise. I would like to show my appreciation to Mr. Toyoki Watabe, Dr. Ryota Kiuchi and Mr. Jaeyong Lee. They developed the SSD which was essential detector of the counter-emulsion hybrid method. I would like to express my gratitude to Mr. Masahiro Hirose and Mr. Kazuya Ito. They developed the Emulsion Mover. Although we face many problems about it, we could solved them thanks to their efforts. I am very grateful to thank Mr. Kenichiro Oue. He developed SCH which was a key detector to produce (K^-, K^+) trigger condition.

I would like to thank all the K1.8 beam line members, Dr. Kotaro Shirotori, Dr. Tomonori Takahashi, Dr. Manabu Moritsu, Dr. Hitoshi Sugimura, Dr. Ry-

otaro Honda, Ms. Manami Nakagawa, Dr. Yuya Akazawa, Ms. Shinhyung Kim, Mr. Yoshiyuki Nakada, Mr. Wooseung Jung, Mr. Taejin Moon, Dr. Seongbae Yang, Dr. Koji Miwa, Dr. Takeshi Koike, Mr. Yuki Sasaki, Ms. Honoka Kanauchi, Ms. Norina Fujioka, Mr. Yuji Ishikawa, Mr. Yu Ogura, Mr. Suharu Hoshino, Mr. Abzal Iskendir, Mr. Kazuya Kobayashi, Mr. Tomonari Hayakawa, Mr. Shotaro Ozawa. We spend a lot of time to perform experiments in J-PARC Hadron Hall K1.8 beam line. I learn a lot from them.

I want to express my gratitude to students of Gifu University who joined the E07 experiment, Mr. Hiroki Ito, Ms. Yoko Endo, Mr. Hidetaka Kobayashi, Mr. Masaki Ohashi, Mr. Ryo Goto, Mr. Daisuki Nakajima, Mr. Shin Nishimura, Mr. Aung Nay Lin Nyaw, Ms. Aye Moh Moh Theint, Ms. Go Shang Hai. They performed emulsion works such as mass production, photographic development, scanning. In particular, they packed emulsion sheets into the Cassette for beam exposure in a dark room in the E07 beam time. I sincerely show respect to their hard works.

I would like to show to all the members of "Experimental Nuclear and Hadronic Physics" (NH) group in Kyoto University. I want to thank Prof. Megumi Naruki, Dr. Tetsuya Murakami, Prof. Takahiro Kawabata, Dr. Toshiyuki Gogami, Dr. Hiroyuki Fujioka, Dr. Masayuki Niiyama. They support me to learn nuclear physics and encourage me. I want to thank Mr. Toshikazu Hashimoto, Mr. Shunsuke Kanatsuki and Dr. Keigo Mizutani. They entered the graduate school in the same year with me. I enjoyed my campus life in the Kyoto University with them. Especially, Mr. Kanatsuki carried out his experiment at the J-PARC K1.8 beam line and I worked with him. He helped me a lot and gave me useful advices. I want to thank all the NH students who shared meaningful time with me. In particular, Mr. Takuya Nanamura, Ms. Sakiko Ashikaga, Mr. Masaya Ichikawa and Mr. Kazuki Suzuki are the member of K1.8 beam line group. I enjoyed experimental works with them.

I owe my gratitude to all the members of "Research Group for Hadron nuclear physics" in Advanced Science Research Center of Japan Atomic Energy Agency, Prof. Makoto Oka, Prof. Hiroyuki Sako, Prof. Shoichi Hasegawa, Prof. Susumu Sato, Prof. Kiyoshi Tanida, Prof. Toshiki Maruyama, Dr. Takayasu Sekihara, Dr. Philipp Gubler, Dr. Tadashi Hashimoto. They give me the good environment to concentrate and enjoy my research life.

I appreciate secretaries who supported me to spend a fruitful research life, Ms. Shiori Yamamoto, Ms. Aya Araki, Ms. Eiko Yoshino, Ms. Yuri Kimura, Ms. Mayumi Hiraoka, Ms. Noriko Hirano, Ms. Yuri Nishikubo, Ms. Mariko Tanizawa, Ms. Michiko Matsuo and Ms. Akiko Iioka. I could concentrate to research and have a swell time thanks to them.

I am indebted to all the staffs of KEK and J-PARC involved with the present experiment. They gave me an opportunity to perform the present experiment. They provide us an excellent beam quality in spite of the accelerator troubles. The present experiment has been completed because of their untiring efforts.

And last but not least, I would like to offer my special thanks to my family for their warmhearted supports.

Appendix A

Estimation of K^+ component

As shown in Fig. 3.12, the distribution of the squared mass of reconstructed particles depended on its momentum caused by the difference of their time-of-flight. In order to obtain the number of net K^+ in the tagged Ξ^- events, the fitting with Gaussian and 1D-polynomial background was performed in each momentum band. Figure A.1 shows the result of the fitting by dividing them into 50 MeV/c momentum bands.

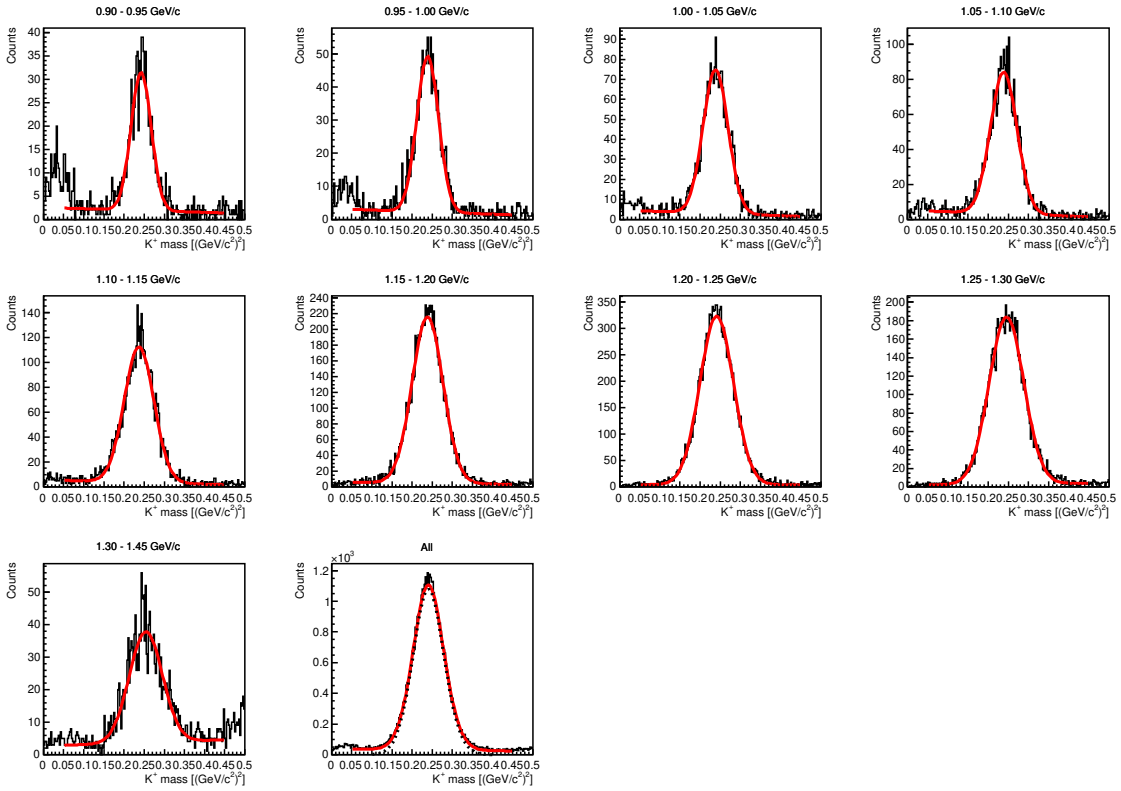

Figure A.1: Distribution of the squared mass of K^+ after the Ξ^- selection criteria without squared mass cut. Each histogram shows the result of 50 MeV/c momentum band. Since the number of event with more than 1.3 GeV/c was small, those were combined.

Appendix B

Mass table of nuclides

Table B.1: Mass table in S=0 (A $<$ 10). All values were obtained from the mass table [70].

Nuclide	Mass number (A)	Charge (Z)	Mass [MeV/c^2]
π^0	0	0	134.977
π^-	0	-1	139.570
n	1	0	939.565
p	1	1	938.272
d	2	1	1875.613
t	3	1	2808.921
^{3}He	3	2	2808.391
^{4}He	4	2	3727.379
^{6}He	6	2	5605.534
^{6}Li	6	3	5601.518
^{7}Li	7	3	6533.833
^{7}Be	7	4	6534.184
^{8}He	8	2	7482.540
^{8}Li	8	3	7471.365
^{8}B	8	5	7472.320
^{9}Li	9	3	8406.868
^{9}Be	9	4	8392.751
^{9}B	9	5	8393.309
^{9}C	9	6	8409.293

Table B.2: Mass table in S=0 (A $\geq$ 10). All values were obtained from the mass table [70].

Nuclide	Mass number (A)	Charge (Z)	Mass [MeV/c^2]
^{10}Be	10	4	9325.504
^{10}B	10	5	9324.437
^{10}C	10	6	9327.574
^{11}Li	11	3	10285.630
^{11}Be	11	4	10264.568
^{11}B	11	5	10252.548
^{11}C	11	6	10254.019
^{12}Be	12	4	11200.963
^{12}B	12	5	11188.744
^{12}C	12	6	11174.864
^{12}N	12	7	11191.691
^{13}Be	13	4	12141.038
^{13}B	13	5	12123.430
^{13}C	13	6	12109.483
^{13}N	13	7	12111.193
^{13}O	13	8	12128.452
^{14}Be	14	4	13078.827
^{14}B	14	5	13062.026
^{14}C	14	6	13040.872
^{14}N	14	7	13040.204
^{14}O	14	8	13044.839
^{15}B	15	5	13998.815
^{15}C	15	6	13979.219
^{15}N	15	7	13968.936
^{15}O	15	8	13971.181
^{16}B	16	5	14938.463
^{16}C	16	6	14914.534
^{16}N	16	7	14906.013
^{16}O	16	8	14895.082

Table B.3: Mass table in $S = -1$. The B_Λ values of unobserved nuclides are enclosed in parentheses and those are estimated by extrapolating that of isotopes.

Nuclide	Mass number (A)	Charge (Z)	Mass [MeV/c^2]	B_Λ [MeV]	Reference
Λ	1	0	1115.683	-	[61]
${}^{3}_{\Lambda}$H	3	1	2991.17	0.13	[71]
${}^{4}_{\Lambda}$H	4	1	3922.56	2.04	[71]
${}^{4}_{\Lambda}$He	4	2	3921.68	2.39	[71]
${}^{5}_{\Lambda}$H	5	1	4861.82	(3.95)	
${}^{5}_{\Lambda}$He	5	2	4839.94	3.12	[71]
${}^{6}_{\Lambda}$He	6	2	5779.18	4.18	[60]
${}^{6}_{\Lambda}$Li	6	3	5778.8	4.5	[72]
${}^{7}_{\Lambda}$He	7	2	6715.67	5.55	[73]
${}^{7}_{\Lambda}$Li	7	3	6711.62	5.58	[71]
${}^{7}_{\Lambda}$Be	7	4	6715.82	5.16	[71]
${}^{8}_{\Lambda}$He	8	2	7654.03	7.16	[71]
${}^{8}_{\Lambda}$Li	8	3	7642.72	6.80	[71]
${}^{8}_{\Lambda}$Be	8	4	7643.03	6.84	[71]
${}^{9}_{\Lambda}$He	9	2	8591.62	(6.60)	
${}^{9}_{\Lambda}$Li	9	3	8578.55	8.50	[60]
${}^{9}_{\Lambda}$Be	9	4	8563.82	6.71	[71]
${}^{9}_{\Lambda}$B	9	5	8579.71	8.29	[60]
${}^{10}_{\Lambda}$He	10	2	9531.59	(7.46)	
${}^{10}_{\Lambda}$Li	10	3	9513.13	(9.42)	
${}^{10}_{\Lambda}$Be	10	4	9499.83	8.60	[60]
${}^{10}_{\Lambda}$B	10	5	9500.10	8.89	[71]
${}^{11}_{\Lambda}$Li	11	3	10451.44	(10.71)	
${}^{11}_{\Lambda}$Be	11	4	10432.99	(8.20)	
${}^{11}_{\Lambda}$B	11	5	10429.88	10.24	[71]
${}^{11}_{\Lambda}$C	11	6	10433.15	(10.10)	
${}^{12}_{\Lambda}$Be	12	4	11371.41	(8.84)	
${}^{12}_{\Lambda}$B	12	5	11356.86	11.37	[71]
${}^{12}_{\Lambda}$C	12	6	11358.90	10.80	[74]
${}^{13}_{\Lambda}$B	13	5	12291.95	(12.48)	
${}^{13}_{\Lambda}$C	13	6	12278.86	11.69	[60]
${}^{13}_{\Lambda}$N	13	7	12295.16	(12.21)	
${}^{14}_{\Lambda}$B	14	5	13225.51	(13.61)	
${}^{14}_{\Lambda}$C	14	6	13213.00	12.17	[60]
${}^{14}_{\Lambda}$N	14	7	13214.71	12.17	[75]
${}^{15}_{\Lambda}$C	15	6	14143.40	(13.16)	
${}^{15}_{\Lambda}$N	15	7	14142.30	13.59	[71]
${}^{16}_{\Lambda}$C	16	6	15080.98	(13.92)	
${}^{16}_{\Lambda}$N	16	7	15070.86	13.76	[76]
${}^{16}_{\Lambda}$O	16	8	15074.44	12.42	[77]

Table B.4: Mass table in $S = -2$. Masses are calculated by assuming $\Delta B_{\Lambda\Lambda} = 0$. The B_Λ values of unobserved ${}^{A-1}_{\Lambda}Z$ are enclosed in parentheses same as Table B.3.

Nuclide	Mass number (A)	Charge (Z)	Mass [MeV/c^2]	$B_\Lambda({}^{A-1}_{\Lambda}Z)$ [MeV]
Ξ^-	1	-1	1321.71	-
${}^{4}_{\Lambda\Lambda}$H	4	1	4106.72	0.13
${}^{5}_{\Lambda\Lambda}$H	5	1	5036.21	2.04
${}^{5}_{\Lambda\Lambda}$He	5	2	5034.98	2.39
${}^{6}_{\Lambda\Lambda}$H	6	1	5973.55	(3.95)
${}^{6}_{\Lambda\Lambda}$He	6	2	5952.51	3.12
${}^{7}_{\Lambda\Lambda}$He	7	2	6890.69	4.18
${}^{7}_{\Lambda\Lambda}$Li	7	3	6890.0	4.5
${}^{8}_{\Lambda\Lambda}$He	8	2	7825.80	5.55
${}^{8}_{\Lambda\Lambda}$Li	8	3	7821.72	5.58
${}^{8}_{\Lambda\Lambda}$Be	8	4	7826.34	5.16
${}^{9}_{\Lambda\Lambda}$He	9	2	8762.56	7.16
${}^{9}_{\Lambda\Lambda}$Li	9	3	8751.60	6.80
${}^{9}_{\Lambda\Lambda}$Be	9	4	8751.87	6.84
${}^{10}_{\Lambda\Lambda}$He	10	2	9700.71	(6.60)
${}^{10}_{\Lambda\Lambda}$Li	10	3	9685.73	8.50
${}^{10}_{\Lambda\Lambda}$Be	10	4	9672.80	6.71
${}^{10}_{\Lambda\Lambda}$B	10	5	9687.11	8.29
${}^{11}_{\Lambda\Lambda}$He	11	2	10639.81	(7.46)
${}^{11}_{\Lambda\Lambda}$Li	11	3	10619.40	(9.42)
${}^{11}_{\Lambda\Lambda}$Be	11	4	10606.92	8.60
${}^{11}_{\Lambda\Lambda}$B	11	5	10606.90	8.89
${}^{12}_{\Lambda\Lambda}$Li	12	3	11556.42	(10.71)
${}^{12}_{\Lambda\Lambda}$Be	12	4	11540.47	(8.20)
${}^{12}_{\Lambda\Lambda}$B	12	5	11535.32	10.24
${}^{12}_{\Lambda\Lambda}$C	12	6	11538.73	(10.10)
${}^{13}_{\Lambda\Lambda}$Be	13	4	12478.25	(8.84)
${}^{13}_{\Lambda\Lambda}$B	13	5	12461.17	11.37
${}^{13}_{\Lambda\Lambda}$C	13	6	12463.79	10.80
${}^{14}_{\Lambda\Lambda}$B	14	5	13395.15	(12.48)
${}^{14}_{\Lambda\Lambda}$C	14	6	13382.85	11.69
${}^{14}_{\Lambda\Lambda}$N	14	7	13398.63	(12.21)
${}^{15}_{\Lambda\Lambda}$B	15	5	14327.59	(13.61)
${}^{15}_{\Lambda\Lambda}$C	15	6	14316.51	12.17
${}^{15}_{\Lambda\Lambda}$N	15	7	14318.22	12.17
${}^{16}_{\Lambda\Lambda}$C	16	6	15245.92	(13.16)
${}^{16}_{\Lambda\Lambda}$N	16	7	15244.39	13.59
${}^{17}_{\Lambda\Lambda}$C	17	6	16182.74	(13.92)
${}^{17}_{\Lambda\Lambda}$N	17	7	16172.78	13.76

Appendix C

Solution of the kinematic fitting

As shown in Eq. (5.3), the χ^2 of the kinematic fitting is defined as follows:

$$\chi^2 = (\boldsymbol{\eta} - \boldsymbol{\eta_0})^t \boldsymbol{V}_{\eta_0}^{-1} (\boldsymbol{\eta} - \boldsymbol{\eta_0}) + 2\boldsymbol{\lambda}^t (\boldsymbol{D}\boldsymbol{\eta} + \boldsymbol{E}\boldsymbol{z} + \boldsymbol{d}). \tag{1}$$

In order to minimize the χ^2 on the Lagrange multipliers method, the following constraints are required.

$$\boldsymbol{V}_{\eta_0}^{-1} (\boldsymbol{\eta} - \boldsymbol{\eta_0}) + \boldsymbol{D}^t \boldsymbol{\lambda} = \boldsymbol{0}, \tag{2}$$

$$\boldsymbol{D}\boldsymbol{\eta} + \boldsymbol{E}\boldsymbol{z} + \boldsymbol{d} = \boldsymbol{0}, \tag{3}$$

$$\boldsymbol{E}^t \boldsymbol{\lambda} = \boldsymbol{0}. \tag{4}$$

These equations can be solve as follows:

$$\boldsymbol{\lambda_0} = \boldsymbol{V_D}(\boldsymbol{D}\boldsymbol{\eta_0} + \boldsymbol{d}), \tag{5}$$

$$\boldsymbol{z} = -\boldsymbol{V_E}\boldsymbol{E}^t \boldsymbol{\lambda_0}, \tag{6}$$

$$\boldsymbol{\lambda} = \boldsymbol{\lambda_0} + \boldsymbol{V_D}\boldsymbol{E}\boldsymbol{z}, \tag{7}$$

$$\boldsymbol{\eta} = \boldsymbol{\eta_0} - \boldsymbol{V}_{\eta_0}\boldsymbol{D}^t \boldsymbol{\lambda}, \tag{8}$$

where,

$$\boldsymbol{V_D} = (\boldsymbol{D}\boldsymbol{V}_{\eta_0}\boldsymbol{D}^t)^{-1}, \tag{9}$$

$$\boldsymbol{V_E} = (\boldsymbol{E}^t \boldsymbol{V_D} \boldsymbol{E})^{-1}. \tag{10}$$

Then χ^2 is obtained as

$$\chi^2 = \boldsymbol{\lambda}^t \boldsymbol{V_D}^{-1} \boldsymbol{\lambda}. \tag{11}$$

Bibliography

[1] T. A. Rijken, M. M. Nagels, and Y. Yamamoto, Prog. Theor. Phys. Suppl. **185** 14 (2010).

[2] M. M. Nagels, T. A. Rijken, Y. Yamamoto, Phys. Rev. C **99**, 044002 (2019).

[3] M. M. Nagels, T. A. Rijken, Y. Yamamoto, Phys. Rev. C **99**, 044003 (2019).

[4] P. Khaustov *et al.*, Phys. Rev. C **61**, 054603 (2000).

[5] Takashi Inoue, arXiv:1809.08932 [hep-lat] (2018).

[6] K.-I. Ishikawa *et al.* [PACS Collaboration], PoS LATTICE **2015**, 075 (2016).

[7] P. B. Demorest *et al.*, Nature **467**, 1081 (2010).

[8] J. Antoniadis *et al.*, Science **340**, 1233232 (2013).

[9] D. Lonardoni, A. Lovato, S. Gandolfi, and F. Pederiva, Phys. Rev. Lett. **114**, 092301 (2015).

[10] H. Togashi *et al.*, Phys. Rev. C **93**, 035808 (2016).

[11] R. L. Jaffe, Phys. Rev. Lett. **38**, 195 (1977).

[12] T. Sakai, K. Shimizu and K. Yazaki, Prog. Theor. Phys. Suppl. **137**, 121 (2000).

[13] H. Takahashi *et al.*, Phys. Rev. Lett. **87**, 212502 (2001).

[14] T. Inoue *et al.*, Nucl. Phys. A **881**, 28 (2012).

[15] J. K. Ahn (spokespersons), *et al.*, J-PARC P42 proposal.

[16] J. K. Ahn *et al.*, Phys. Rev. Lett. **87**, 132504 (2001).

[17] S. D. Randeniya and E. V. Hungerford, Phys. Rev. C **76**, 064308 (2007).

[18] S. Bleser *et al.*, Phys. Lett. B **790** 502 (2019).

[19] P. H. Pile *et al.*, Nucl. Instrum. Methods Phys. Res. A **321**, 48 (1992).

[20] T. Nagae (spokespersons), *et al.*, J-PARC P05 proposal.

[21] T. Nagae (spokespersons), *et al.*, J-PARC P70 proposal.

[22] K. Nakazawa *et al.*, Prog. Theor. Exp. Phys. **2015**, 033D02 (2015).

[23] S. Acharya *et al.*, Phys. Rev. C **99**, 024001 (2019).

[24] R. B. Wiringa, V. G. J. Stoks, and R. Schiavilla, Phys. Rev. C **51**, 38 (1995).

[25] M. Danysz *et al.*, Nuclear Physics **49**, 121 (1963).

[26] S. Aoki *et al.*, Nucl. Phys. A **828**, 191 (2009).

[27] S. Aoki *et al.*, Prog. Theor. Phys. **85** 1287 (1991).

[28] J. K. Ahn *et al.*, Phys. Rev. C **88**, 014003 (2013).

[29] M. Yamaguchi, K. Tominaga, Y. Yamamoto, and T. Ueda, Prog. Theor. Phys. **105**, 627 (2001).

[30] R. H. Dalitz *et al.*, Proc. R. Soc. A **426**, 1 (1989).

[31] D. H. Davis, Nucl. Phys. A **754**, 3c (2005).

[32] E. Hiyama and K. Nakazawa, Annu. Rev. Nucl. Part. Sci. **68**, 131 (2018).

[33] E. Hiyama, M. Kamimura, Y. Yamamoto, and T. Motoba, Phys. Rev. Lett. **104**, 212502 (2010).

[34] K. Nakazawa, K. Imai, and H. Tamura (spokespersons), *et al.*, J-PARC P07 proposal.

[35] E. Hiyama *et al.*, Phys. Rev. C **66**, 024007 (2002).

[36] Y. Hirata *et al.*, Prog. Theor. Phys. **102**, 89 (1999).

[37] T. Takahashi *et al.*, Prog. Theor. Exp. Phys. **2012**, 02B010 (2012).

[38] S. Morinobu, unpublished.

[39] J. Myrheim and L. Bugge, Nucl. Instr. Meth. **160**, 43 (1979).

[40] R. Honda *et al.*, PoS PhotoDet2012, 031 (2013).

[41] T. Iijima *et al.*, Nucl. Phys. A **546**, 588 (1992).

[42] D. E. Alburger and M. May, Nucl. Instrum. Meth. A **443**, 27 (2000).

[43] Y. Igarashi, IEEE Trans. Nucl. Sci. **52**, 2866, (2005).

[44] ANSYS, (htpp://www.ansys.com).

[45] MINUIT Function Minimization and Error Analysis: Reference Manual Version 94.1 - F. James, CERN-D506.

[46] Geant4 homepage, (http://geant4.web.cern.ch/).

[47] Y. Nara, N. Otuka, A. Ohnishi, K. Niita, and S. Chiba, Phys. Rev. C **61**, 024901 (2000).

[48] M. K. Soe *et al.*, Nucl. Instrum. Methods Phys. Res. Sect. A **848**, 66 (2017).

[49] W. H. Barkas, Pure & Applied Physics series 15-I: Nuclear Research Emulsions (Academic Press, New York, 1963).

[50] H. H. Heckman *et al.*, Phys. Rev. **117**, 544, (1960).

[51] K. Abusaleem, Nuclear Data Sheets **116**, 163 (2014).

[52] S. Singh and B.Singh, Nuclear Data Sheets **130**, 127 (2015).

[53] E. Browne, J. K. Tuli, Nuclear Data Sheets **112**, 1115 (2011).

[54] S. -C. Wu, Nuclear Data Sheets **108**, 1057 (2007).

[55] E. Browne, Nuclear Data Sheets **104**, 427 (2005).

[56] M. J. Martin, Nuclear Data Sheets **108**, 1583 (2007).

[57] J. Yoshida *et al.*, Nucl. Instrum. Methods Phys. Res. Sect. A **847**, 86 (2017).

[58] P. Avery, Applied Fitting Theory I: General Least Squares Theory, CLEO Note CBX, 91–72, (1991).

[59] D. R. Tilley, C. M. Cheves, J. L. Godwin, G. M. Hale, H. M. Hofmann, J. H. Kelley, C. G. Sheu, and H. R. Weller, Nucl. Phys. A **708**, 3 (2002).

[60] D. H. Davis, Contemporary Physics, **27:2**, 91 (1986).

[61] M. Tanabashi *et al.* (Particle Data Group), Phys. Rev. D **98**, 030001 (2018).

[62] T. Gogami *et al.*, Phys. Rev. C **93**, 034314 (2016).

[63] D. J. Millener, C. B. Dover and A. Gal, Prog. Theor. Phys. Suppl. **117**, 307 (1994).

[64] D. Bertrand, G. Coremans, C. Mayeur, J. Sacton, P. Vilain, G. Wilquet, J. H. Wickens, D. O' Sullivan, D. H. Davis, and J. E. Allen, Nucl. Phys. B **16**, 77 (1970).

[65] H. Kamada, J. Golak, K. Miyagawa, H. Witała, and W. Glöckle, Phys. Rev. C **57**, 1595 (1998).

[66] A. Gal and D.J. Millener, Phy. Let. B **701**, 342 (2011).

[67] Wen-Ying Li, Ji-Wei Cui, and Xian-Rong Zhou, Phys. Rev. C **97**, 034302 (2018).

[68] Yoshiko Kanada-En'yo, Phys. Rev. C **97**, 034324 (2018).

[69] D. R. Tilley, J. H. Kelley, J. L. Godwin, D. J. Millener, J. Purcell, C. G. Sheu, and H. R. Weller, Nucl. Phys. A **745**, 155 (2004).

[70] M. Wang, G. Audi, F. G. Kondev, W. J. Huang, S. Naimi, and X. Xu, Chinese Physics C **41**, 030003 (2017).

[71] M. Juric *et al.*, Nucl. Phys. B **52**, 1 (1973).

[72] R. Bertini *et al.*, Nucl. Phys. A **368**, 365 (1981).

[73] T. Gogami *et al.*, Phys. Rev. C **94**, 021302(R) (2016).

[74] P. Dluzewski *et al.*, Nucl. Phys. A **484**, 520 (1988).

[75] M. May *et al.*, Phys. Rev. Lett. **47**, 1106 (1981).

[76] F. Cusanno *et al.*, Phys. Rev. Lett. **103**, 202501 (2009).

[77] O. Hashimoto and H. Tamura, Prog. Part. Nucl. Phys. **57**, 564 (2006).

List of Figures

List of Tables